TU Delft

Delft University of Technology

Turbulent shear flow over complex surfaces

An experimental study

Greidanus, A.J.

DOI
10.4233/uuid:5d46cffe-032b-4084-8c09-88ab7f0f767d

Publication date
2020

Document Version
Final published version

Citation (APA)
Greidanus, A. J. (2020). *Turbulent shear flow over complex surfaces: An experimental study*. [Dissertation (TU Delft), Delft University of Technology]. https://doi.org/10.4233/uuid:5d46cffe-032b-4084-8c09-88ab7f0f767d

Important note
To cite this publication, please use the final published version (if applicable).
Please check the document version above.

Copyright
Other than for strictly personal use, it is not permitted to download, forward or distribute the text or part of it, without the consent of the author(s) and/or copyright holder(s), unless the work is under an open content license such as Creative Commons.

Takedown policy
Please contact us and provide details if you believe this document breaches copyrights.
We will remove access to the work immediately and investigate your claim.

This work is downloaded from Delft University of Technology.
For technical reasons the number of authors shown on this cover page is limited to a maximum of 10.

TURBULENT SHEAR FLOW OVER COMPLEX SURFACES

-AN EXPERIMENTAL STUDY-

TURBULENT SHEAR FLOW OVER COMPLEX SURFACES

-AN EXPERIMENTAL STUDY-

Proefschrift

ter verkrijging van de graad van doctor
aan de Technische Universiteit Delft,
op gezag van de Rector Magnificus prof. dr. ir. T.H.J.J. van der Hagen,
voorzitter van het College voor Promoties,
in het openbaar te verdedigen op vrijdag 02 oktober 2020 om 10:00 uur

door

Arnoud Jan GREIDANUS

Scheikundig Ingenieur,
Technische Universiteit Delft, Nederland,
geboren te Leiderdorp, Nederland.

Dit proefschrift is goedgekeurd door de

Promotor: prof. dr. ir. J. Westerweel
Promotor: prof. dr. S.J. Picken
Copromotor: dr. R. Delfos

Samenstelling promotiecommissie:

Rector Magnificus,	Voorzitter
Prof. dr. ir. J. Westerweel,	Technische Universiteit Delft
Prof. dr. S.J. Picken,	Technische Universiteit Delft
Dr. R. Delfos,	Technische Universiteit Delft
Onafhankelijke leden:	
Prof. F. Moisy,	Université Paris-Saclay
Prof. dr. ir. C.H. Venner,	Universiteit Twente
Prof. dr. ir. C. Poelma,	Technische Universiteit Delft
Prof. dr. ir. T.J.C. van Terwisga,	Technische Universiteit Delft

Part of this research was supported by InnoSportNL, under contract number 4010.0020.

Cover: Artist's impression of a displacement field
Cover design: Marianne Neijts
Printed by: Ridderprint | www.ridderprint.nl

Copyright © 2020 by A.J. Greidanus, all rights reserved.

ISBN 978-94-6416-152-6

An electronic version of this dissertation is available at
http://repository.tudelft.nl.

To my loved ones.

CONTENTS

SUMMARY

This thesis describes the investigation of the dynamics of turbulent shear flows over non-smooth surfaces. The research was conducted in two parts, related to the experimental facility used in combination with the applied functional surface. The first part describes the experiments of a turbulent Taylor-Couette flow over a riblet surface. The Taylor-Couette facility proves to be an accurate measurement device to determine the frictional drag of surfaces under turbulent flow conditions. Sawtooth riblets are applied on the inner cylinder surface and have the ability to reduce the total measured drag by 5.3% at $Re_s = 4.7 \times 10^4$. Under these conditions, a small shift is observed in the azimuthal velocity profile that indicates the change in the net system rotation, which on its turn affects the quantity of drag change, the so-called rotation effect. A model based on the angular momentum balance is proposed and quantifies the drag change due to the rotation effect. Using the total measured drag change, the model accurately predicts the velocity shift in the azimuthal direction.
In addition to the steady operational conditions, periodically driven Taylor-Couette flows were investigated by modulating the velocity between the two cylinders as a sinusoidal function, while maintaining $R_\Omega = 0$. The main scaling parameters are the shear Reynolds number Re_s, the oscillation Reynolds number Re_{osc} and the Womersley number Wo, such that the required power to overcome the frictional drag becomes equal to $\langle P_d \rangle = f(Re_s, Re_{osc}, Wo)$. Large velocity amplitudes $\mathscr{A} = Re_{osc}/Re_s \geq 0.10$ induce the growth of frictional drag due to the additional turbulent fluctuations. The required power to overcome the frictional drag is given by
$\langle P_d \rangle = \langle P_{d,0} \rangle \left(f(\mathscr{A}) + \mathscr{K}^* Wo^4 \mathscr{A}^2 \right)$. The first term represents the analytical quasi-steady state solution with the accompanying velocity modulation, while the second term involves the magnitude of the boundary acceleration with the associated velocity fluctuation, where $\mathscr{K}^*$ is the conditional scaling-factor between the additional drag and the dimensionless acceleration. Riblets are still able to reduce the frictional drag under small accelerations of the periodically driven boundaries, but the effect declines drastically or even enhances the frictional drag when the boundary acceleration becomes more significant.

The second part of this thesis describes the assessment of the applied water tunnel and the interactional behavior between a compliant coating and a turbulent boundary layer flow in the tunnel. In the assessment of the water tunnel, the Clauser chart method showed to be a suitable procedure to quantify the local wall shear stress τ_w.
The interaction between a compliant wall and the near-wall turbulent flow was examined by applying in-house produced visco-elastic coatings with three different stiffnesses. Two typical flow-surface interaction regimes were identified; the one-way coupled regime and the two-way coupled regime. The one-way coupled regime is valid when the turbulent flow initiates moderate coating surface deformation, while the

fluid flow remains undisturbed. All of the three coatings exhibited the one-way coupled interactional behavior, where the surface modulations ζ were smaller than the viscous sublayer thickness δ_v and scale with the turbulent pressure fluctuations over the coating shear modulus, i.e. $\zeta_{rms} \sim p_{rms}/|G^*|$. In this regime, the surface waves have the propagation velocity in the order of $c_w = 0.70 - 0.80\ \bar{U}_b$, indicating a strong correlation with the high-intensity pressure fluctuations in the turbulent boundary layer away from the wall. The two-way coupled regime has only been observed for the coating with the lowest shear modulus when $\bar{U}_b > 4.5$ m/s, indicating significant surface deformation accompanied by additional fluid motions (u', v') and an increase in the local Reynolds stresses. The velocity profile shifts downwards Δu^+ in the log region, which verifies the drag increase due to the significant surface undulations.
The visualizations of the surface deformation showed the formation of wave-trains with high amplitudes originating from the initial surface undulations caused by the pressure fluctuations in the turbulent boundary layer (i.e. one-way coupling). When these early surface undulations start to protrude the viscous sublayer, the turbulent flow is capable of transfering more energy towards the coating and initiates the wave-train with high amplitudes. The wave-trains dominate the coating surface incrementally with increasing bulk velocity and propagate with a wave velocity of $c_w = 0.17$-0.18 $\bar{U}_b$. The 1-way/2-way regime transition is estimated to occur around $\zeta_{rms} > \delta_v/2$.
The turbulent flow along the slow-moving wave-trains resembles the classical phenomenon of a turbulent flow over a rigid wavy surface, with a local acceleration and deceleration of the fluid. When the wave-trains start to dominate the coating surface, a linear correlation determines the abovementioned downward shift Δu^+, based on the wall-normal velocity component $\partial\zeta/\partial t$. No frictional drag reduction under turbulent flow conditions was found in this study with this type of visco-elastic compliant coatings.

SAMENVATTING

Dit proefschrift beschrijft het onderzoek naar de dynamica van turbulente stromingen over niet-gladde oppervlakken. Het onderzoek werd uitgevoerd in twee delen, gerelateerd aan de gebruikte experimentele faciliteit in combinatie met het toegepaste functionele oppervlak. Het eerste deel beschrijft experimenten van een turbulente Taylor-Couette stroming langs een geribbeld oppervlak (/riblets). De Taylor-Couette faciliteit bewijst een nauwkeurig meetapparaat te zijn om de wrijvingsweerstand van oppervlakken onder turbulente stromingsomstandigheden te bepalen. Zaagtand riblets zijn aangebracht op het oppervlak van de binnen cilinder en hebben de mogelijkheid om de totale gemeten weerstand met 5.3 % te verminderen bij $Re_s = 4.7 \times 10^4$. Onder deze condities wordt een kleine verschuiving waargenomen in het azimutale snelheidsprofiel dat wijst op een verandering in de netto systeemrotatie, die op zijn beurt de hoeveelheid weerstandsverandering beïnvloedt, het zogenoemde rotatie-effect. Een model gebaseerd op het hoek-momentum evenwicht is voorgesteld en kwantificeert de weerstandsverandering als gevolg van het rotatie-effect. Met behulp van de totale gemeten weerstandsverandering, voorspelt het model nauwkeurig de kleine snelheidsverschuiving in de azimutale richting.
Behalve stabiele operationele condities, werden ook periodiek aangedreven Taylor-Couette stromingen onderzocht door de snelheid tussen de twee cilinders als een sinusfunctie te moduleren, met behoud van $R_\Omega = 0$. De belangrijkste schalingsparameters zijn het afschuif Reynolds getal Re_s, het oscillatie Reynolds getal Re_{osc} en het Womersley getal Wo, zodat het benodigde vermogen om de wrijvingsweerstand te overwinnen gelijk is aan $\langle P_d \rangle = f(Re_s, Re_{osc}, Wo)$. Grote snelheidsamplitudes $\mathscr{A} = Re_{osc}/Re_s \geq 0.10$ induceren de toename van de wrijvingsweerstand als gevolg van de extra turbulente fluctuaties. De vereiste kracht om de wrijvingsweerstand te overwinnen wordt gegeven door $\langle P_d \rangle = \langle P_{d,0} \rangle \left(f(\mathscr{A}) + \mathscr{K}^* Wo^4 \mathscr{A}^2 \right)$. De eerste term vertegenwoordigt de analytisch quasi-steady-state oplossing met de bijbehorende snelheidsmodulatie, terwijl de tweede term de grootte van de versnelling is met de bijbehorende snelheidsschommeling, waarbij $\mathscr{K}^*$ de conditionele schalingsfactor is tussen de extra weerstand en de dimensieloze versnelling. Riblets zijn nog steeds in staat om de wrijvingsweerstand te verminderen onder kleine periodieke versnellingen, maar dit neemt drastisch af of verhoogt zelfs de wrijvingsweerstand wanneer de versnelling significant is.

Het tweede deel van dit proefschrift beschrijft de evaluatie van de toegepaste watertunnel en het interactie gedrag tussen een flexibele coating en een turbulente grenslaag stroming in de tunnel. In de beoordeling van de watertunnel, bleek de Clauser-chart methode een geschikte procedure om de lokale wand schuifspanning τ_w te kwantificeren.
De interactie tussen een flexibele wand en de turbulente stroming nabij de wand werd

onderzocht door het aanbrengen van zelf-geproduceerde visco-elastische coatings met drie verschillende stijfheden. Twee typische regimes van interactie tussen stroming en oppervlak werden geïdentificeerd; het éénrichtingsgekoppelde regime en het tweerichtingsgekoppelde regime. Het éénrichtingsgekoppelde regime is geldig wanneer de turbulente stroming matige vervorming van het coatingoppervlak initieert, terwijl de vloeistofstroming ongehinderd blijft. Alle drie coatings vertoonden het éénrichtingsgekoppelde interactie gedrag, waarbij de oppervlaktemodulaties ζ kleiner waren dan de viskeuze sublaag dikte δ_ν en schaalt met de turbulente drukfluctuaties over de coating afschuif modulus, oftewel $\zeta_{rms} \sim p_{rms}/|G^*|$. In dit regime hebben de oppervlaktegolven een voortplantingssnelheid in de ordegrootte van $c_w = 0.70 - 0.80\ \bar{U}_b$, hetgeen een sterke correlatie lijkt te hebben met de hoge intensiteit drukfluctuaties in de turbulente grenslaag ver van de wand. Het in twee richtingen gekoppelde regime is alleen waargenomen voor de coating met de laagste afschuif modulus wanneer $\bar{U}_b > 4.5$ m/s en duidt op significante oppervlaktevervorming die vergezeld gaan met extra vloeistofbewegingen (u', v') en een toename van de lokale Reynolds-stress. Het snelheidsprofiel schuift naar beneden Δu^+ in het log-gebied, wat de toename van de weerstand aantoont als gevolg van de significante oppervlakte golven.
De visualisaties van de oppervlaktevervorming toonden de formatie van golftreinen met hoge amplitudes die voortkomen uit de initiële oppervlaktegolven die veroorzaakt zijn door de drukschommelingen in de turbulente grenslaag (oftewel éénrichtingsgekoppeld). Wanneer deze eerdere oppervlakte golven beginnen uit te steken boven de viskeuze sublaag, zal de turbulente stroom in staat zijn om meer energie naar de coating over te brengen en initieert daarmee de golftrein met hoge amplitudes. De golftreinen domineren meer het coatingoppervlak met toenemende bulksnelheid en planten zich voort met een golfsnelheid van c_w = 0.17 - 0.18 $\bar{U}_b$. De 1-richting/2-richting regimeovergang vindt naar schatting plaats rond $\zeta_{rms} > \delta_\nu/2$.
De turbulente stroming over de langzaam bewegende golftreinen lijkt op het klassieke verschijnsel van een turbulente stroming over een rigide golvend oppervlak, met een lokale versnelling en vertraging van de vloeistof. Wanneer de golftreinen het coatingoppervlak beginnen te domineren, definieert een lineaire correlatie de bovengenoemde neerwaartse verschuiving Δu^+, gebaseerd op de wand-normale snelheidscomponent $\partial\zeta/\partial t$. Binnen dit onderzoek, werd er met deze visco-elastische flexibele coatings geen wrijvingsreductie gevonden onder turbulente stromingsomstandigheden.

1

INTRODUCTION

1

1.1. BACKGROUND [1]

Flow. It encompasses the concept of the ever changing state of being, as the Greek philosopher Heraclitus expressed: "Panta Rhei", meaning "everything flows". Flow is the dynamic movement of fluids and forms an existential part of our daily life. The encountered wind in our face, the pulsating blood flow in our veins, the curling movement of the clouds. These natural phenomena can have an extensive effect on human senses and perception, and reveal their inherent beauty. Even the smallest things in life. For example, a plastic bag dancing aesthetically in the wind appears free but actually the bag is entrapped by the benevolent force of the wind. The expected change and the unexpected movement provoke the urge to understand the physical interaction between the wind and the plastic bag. Taking the time to exercise all our senses, to experience ordinary things in life, will eventually induce astonishment and conception of the natural phenomena, which can give direction to new insights, perspectives and opportunities.

Scientific research embodies the endless search to understand the physical aspect of nature. Also within the field of fluid physics, the early researchers were frequently bemused with the unknown fluid phenomena they experienced and were overwhelmed by their new discoveries. These pioneers were dedicated to reproduce, investigate and analyze the flow conditions they observed, in order to understand the physics of nature. In 1839, it was Hagen who initially discovered the transition to a second flow regime during his pressure-drop experiments [2]. However, he was unable to explain the physical mechanism of this new flow phenomena, which became known as the turbulent state of a fluid flow. A few decades later, Reynolds took the honor with his classical pipe experiment in 1883 [3]. He demonstrated that the change in the flow regime depends on the dimensionless parameter Ud/ν, the so-called Reynolds number Re. In 1904, Prandtl made a major contribution in the conceptual understanding of turbulent fluid flows, by introducing the concept of the boundary layer in a fluid flow near a solid interface [4]. This eventually evolved to the theory of the universal turbulent velocity profile (i.e "law of the wall"), which is considered to be one of the cornerstones of the modern days fluid dynamics. Regarding this original theory, most fundamental research has been performed with smooth-wall bounded flows. However, materials applied in industry and practice rarely has the smooth-surface properties and makes this theory inconclusive. Nikuradse [5], Colebrook and White [6] and Moody [7] investigated the effect of surface roughness (ϵ) in wall-bounded flows and indicated the change in general behaviour of the fluid motions. Wall-roughness can induce an earlier onset of turbulence and may cause additional friction losses in turbulent flows, with both dependent on the dimensionless roughness parameter $\epsilon/\mathscr{L}$ and the Reynolds number Re. For turbulent flows, wall roughness breaks up the viscous sublayer and forces the log region of the velocity profile to shift outwards, which is associated with a frictional drag increase.

Frequently inspired by nature, specific "rough" surfaces have the ability to reduce the frictional drag [8] and induce a different flow behaviour than the aforementioned rough

[1] Historical outline based on White [1].

wall-bounded flow theory. In the near-wall region, the fluid motions impose the level of turbulence, where in particular the velocity fluctuations in the boundary layer determine the magnitude of turbulent shear stress. The so-called drag-reducing methods interfere with the random fluid motions and consequently reduce the viscous energy dissipation. Some bio-inspired methods that are capable of suppressing the wall-bounded turbulent activities are: Superhydrophobic surfaces ('Lotus leaf'), which are geometrically structured surfaces in combination with a hydrophobic surface chemistry [9]. The wall-bounded flow experiences slip at the fluid-solid interface due to possible trapped air pockets between the surface structures. Another well-studied drag reducing method is the use of riblet surfaces ('shark skin'), which consist of small wall protrusions that are aligned in the streamwise flow direction [10]. They suppress the friction by reducing the spanwise fluid motions near the surface, thereby moving turbulent vortices further away from the wall. Lastly, an example of a surface that interacts with the turbulent flow in the near wall region is the imitation of a dolphin skin, which acts as a compliant wall [11]. It is suggested that the formation of bursting events is likely to be obstructed by the compliant wall, which suppresses the velocity fluctuations and reduces the accompanying Reynolds stress. The last two surface modifications, riblets and compliant surfaces, have been applied in the current research.

1.2. RESEARCH OBJECTIVES

The main research goal was to study drag-modifying surfaces applied to turbulent flows. Part of the research was carried out within the framework of fluid mechanics in sports, where a small reduction of frictional drag results in significant enhancement of sport performances. Furthermore, functional surfaces are applicable to pipe systems and ship vessels to reduce frictional drag, avoid marine fouling and improve heat distribution or exchange. Suitable experimental test facilities in combination with (optical) measurement techniques were selected and developed, in order to measure the frictional drag and to investigate the interaction between the functional surface and the turbulent flow.

The objective of the current study is two-fold. The first research topic covers the investigation of Taylor-Couette flow as a simple and quick measurement tool in order to quantify the frictional drag performance of functional surfaces. In particular, the classical sawtooth riblet textures under steady and unsteady turbulent flow conditions were studied. Specific questions to investigate are: How much frictional drag can be reduced under steady and unsteady flow conditions? What are the flow modifications when drag-reducing surfaces are applied? What are the typical artefacts of the test facility that define the flow behavior and influence the obtained drag measurements? What is the scaling relation between the shear stress and the dimensionless parameters of periodic driven flows?

The second research objective was to quantify the dynamic interaction between a compliant wall and the near-wall turbulent flow. An enumeration of several research questions arises: Will the shear stress be influenced and possibly be reduced by the application of compliant surfaces? What physical mechanism evokes the initial surface deformation? What are the wall dynamics in relation to the turbulent fluid dynamics? What are the motion characteristics of the surface in contrast to the global flow con-

ditions? How are the generated surface deformations related to the properties of the compliant material? What conditions generate flow-induced surface-instabilities? In which way does the wall dynamics manipulate the near-wall flow motions? What is the interrelationship between the wall motions, the near-wall fluid dynamics and the accompanying shear stress?
The combination of the applied surface modifications, test facilities and optical measurement methods remains a recurring subject in this research thesis. The combined implementation is considered and discussed, in order to obtain the relevant wall and fluid dynamics interpretation. Finally, this study is also an attempt to bridge the general gap between scientific research and promising industrial/societal applications. The acquired knowledge will contribute to new insights and innovations in research, development and other related activities.

1.3. OUTLINE OF THE THESIS

This thesis consists of five chapters, which can roughly be divided into two parts. The first part elaborates on the research accomplished with the Taylor-Couette facility under steady flow conditions (Chapter 2) and periodically driven turbulent flow conditions (Chapter 3). The second part describes the investigation and assessment of the water tunnel and accompanying turbulent flow (Chapter 4), as well as the accomplished investigation on compliant surfaces under turbulent shear flow conditions (Chapter 5). Chapter 6 summarizes the conclusions of this thesis.
Chapter 2 describes the Taylor-Couette facility and discusses the application of Tomographic Particle Image Velocimetry (tomo-PIV) that measures the three velocity components of the fluid flow. The presence of large-scale flow structures are linked to the torque measurements in order to determine the suitable turbulent flow regime to perform the frictional drag study of functional surfaces. The drag performance of a riblet surface under steady turbulent flow conditions is studied and shows to generate a bulk fluid rotation. This rotation effect is quantified by introducing a simple model based on the drag performance, which is subsequently verified by PIV measurements. Appendix A.1 provides the general background information on relevant flow structures and torque scaling in relation to the operating conditions (i.e. Re_s and R_Ω). The validation of the applied assumptions and the correction methods for the current Taylor-Couette facility is discussed in Appendices A.2, A.3 and A.4.
Unsteady turbulent Taylor-Couette flow due to sinusoidally driven cylinders is discussed in **Chapter 3**, wherein the relation between the frictional drag and the governing parameters for periodically driven boundaries is explored. Besides the shear Reynolds number Re_s, the oscillatory Reynolds number Re_{osc} and the Womersley number Wo are introduced as scaling parameters, which are based on the velocity amplitude ΔU_{sh} and the oscillation period T, respectively. Furthermore, the riblet performance to reduce frictional drag under periodically driven flow conditions is studied and evaluated.
Chapter 4 describes the application of the water tunnel facility and the two measurement techniques: (i) drag force measurements to indicate the averaged surface friction and (ii) planar Particle Image Velocimetry (planar-PIV) to reconstruct the fluid motions in the bulk and the near-wall region. These two measurement techniques are relevant tools to characterize the test plates and the water tunnel.

The investigation of the dynamic interaction between a compliant coating and the near-wall turbulent flow is reported in **Chapter 5**. Two optical measurements methods are made applicable in order to study the relevant wall motions and fluid dynamics, which are Background-Oriented Schlieren (BOS) and planar Particle Image Velocimetry (planar-PIV), respectively. The wall and the fluid motions are coupled to the surface drag force and jointly elucidate the physical mechanism of the onset of surface instability.
Finally, **Chapter 6** summarizes the conclusions of this thesis regarding the two research topics. Additionally, an outlook is presented for further research on drag-modifying surfaces, as well as possible implementation of the developed knowledge to create a value proposition for prospective industrial activities.

REFERENCES

[1] F. M. White, *Fluid mechanics* (WCB, 1999).

[2] G. Hagen, *Über die bewegung des wassers in engen cylindrischen röhren,* Annalen der Physik **122**, 423 (1839).

[3] O. Reynolds, *An experimental investigation of the circumstances which determine whether the motion of water shall be direct or sinuous, and of the law of resistance in parallel channels,* Philosophical Transactions of the Royal society of London , 935 (1883).

[4] L. Prandtl, *Über flussigkeitsbewegung bei sehr kleiner reibung,* Verhandl. III, Internat. Math.-Kong., Heidelberg, Teubner, Leipzig , 484 (1904).

[5] J. Nikuradse, *Similarity for turbulent flow in smooth pipes,* VDI-Forschungsheft (1932).

[6] C. Colebrook and C. White, *Experiments with fluid friction in roughened pipes,* Proceedings of the Royal Society of London. Series A-Mathematical and Physical Sciences **161**, 367 (1937).

[7] L. F. Moody, *Friction factors for pipe flow,* Trans. Asme **66**, 671 (1944).

[8] D. M. Bushnell and K. Moore, *Drag reduction in nature,* Annual Review of Fluid Mechanics **23**, 65 (1991).

[9] J. P. Rothstein, *Slip on superhydrophobic surfaces,* Annual Review of Fluid Mechanics **42**, 89 (2010).

[10] B. Dean and B. Bhushan, *Shark-skin surfaces for fluid-drag reduction in turbulent flow: a review,* Philosophical Transactions of the Royal Society of London A: Mathematical, Physical and Engineering Sciences **368**, 4775 (2010).

[11] M. Gad-el Hak, *Compliant coatings for drag reduction,* Progress in Aerospace Sciences **38**, 77 (2002).

2

TURBULENT TAYLOR–COUETTE FLOW OVER RIBLETS

An adapted version of this chapter has been published in Experiments in Fluids **56** [1].

2.1. INTRODUCTION

The reduction of wall friction in turbulent flows has remained an interesting subject for researchers over the last decades. Applications may be particularly relevant to industrial devices to reduce the pressure drop in pipe flows, as to decrease fuel consumption and/or to increase transfer speed for transport vehicles. Substantial energy savings for these industries would lead to ecological and economical benefits.

Windtunnels and fluid channels are qualified test facilities to perform turbulent drag reduction studies [2]. However, the forces and the force differences are small and require accurate force measurements in combination with large test surfaces, and these are often the most time-consuming and expensive parts of the research process. An alternative experimental setup for a study of turbulent drag reduction that is compact, accurate and easy-to-use is a Taylor-Couette system. Several researchers have investigated and reported drag reduction measurements of a flow between two coaxial cylinders, although not all under comparable operational conditions. Experiments with polymers [3], riblets [4], surfactants [5], highly hydrophobic surfaces [6] and air bubbles [7] are successfully performed and indicate the Taylor-Couette facility as a suitable experimental setup to study drag reducing methods.

The flow in a Taylor-Couette facility presents a flow between two rotating coaxial cylinders. For high Reynolds numbers, the turbulent flow between these presumably infinite long plates in azimuthal direction, has a fully developed turbulent shear flow boundary layer. The fluid generates a shear stress on the surfaces that can be determined by measuring the torque on the (inner) cylinder surface.

Andereck *et al.* [8] distinguished and characterized multiple flow regimes and compiled a complex flow pattern diagram. Many parameters influence the different flow states, such as the inner and outer cylinder velocity, the gap ratio, the aspect ratio, the end effects and the initial conditions before flow transition between the regimes. Torque scaling research identified the relation between the flow structures and measured torque [9–11]. Ravelet *et al.* [12] demonstrated strong dependency of the friction coefficient C_f as a function of the Reynolds number Re_s and the rotation number R_Ω, due to the change of turbulent flow structures and their interactions, which was verified by Tokgöz [13].

In this paper, we discuss our Taylor-Couette facility as an easy-to-use experimental instrument to measure the drag on surfaces. Turbulent drag changes are identified for an adhesive riblet film in the moderate to highly turbulent flow regime (up to $Re_s \approx 1.5 \cdot 10^5$). We observe a modification in rotation number for the same mean shear rates due to the use of riblets on the inner cylinder.

In Section 2.2, the experimental and PIV setup are described. We explain the specific parameters and relevant effects for a Taylor-Couette (TC) facility in Section 2.3. Then, in Section 2.4, we discuss the investigation of the TC facility by torque and PIV measurements. We analyse, discuss and validate the results of surface modification with riblets on the inner cylinder and propose a simple model to determine the rotation effect in Section 2.5. The main conclusions are summarized in Section 2.6.

2.2. TAYLOR-COUETTE FACILITY AND PIV SETUP

2.2.1. TAYLOR-COUETTE FACILITY

The TC facility in the present study was previously used in the investigation of Delfos *et al.* [14], Ravelet *et al.* [12] and Tokgöz [13]. It consists of two coaxial acrylic glass cylinders that both can rotate independently. The inner cylinder is sealed by PVC end-plates at the top and bottom. The radius of the inner cylinder is $r_i = 110$ mm and total length $L_i = 216$ mm. The outer cylinder has a radius $r_o = 120$ mm and a length $L_o = 220$ mm (Fig. 2.1). The inner cylinder is assembled within the outer cylinder with high precision; the shaft is secured by two ball bearings at the top, while the bottom remains centered and stabilized by a polymer ball bearing in the bottom end-plate of the inner cylinder. The radial gap between the cylinders is $d = r_o - r_i = 10.0$ mm, and hence the gap ratio is $\eta = r_i / r_o = 0.917$ and axial aspect ratio is $\Gamma = L_i / d = 21.6$.
The system is closed by end-plates attached to the outer cylinder and are rotating with the outer cylinder. The gaps between the top and bottom end-plates of the inner and outer cylinder are around $h = 2$ mm and are called the *von Kármán*-gaps. The fluid motions in these horizontal gaps (i.e. von Kármán flow) create an additional fluid friction on the cylinders during rotation [15–17]. The mechanical friction of the system bearings can be neglected compared to the total fluid friction in the system, as was verified with an empty system. The total torque (M_{Tot}) on the inner cylinder is recorded with a co-rotating torque meter (HBM T20WN/2Nm, abs. precision ±0.01 Nm) that is assembled in the shaft between the driving motor (Maxon, 250W) and inner cylinder. The outer cylinder is driven by an identical external motor via a driving belt.

The shear stress τ is among others influenced by the temperature-dependent fluid viscosity. During measurements, we observe the temperature change of the working fluid closely as we are not able to control the fluid temperature. When the cylinders are at

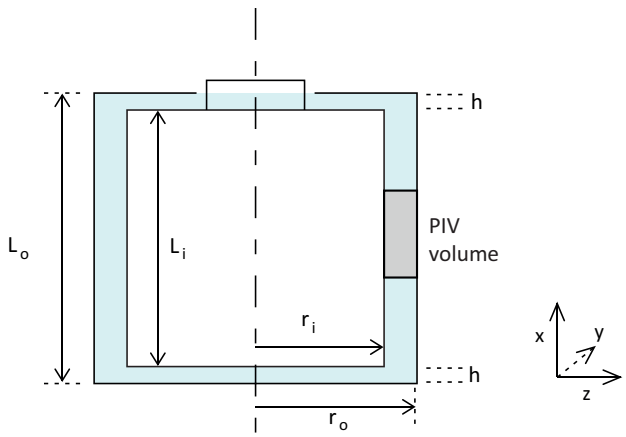

Figure 2.1: Sketch of the Taylor-Couette facility in the radial-axial plane. The coordinate system in the measurement volume is given by x for axial, y for azimuthal and z for radial direction. The dimensions are not to scale.

Table 2.1: Glycerol/water fluid properties: Mass fraction glycerol, fluid viscosity at 20 °C, heat capacity coefficient and viscous sensitivity of temperature change (20-25 ^{o}C).

Mixture	C_m (wt%)	$10^6 \times \nu$ (m^2/s)	c_p (kJ/(kg K))	$\partial(\nu/\nu_0)/\partial T$ (%/K)
5	85.9	100	2.68	-6.6
4	62.1	10.8	3.09	-4.3
3	52.6	6.09	3.26	-3.7
2	38.9	3.19	3.50	-3.2
1	17.1	1.53	3.88	-2.6
0	0	1.01	4.18	-2.4

rest, the fluid temperature T_f is manually measured via an opening in the top lid by a thermocouple (RS, type K) connected to a digital thermometer (RS1319A). When the cylinders are rotating, it is not possible to measure the fluid temperature directly since the system is completely closed. Instead, the outside wall temperature $T_{out}(t)$ of the outer cylinder is recorded in time by an infrared-thermometer (Calex PyroPen). The fluid temperature $T_f(t)$ is indirectly determined via heat transfer calculations, based on the material and fluid properties of the setup. At the end of a measurement, the temperature value is verified by manual temperature measurement as described before and agrees very well (±0.2°C). The determined fluid temperatures $T_f(t)$ are used to estimate the correct value of the working fluid viscosity during torque measurements. The working fluids in the present study are various glycerol-water mixtures, with a kinematic viscosity in the range of $1.0\times10^{-6} < \nu < 100\times10^{-6}$ m^2/s at 20 °C (Table 2.1). Experiment control and data acquisition (DAQ) are accomplished with a desktop computer. The two motors are controlled by a software program (LabVIEW, National Instruments Corp.) that regulates the desired angular velocities of the inner and outer cylinders. The torque meter is connected via a DAQ block (NI PCI-6035E) to a 12 bit DAQ board (NI BNC-2110) that records the torque and rotation rate signal of the inner cylinder at a sampling rate of 2 kHz for 120 seconds. Simultaneously, the outside wall temperature signal $T_{out}(t)$ of the IR-thermometer is recorded by a manufacturer supplied software (Calexsoft 1.05).

2.2.2. PIV SETUP

The three velocity components in the instantaneous flow field can be measured by tomographic particle image velocimetry (tomo-PIV, Elsinga *et al.* [18]). The application of the tomo-PIV to Taylor-Couette is shown in Figure 2.2 and is described in more detail by Tokgöz [13]. Particle images were recorded with four cameras (Imager Pro X 4M) in double frame mode with a resolution of 2000 × 2000 pixels. A double-pulsed Nd:YAG laser (New Wave Solo-III) was used to illuminate the measurement volume between the two cylinders with a volume size of roughly $40 \times 20 \times 10$ mm^3 in axial, azimuthal and radial directions. The measurement volume is located at mid-height of the rotational axis to minimize the possible end effects of the Taylor-Couette facility on the measurements (Fig. 2.1).

Fluorescent particles (Fluostar) with a mean diameter of 15 μm were used as tracer particles. The seeding concentration was around 0.025 particles per pixel. This is considered to be an optimal seeding concentration to achieve a high spatial resolution and rule out speckle effects in the recorded images [19]. The sharp contrast between the intensity inside and outside the volume gap in radial direction indicates a high quality of the tomographic reconstruction.

For the calibration procedure a stainless steel flat plate of 1 mm thick was used as a calibration target with 0.4 mm circular holes in repetition at every 2.5 mm in the vertical and horizontal directions. The calibration target was stably-attached to a translating and rotating microtraverse, capable to position the target with high precision. Calibration images were recorded in three selected planes in the radial direction, with 2.5 mm distance in-between.

The quality of the recorded images was improved by image processing using commercial software (Davis by LaVision). The signal to noise ratio was increased by first subtracting a sliding minimum intensity of 25×25 pixels from all images followed by a 3×3 -pixel Gaussian smoothing filter. Tomographic reconstruction was performed with the MART algorithm [18]. A multipass correlation was used with a final interrogation window of $40 \times 40 \times 40$ voxels with a 75% overlap. The universal outlier detection method [20] removed spurious vectors and the resulting gaps were filled by linear interpolation.

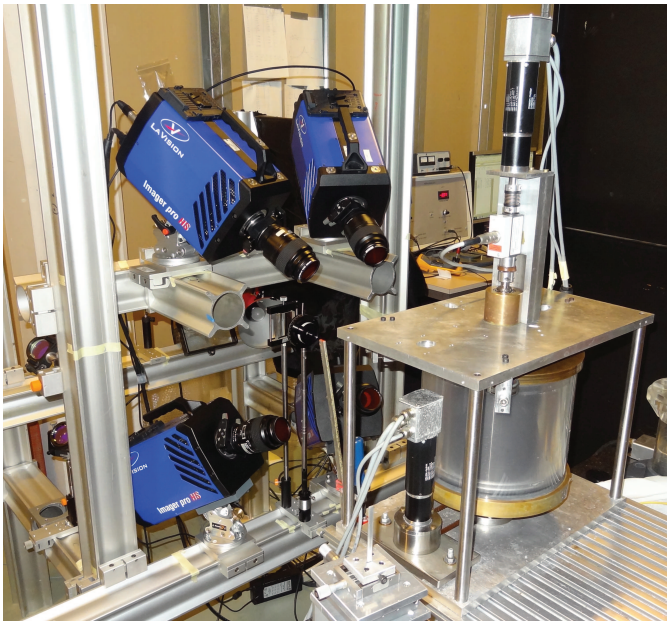

Figure 2.2: Experimental setup with PIV cameras. The cameras on the photo differs from the cameras mentioned in the text.

2.2.3. RIBLETS

Longitudinal ribbed surfaces, called riblets, are able to reduce the skin friction in a turbulent boundary layer in comparison to smooth surfaces [21]. The reduction depends on the dimensions and geometry of the riblets in relation to the local flow. The riblet spacing Reynolds number, or dimensionless riblet spacing, is traditionally defined by the parameter $s^+ = su_\tau/\nu$, where s is the riblet spacing, u_τ ($= \sqrt{\tau_{w,0}/\rho}$) is the friction velocity. The drag reduction is expressed in the change of shear stress compared to a smooth surface ($\Delta\tau_w/\tau_{w,0}$). Several types of riblet geometries are known, which can typically reduce the skin friction up to 5-10%.

In this study we use a 3M Scotchcal High Perfomance film with longitudinal grooves as riblet surface, which has been used in previous research [22]. A picture taken with scanning electron microscopy (SEM) shows a triangular cross-section geometry of the riblets with a spacing $s = 120$ μm and height $h = \pm 110$ μm (Fig. 2.3). The rib tips have a noticeable round/flat area, which can have a negative effect on the drag reducing performance of riblets [21].

The film is adhered to the surface with high precision to avoid air pockets and misalignment of the grooves, which should be parallel to the azimuthal flow. A small axial-aligned gap of roughly 0.3 mm is observed between the edges of the film and makes an irregularity in the cylinder surface. However, the film gap is very small and the torque contribution of the present gap is considered to be marginal. The total film thickness measured from the bottom of the sheet to the tops of the riblet is 190 μm and the adhered riblet film results in a small change of the inner cylinder radius and the radial gap, which is taken into account for the experimental conditions.

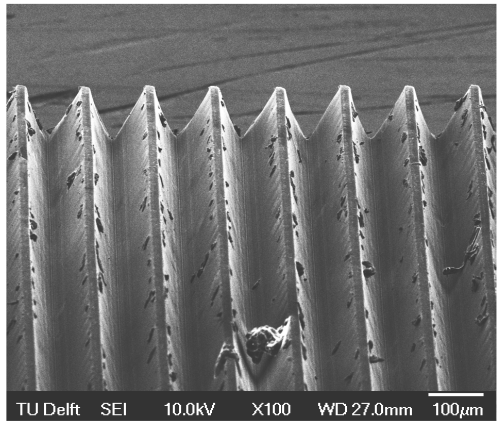

Figure 2.3: SEM picture of sawtooth riblet surface, view-angle 70 degrees. Riblet spacing 120 μm, riblet height ± 110 μm. Rib-tip to spacing ratio $t/s \simeq 0.1$. SEM image taken by C. Kwakernaak (3mE-TU Delft).

2.3. SPECIFIC PARAMETERS AND RELEVANT TAYLOR-COUETTE EFFECTS

In this section, we describe the control parameters that applies to rotating shear flows in general. The flow characteristics are determined by the angular velocities and radii of the inner and outer cylinders, the gap between the cylinders and the fluid viscosity. The use of finite length cylinders induces end effects on the torque measurements and creates flow instabilities.

2.3.1. REYNOLDS AND ROTATION NUMBERS

The shear Reynolds number of Taylor-Couette flows is comparable with the Reynolds number of plane Couette flows in a rotating frame. Dubrulle *et al.* [23] introduced a new set of control parameters based on dynamical rather than the traditional geometrical considerations. Traditionally based on the gap width $d = r_o - r_i$ between the two cylinders, the inner and outer cylinder Reynolds number are respectively defined as $Re_i = (r_i \omega_i d/\nu)$ and $Re_o = (r_o \omega_o d/\nu)$, where ω_i and ω_o are the angular velocities and ν is the kinematic viscosity of the fluid. The sign of the Reynolds number indicates the rotation direction of the cylinders. The parameters are combined to introduce the dynamical control parameters: the shear Reynolds number Re_s, rotation number R_Ω and curvature number R_C are defined as:

$$Re_s = \frac{2}{1+\eta} \left| \eta Re_o - Re_i \right| \tag{2.1}$$

$$R_\Omega = (1-\eta) \frac{Re_i + Re_o}{\eta Re_o - Re_i} \tag{2.2}$$

$$R_C = \frac{1-\eta}{\eta^{1/2}} \tag{2.3}$$

The shear Reynolds number Re_s is based on the shear rate between the inner and outer cylinder. The rotation number R_Ω indicates the net system rotation and represents the influence of the mean rotation on the shear. The rotation condition strongly influences the formation of flow structures in the radial gap and the corresponding shear stresses (see Appendix A.1). The sign of the rotation number defines the case of cyclonic ($R_\Omega > 0$) or anti-cyclonic ($R_\Omega < 0$) flows. For inner and outer cylinder rotation only, the rotation numbers are $R_{\Omega,i} = \eta - 1$ and $R_{\Omega,o} = (1-\eta)/\eta$ respectively. In case of exact counter-rotation ($r_i \omega_i = -r_o \omega_o$), the rotation number R_Ω is zero and indicates that the mean bulk velocity $\bar{U}_b$ is zero. The curvature number, dependent on the gap ratio η, indicates the effect of the cylinder radii on the stability of circumferential flows. The cylinder gap d in our setup is considered to be narrow, with a gap ratio $\eta = r_i/r_o \simeq 0.917$, i.e. close to unity. The curvature number in our experiments is therefore $R_C \simeq 0.087$.

2.3.2. TORQUE CONTRIBUTION OF THE *Taylor-Couette* AND *von Kármán* FLOWS

The fluid inside the experimental setup is distributed into two main regions: the gap between the inner and outer cylinder wall (Taylor-Couette gap) and the gap between the end plates of the cylinders (von Kármán gap). The fluid motions in these regions are very different and demands an other type of methodology to obtain the shear forces working on the inner cylinder.

The torque on the cylinder walls (M_{TC}) is defined by the wall shear stress τ_w multiplied by the surface area of the cylinder A and lever arm r:

$$M_{TC} = 2\pi L_i r_i^2 \tau_{w,i} = 2\pi L_i r_o^2 \tau_{w,o} \tag{2.4}$$

The skin friction coefficient C_f is a dimensionless parameter, which is used to analyze drag changes when the surface of the inner cylinder is modified. The friction coefficient C_f is the ratio of wall shear stress τ and the dynamic pressure $\frac{1}{2}\rho U_{sh}^2$ [12]:

$$C_f = \frac{M_{TC}}{\pi \rho r_i^2 L_i U_{sh}^2} \tag{2.5}$$

In Equation 2.5 the shear velocity U_{sh} is proportional to $Re_s \nu/d$. Equation 2.5 represents the friction coefficient for laminar and turbulent flow conditions. The analytical solution of the friction coefficient for laminar flow, with shear velocity $U_{sh} = \omega_o r_o - \omega_i r_i$ is given by:

$$C_f = \frac{4\nu(\omega_o - \omega_i)}{(1-\eta^2)(\omega_o r_o - \omega_i r_i)^2} \tag{2.6}$$

The fluid motions in the horizontal von Kármán gap (vK-gap) create an additional fluid friction on the cylinders. The shear flow between the end-plates applies a torque on the inner cylinder end-plates with radius r_i, with the outer cylinder end-plates rotating at a gap height h in between. The torque on the inner cylinder under laminar flow conditions realized by the fluid motion in the vK-gap can be expressed by:

$$M_{vK} = \frac{\pi \rho \nu (\omega_o - \omega_i) r_i^4}{2h} \tag{2.7}$$

Combining Equations 2.5-2.7 gives the ratio between the torque contribution of the two vK-gaps and the TC-gap for laminar flows, considering the gap height of the bottom and top vK-gap (h) to be similar:

$$\frac{2M_{vK}}{M_{TC}} = \frac{r_i^2(1-\eta^2)}{4hL_i} \tag{2.8}$$

Equation 2.8 shows that the measured torque M_{tot} becomes more dependent of the fluid friction in the TC-gap when the vK-gap height $h \to \infty$ or when $L_i \to \infty$. Under laminar flow conditions, the described experimental setup has a torque ratio of $M_{vK}/M_{TC} \simeq 1$.

For turbulent flow conditions, the torque contribution of the von Kármán gaps is assumed to be independent of R_Ω and is estimated to be equal to half of the measured torque at $R_\Omega = 0.091$, as suggested by Tokgöz [13]. This assumption is compared to the results of Daily and Nece [15]. They studied the flow regimes in the axial gap between a rotation disk enclosed within a right-cylindrical chamber, and it was verified that the disk friction coefficient $C_{f,disk}$ is a function of the disk Reynolds number $Re_d = |\Delta\omega| r_i^2/\nu$ and the axial spacing/disk radius ratio h/r_i. Figure 2.4 shows the relation between $C_{f,disk}$ and Re_d for an axial spacing/disk radius ratio $h/r_i = 0.02$.

The measured torque of only outer cylinder rotation ($R_\Omega = 0.091$) of Ravelet *et al.* [12] is used to determine the disk friction coefficient $C_{f,disk}$ of the end-plate in the von Kármán gap for the current setup. Figure 2.4 indicates that the assumption fits reasonably well to the results found by Daily and Nece [15]. This was validated by additional torque measurements with substantial longer cylinders, maintaining a similar gap distance h between the end-plates (see Appendix A.2).

The torque of the fluid motions in the von Kármán gap M_{vK} for the current setup is estimated by:

$$M_{vK} = C_{f,disk} \frac{1}{5} \pi \rho \left(\omega_o - \omega_i\right)^2 r_i^5 \tag{2.9}$$

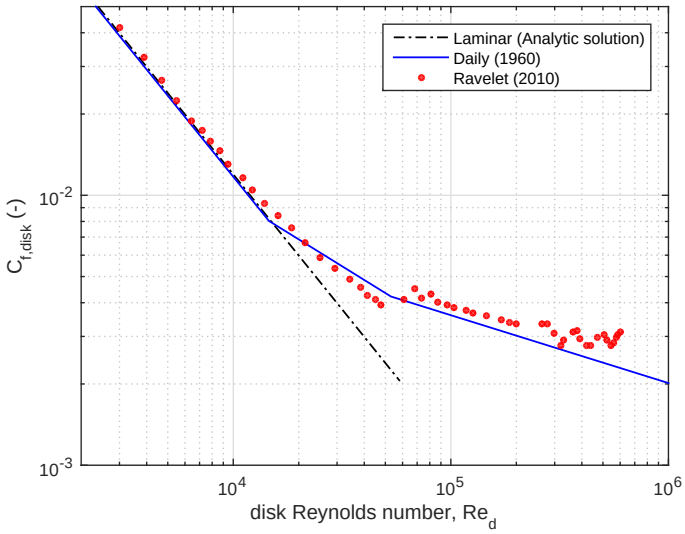

Figure 2.4: The von Kármán disk friction coefficient $C_{f,disk}$ as a function of the disk Reynolds number $Re_d = |\Delta\omega| r_i^2/\nu$ for an axial spacing/disk radius ratio $h/r_i = 0.02$.

2.3.3. AZIMUTHAL VELOCITY PROFILE

Taylor derived an exact solution for the laminar azimuthal velocity profile of the flow between two infinitely long coaxial cylinders [24]. In practice the cylinders have a finite length and the azimuthal flow experiences disturbances from the fluid motions in the horizontal vK-gaps that penetrates into the vertical TC-gap, causing a secondary flow. This leads to flow instabilities at lower Reynolds number than the theoretical predicted critical Reynolds number for flow transitions [25]. It is assumed that the end-effects will not influence the bulk profile in the turbulent regime as a secondary flow is much weaker than the turbulent fluid motions.

The turbulent velocity profile of the azimuthal flow is more complex. Dong [26] performed 3D direct numerical simulations of the turbulent flow between exact counter-rotating cylinders ($R_\Omega = 0$) with a gap ratio $\eta = 0.5$ at moderate Reynolds numbers that correspond to featureless turbulence and unexplored turbulent regions in the flow pattern diagram of Andereck *et al.* [8]. They report an asymmetrical azimuthal velocity profile at the cylinder walls and a core flow which has near-zero azimuthal velocities at higher Reynolds numbers. This region of near-zero azimuthal velocities expands as the Reynolds number increases. The velocity profile approaches a linear line with slope α in the core of the flow ($U_{\theta,bulk}(r) = \alpha(r - r_i)/d$) and the location of the surface with zero azimuthal velocities shifts outwards when the Reynolds number were increased, with a limiting value of $(r^* - r_i)/d \sim 0.55$.

2.4. INVESTIGATION OF THE EXPERIMENTAL CONDITIONS

2.4.1. EXPERIMENTAL CONSIDERATIONS

In order to make a proper drag performance comparison, it is preferable to measure the riblet surfaces under similar flow conditions as for boundary layer or fluid channel experiments. Global rotation, which is the rotation of the frame of reference in which the shear flow occurs, can strongly influence the turbulent structures [27]. With regard to a Taylor-Couette set-up, global rotation can enhance or suppress turbulence for only inner or outer cylinder rotation respectively. Therefore the measurements are performed under exact counter-rotation, with a rotation number $R_\Omega = 0$.

Frictional heating causes thermal effects on the estimation of the correct fluid viscosity, as was mentioned by Hall [4]. Nevertheless, a flow under exact counter-rotating conditions is indicated as highly turbulent and therefore well-mixed, resulting in a constant fluid temperature over the radial gap. The fluid temperature $T_f(t)$ is indirectly determined via heat transfer calculations and deviates maximum ± 0.2°C from the actual fluid temperature when checked manually. For common turbulent flows, the friction coefficient C_f scales with $Re^{-1/4}$ and results in a maximum error of the friction coefficient of $0.1 - 0.3\%$ due to the temperature deviation.

The drag-reducing material, in this case the riblet film, is only applied on the inner cylinder surface as it is much easier, faster and more accurate to apply. The outer cylinder surface remains unaltered, as the riblet film is also non-transparent and inhibits PIV-measurements. A consequence is that the inner and outer cylinder surfaces have different skin-friction coefficients and modify the condition for the rotation number R_Ω of exact counter-rotation. This is discussed in Section 2.5.1.

2.4.2. TORQUE MEASUREMENTS

For all Reynolds numbers, the torque contribution of the TC-gap is determined by the time-averaged values of the measured torque minus the torque values of the vK-gap at $R_\Omega = 0.091$, and are used to determine the friction coefficients C_f. Figure 2.5 shows the friction coefficient C_f of an untreated, smooth cylinder surface as a function of the shear Reynolds number Re_s for a rotation number $R_\Omega = 0$. The current data is identical to the data of Ravelet *et al.* [12] and is similar to the results of planar-Couette flow [28]. The friction coefficients in Figure 2.5 are used as a reference to identify drag changes due to surface modification of the inner cylinder. The results of the friction coefficient C_f are reproducible within 0.6% for all working fluids. At low Reynolds numbers ($Re_s < 400$) the curve is identical to the theoretically predicted curve of C_f (Eq. 2.6) and validates the torque contribution of 50% of the TC-gap. The measured torque for laminar flow is linear with the relative angular velocity and scales as $C_f \sim 1/Re$. The first flow transition already occurs at $Re_s \simeq 400$, which is lower than the theoretical value of $Re_s = 515$ [25]. We believe that the finite aspect ratio induces secondary flow that creates an earlier state of instability. A transitional regime arises between $Re_s \sim 400$ and 1000, and above $Re_s > 1000$ the friction coefficient scales with $C_f \sim Re^{-1/2}$. A second flow transition occurs around $Re_s \sim 4000$ and for higher Reynolds numbers the curve scales with $C_f \sim Re^{-1/4}$. The flow is considered to be fully turbulent under these conditions.

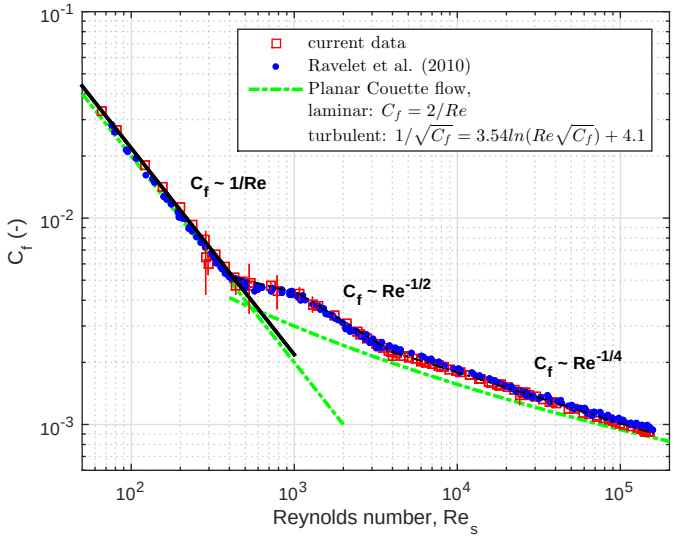

Figure 2.5: Friction coefficient C_f as a function of shear Reynolds number Re_s under exact counter-rotation ($R_\Omega = 0$). Errorbars represent the estimated 95% confidence interval. The solid black line represents the analytical solution for laminar flow and scales with $C_f \sim 1/Re$. The Taylor and fully turbulent regime are scaled with $C_f \sim Re^{-1/2}$ and $C_f \sim Re^{-1/4}$ respectively. Current data compared to the data of Ravelet *et al.* [12] and plane-Couette flow. Laminar plane-Couette flow, $C_f = 2/Re$. Turbulent plane-Couette flow, $1/\sqrt{C_f} = 3.54 \ln(\mathrm{Re}\sqrt{C_f}) + 4.1$ [28].

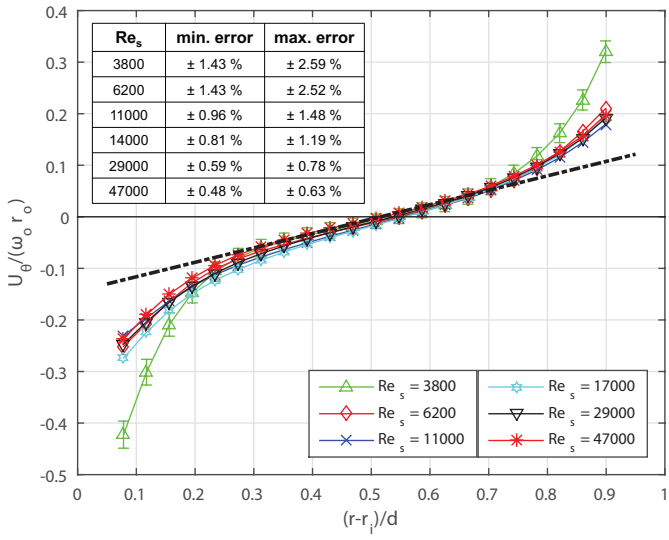

Figure 2.6: Averaged azimuthal velocities under exact counter-rotation ($R_\Omega = 0$) as a function of the radial position. The velocities are normalized to the azimuthal velocity of the outer cylinder ($\omega_o r_o$). The minimum and maximum estimated 95% confidence intervals of the azimuthal velocity data are presented in the table. Errorbars are only shown for $Re_s = 3800$. The dashed line represents the azimuthal core flow velocity for turbulent flows, with slope $\alpha \approx 0.25$.

2.4.3. VELOCITY PROFILE: PIV MEASUREMENTS

The three velocity components of instantaneous flow fields are obtained by tomo-PIV measurements. The reliability of the tomo-PIV method of this experimental setup has been evaluated and described by Tokgoz *et al.* [19]. In the past, riblet surfaces have been successfully applied to reduce skin friction in turbulent boundary layers and therefore turbulent velocity components in the TC-gap are highly interesting to investigate. We have used PIV data of turbulent flow at Reynolds numbers $Re_s = 3800$ to 4.7×10^4 under exact counter-rotating conditions ($R_\Omega = 0$), which were presented previously by Tokgoz *et al.* [19]. The averaged velocities of the azimuthal flow as a function of the radial position are given in Figure 2.6. The velocities are obtained by averaging over 1000 instantaneous 3D velocity fields and in axial direction. Data points close to the walls are excluded from the measured domain as they are not reliable due to optical distortions. The minimum and maximum estimated 95% confidence intervals of the azimuthal velocity data are listed in the table of Figure 2.6. The minimum and maximum errors are related to the data points in the core flow or close to the walls respectively. The averaged azimuthal velocity profiles suggest high velocity gradients near both walls and low velocity gradients in the middle of the gap (core flow). The velocity gradient at the wall increases by increasing the Reynolds number Re_s, which indicates a higher level of turbulence. The zero-crossing where the averaged azimuthal velocity changes from negative to positive is around $(r^* - r_i)/d \sim 0.52 - 0.56$ for all cases. The core of the flow has very low azimuthal velocities and when the Reynolds number in-

creases, the azimuthal velocity profile of the core flow approaches a straight line with slope $\alpha \approx 0.25$, indicated by the dashed line in Figure 2.6. The averaged axial and radial velocity profiles are within a maximum value of 0.6% of the outer cylinder wall velocity. The instantaneous PIV data shows axial and radial velocity fluctuations of $\pm 10-20\%$ of the outer cylinder wall velocity.

Figure 2.7 presents the azimuthal vorticity and the velocity vectors of the time-averaged flow in the radial-axial plane of the gap. The presence of large-scale structures is clearly visible at $Re_s = 3800$, which are counter-rotating Taylor vortices with a diameter comparable to that of the TC-gap width. The structures are much weaker at $Re_s = 6200$ and also small-scale structures arise. The large vortex structures have completely disappeared for fully turbulent flows. The vorticity plots indicate a least limited Reynolds number at which the flow in the Taylor-Couette facility has typical turbulent flow characteristics comparable to channel or pipe flows. The flow at $Re_s = 3800$ and $Re_s = 6200$ have visible Taylor-vortices and therefore the riblet results under these conditions are considered to be an artefact of the experimental setup rather than the drag characteristics of riblets.

In conclusion, Figures 2.5 - 2.7 show that the friction coefficient is strongly related to the flow regime (laminar, Taylor vortices and fully turbulent flow) with different scaling ($C_f \sim Re^{-1}$, $Re^{-1/2}$ and $Re^{-1/4}$ respectively).
Furthermore, the derived riblet data will be limited to $Re_s > 10^4$ in order to make a suitable comparison to data obtained by other researchers.

2.5. RESULTS

Figure 2.8 presents the determined friction coefficients C_f against shear Reynolds number Re_s for smooth and riblet inner cylinder surfaces under exact counter-rotating conditions ($R_\Omega = 0$). For low Reynolds numbers up to $Re_s = 4.0 \times 10^3$, the friction coefficients are slightly higher compared to a smooth surface. For higher Reynolds numbers the friction values are initially lower, while for Reynolds numbers $Re_s > 8.5 \times 10^4$ the values are much higher compared to a smooth surface.

An alternative figure to indicate the drag change is given in Figure 2.9. The change in drag at the inner cylinder surface is determined by:

$$\frac{\Delta\tau_w}{\tau_{w,0}} = \frac{\tau_{w,rib} - \tau_{w,0}}{\tau_{w,0}} = \frac{C_{f,rib} - C_{f,0}}{C_{f,0}} \tag{2.10}$$

A drag reduction is observed for a Reynolds number interval of $Re_s = 4.0 \times 10^3$ to 8.5×10^4, with a maximum apparent drag reduction of 5.3% around $Re_s = 4.7 \times 10^4$. Drag increases in the Reynolds regime with Taylor vortices (Fig. 2.9, inset), as for Reynolds numbers above $Re_s = 8.5 \times 10^4$. A maximum drag increase of 14% is noticed for a Reynolds number $Re_s = 15 \times 10^4$. For further evaluation, the riblet data will be limited to $Re_s > 10^4$ as is stated in Section 2.4.3.

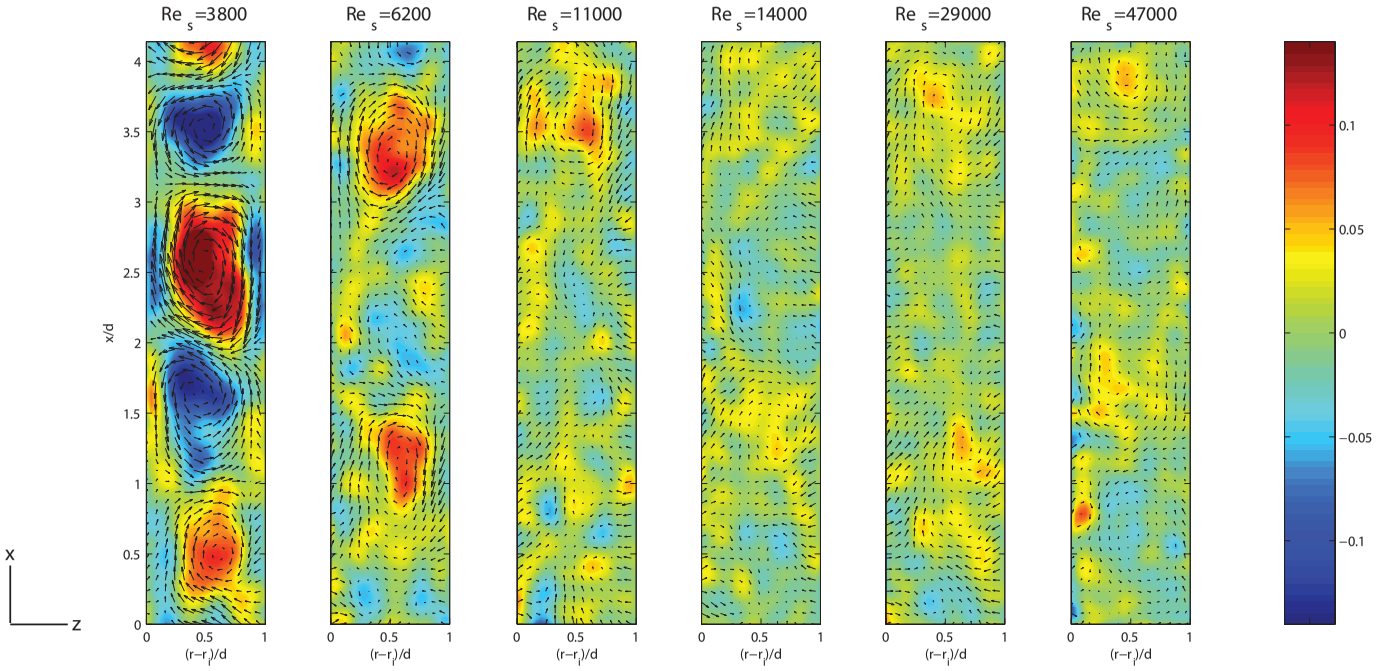

Figure 2.7: Vorticity plot: Color indicates the normalized strength of the out-of-plane vorticity, arrows indicate the radial and axial velocities. The vorticity and velocity in each plot are normalized to outer cylinder wall velocity $\omega_o r_o$ and radial gap length d.

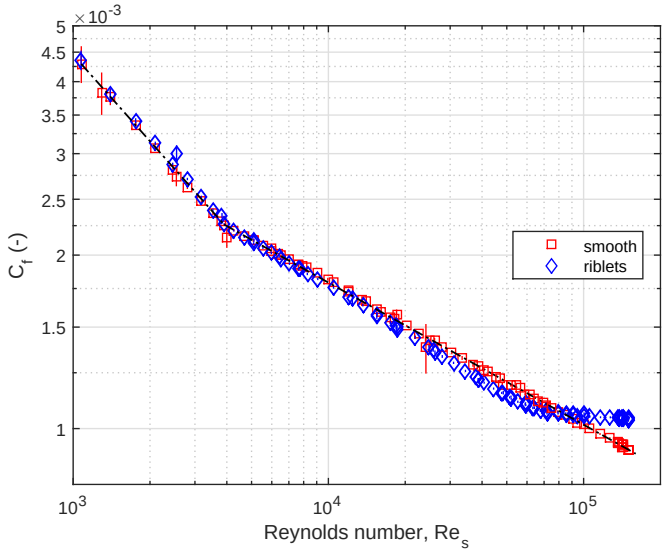

Figure 2.8: Friction coefficient C_f vs shear Reynolds number Re_s under exact counter-rotation ($R_\Omega = 0$) of a smooth (red ∘) and a riblet (blue ⋄) inner cylinder surface, for $Re_s = 1000$ to 15×10^4.

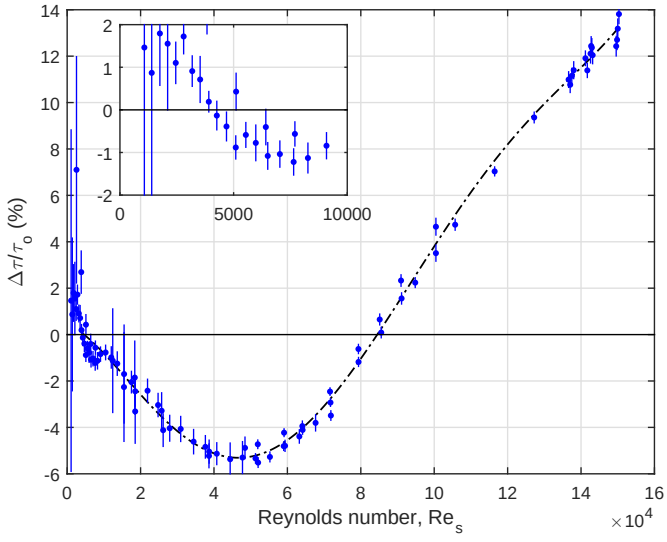

Figure 2.9: Measured drag change under exact counter-rotation ($R_\Omega = 0$). The dashed line represents the polynomial fit. Inset: Zoom-in view around flow transition: Taylor-vortex to turbulent regime. Errorbars: 95% confidence interval.

2.5.1. ROTATION EFFECT

The fluid motions in the TC-gap are driven by the surfaces of the inner and outer cylinder and generate an angular momentum balance, or torque balance ($M_{tc,i} = M_{tc,o}$). Equation 2.4 indicates that the shear stress at the inner cylinder wall is larger than at the outer cylinder wall. The shear stress at the inner cylinder surface is given in Equation 2.11, with $\bar{U}_b$ as the averaged azimuthal bulk/core velocity.

$$\begin{aligned} \tau_w &= \frac{1}{2}\rho\, C_{fi}\, (U_{in} - \bar{U}_b)^2 \\ &= \frac{1}{2}\rho\, C_{fo}\, (U_{out} - \bar{U}_b)^2 \left(\frac{r_o}{r_i}\right)^2 \end{aligned} \tag{2.11}$$

The friction measurements are executed under exact counter-rotation ($U_{out} = -U_{in}$). The azimuthal velocity profile of a smooth inner and outer cylinder surface at Reynolds number $Re_s = 4.7 \times 10^4$ is given in Figure 2.10. The core of the flow shows very low azimuthal velocities and indicates an averaged bulk velocity of zero ($\bar{U}_b \approx 0$). Substituting $U_{in} = -U_{out}$ and $\bar{U}_b = 0$ into Equation 2.11 implies that $C_{fi,0} = (r_o/r_i)^2\, C_{fo,0}$ for the given conditions.

When the friction coefficient is reduced at the inner cylinder wall due to the riblets, the averaged bulk fluid will start to co-rotate a little with the direction of the outer cylinder. Likewise, when the friction coefficient at the inner wall is increased, the core flow will

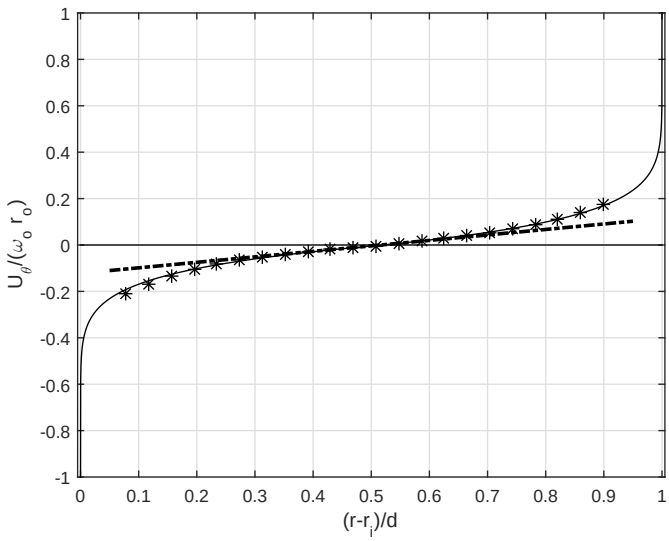

Figure 2.10: Averaged azimuthal velocity as a function of the radial position for shear Reynolds numbers $Re_s = 4.7 \times 10^4$. The velocities are normalized to the azimuthal velocity of the outer cylinder ($\omega_o r_o$). The solid line represents the velocity profile for turbulent boundary layers.

start to co-rotate a little with the inner cylinder. A similar phenomenon also occurs by operating two smooth cylinder walls with a rotation number $R_\Omega \neq 0$. The sign of the rotation number indicates the net system rotation; a negative or positive rotation number is associated with core flow rotation with the direction of the inner or outer cylinder rotation respectively. Hence, a reduced shear stress under exact counter-rotation at the inner cylinder wall due to riblets will result in a positive apparent rotation number $\hat{R}_\Omega$ and *vice versa*.
Ravelet *et al.* [12] demonstrated strong dependency of the friction coefficient C_f to the rotation number R_Ω with the same experimental setup. The friction coefficient C_f has a linear decline around rotation number $R_\Omega = 0$ with increasing rotation numbers. In the case of riblets, the net system rotation is changed ($\hat{R}_\Omega \neq 0$) even though we are operating under exact counter-rotating conditions ($R_\Omega = 0$). Except from a riblet drag change, this net system rotation also imposes a change in the friction coefficient.

We propose a simple model to distinguish drag changes due to the rotation effect and the riblet effect by measuring a change in torque on the inner cylinder wall. We consider the change in friction coefficient of the outer cylinder wall (C_{fo}) to be negligible for any Reynolds number Re_s, and therefore $C_{fo} = C_{fo,0}$. The averaged bulk velocity is normalized with the azimuthal velocity of the outer cylinder U_{out}, resulting in $\delta = \bar{U}_b / U_{out}$.

Equation 2.11 is rewritten as:

$$\begin{aligned} \tau_{w,rib} &= \frac{1}{2}\rho\, C_{fi,rib}\, U_{out}^2\, (-1-\delta)^2 \\ &= \frac{1}{2}\rho\, C_{fo}\, U_{out}^2\, (1-\delta)^2 \left(\frac{r_o}{r_i}\right)^2 \end{aligned} \tag{2.12}$$

Rearranging Equation 2.12 results in:

$$C_{fi,rib}\,(1+\delta)^2 = \left(\frac{r_o}{r_i}\right)^2 C_{fo}\,(1-\delta)^2 \tag{2.13}$$

The comparison between a riblet and smooth inner cylinder surface can be made, with $C_{fi,0} = (r_o/r_i)^2\, C_{fo,0} = (r_o/r_i)^2\, C_{fo}$:

$$\frac{\tau_{w,rib}}{\tau_{w,0}} \sim \frac{C_{fi,rib}}{C_{fi,0}} = \frac{C_{fi,rib}}{(r_o/r_i)^2\, C_{fo}} = \frac{(1-\delta)^2}{(1+\delta)^2} \tag{2.14}$$

Thus, the change in averaged bulk velocity due to the change of shear stress at the inner cylinder wall is determined by:

$$\delta = \frac{1-\sqrt{\tau_{w,rib}/\tau_{w,0}}}{1+\sqrt{\tau_{w,rib}/\tau_{w,0}}} \tag{2.15}$$

According to Equation 2.15, the maximum drag reduction of 5.3% observed around Reynolds number $Re_s = 4.7 \times 10^4$ will correspond with a change in averaged bulk velocity $\delta = 0.014$. PIV measurements confirm a similar shift of the averaged bulk velocity when a riblet inner cylinder is used (Fig. 2.11). The velocity gradient at the inner cylinder wall decreases significantly by using a riblet inner cylinder, which is associated with a lower level of turbulence. The gradient at the outer cylinder wall remains unaltered.

The rotation number R_Ω of Equation 2.2 is equal to:

$$R_\Omega = (1-\eta)\frac{U_i + U_o}{\eta U_o - U_i} \tag{2.16}$$

A small shift in the averaged bulk velocity under exact counter-rotating conditions ($R_\Omega = 0$) quantifies the apparent rotation number $\hat{R}_\Omega$:

$$\hat{R}_\Omega \simeq (1-\eta)\frac{(U_i + \bar{U}_b) + (U_o + \bar{U}_b)}{\eta(U_o + \bar{U}_b) - (U_i + \bar{U}_b)} \tag{2.17}$$

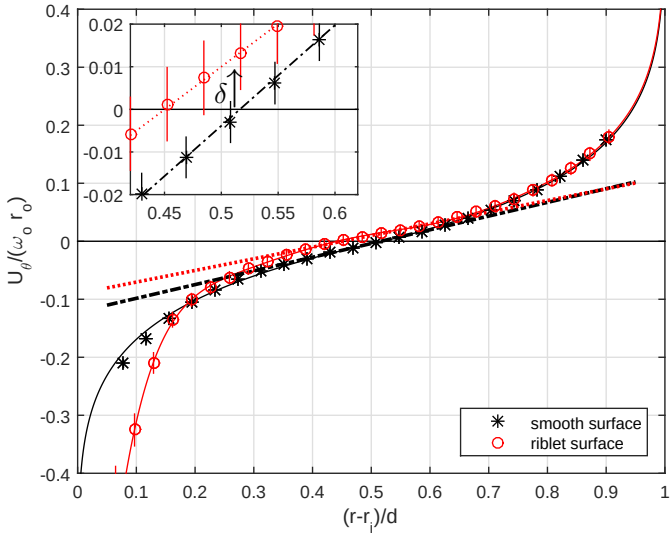

Figure 2.11: Azimuthal velocity profiles of a smooth and riblet inner cylinder at Reynolds number $Re_s = 4.7 \times 10^4$ under exact counter-rotating conditions ($R_\Omega = 0$). The velocities are normalized to the azimuthal velocity of the outer cylinder ($\omega_o r_o$). Errorbars represent the estimated 95% confidence interval. The solid lines represent the velocity profile for turbulent boundary layers for each case. The dashed lines indicates the azimuthal core flow velocities, for smooth surface (black $-\cdot-$) with slope $\alpha \approx 0.25$ and for riblet surface (red $\cdots$) with slope $\alpha \approx 0.20$. Inset: Zero-crossing of the azimuthal velocity profiles.

Equation 2.17 is rewritten as:

$$\hat{R}_\Omega \simeq (1-\eta)\frac{(-1+\delta)+(1+\delta)}{\eta(1+\delta)-(-1+\delta)} \tag{2.18}$$

A drag reduction of 5.3% with an averaged bulk velocity change of $\delta = 0.014$ results in an apparent rotation number $\hat{R}_\Omega = 0.0012$. The relation between the bulk velocity shift δ and the apparent rotation number $\hat{R}_\Omega$ was verified and is discussed in Appendix A.3. The apparent rotation number $\hat{R}_\Omega$ is very small but sufficient to play a substantial role in the total measured drag change. The relative rotational drag change is the difference between friction coefficients $C_f(R_\Omega = 0)$ and $C_f(\hat{R}_\Omega)$ with respect to $C_f(R_\Omega = 0)$. The slope dC_f/dR_Ω around $R_\Omega = 0$ defines the magnitude of rotational drag change, and is specific for each Reynolds number Re_s.

Accurate torque measurements were performed at various rotation numbers R_Ω for Reynolds numbers $Re_s = 4\times10^3$ to 10×10^4. Figure 2.12a shows the friction coefficients at a shear Reynolds number $Re_s = 2.0\times10^4$ for rotation numbers $-2.5\times10^{-3} < R_\Omega < 2.5\times10^{-3}$. The slope values dC_f/dR_Ω as a function of Reynolds number Re_s are displayed in Figure 2.12b. The relative rotational drag change $(\Delta\tau_\theta/\tau_{w,0})$ due to the rotation effect for a specific Reynolds number Re_s is defined by:

$$\frac{\Delta\tau_\theta}{\tau_{w,0}} = \frac{dC_f/dR_\Omega \cdot \hat{R}_\Omega}{C_{f,0}} \tag{2.19}$$

The net drag reduction of riblets is determined by the measured drag change plus the drag change due to the rotation effect. For Reynolds number $Re_s = 4.7\times10^4$ we measured a drag reduction of 5.3% and found positive rotation of the averaged bulk fluid with an apparent rotation number of $\hat{R}_\Omega = 0.0012$. Multiplying the slope value dC_f/dR_Ω at $Re_s = 4.7\times10^4$ with the apparent rotation number $\hat{R}_\Omega$ gives a drag change due to the rotation effect of -1.9%. Consequently, the maximum net riblet drag reduction $(\Delta\tau/\tau_0)_{max}$ is determined to be 3.4%. The model is applied to all measured drag values in order to determine the actual net drag change by the riblet surface. The results are presented in Figure 2.13.

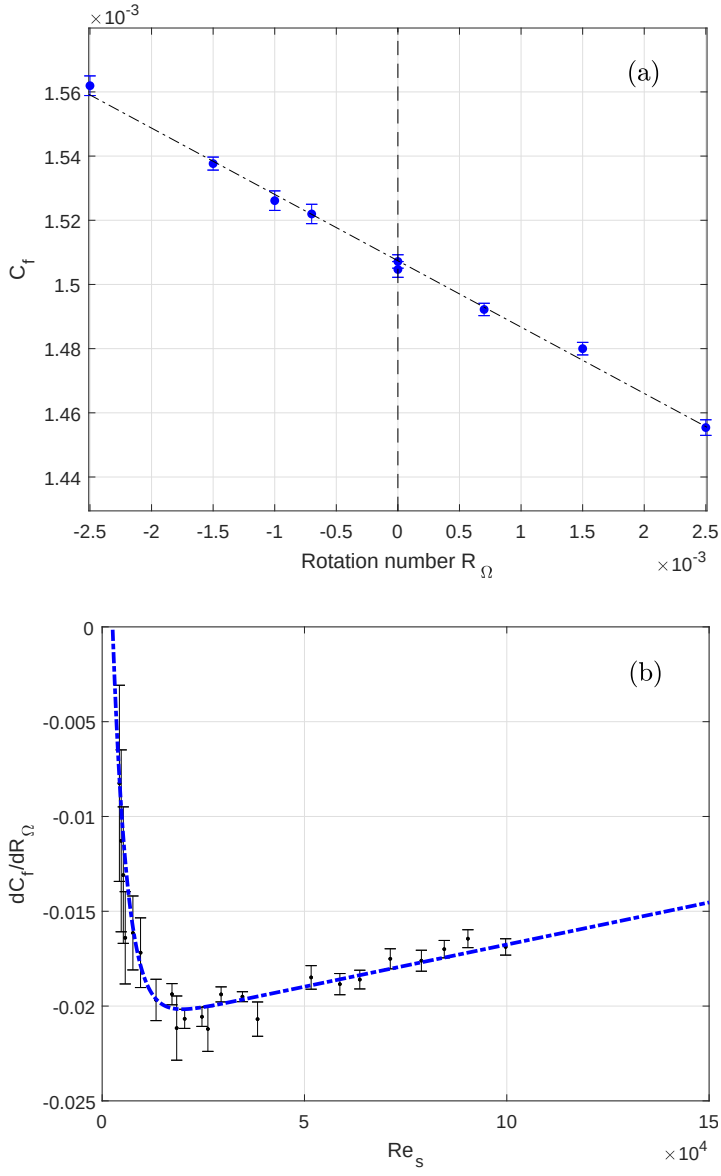

Figure 2.12: (a) Friction coefficient C_f as a function of the rotation number R_Ω at a shear Reynolds number $Re_s = 2.0 \times 10^4$. The dashed line is the best linear fit of the data points with slope $dC_f/dR_\Omega = (-20.7 \pm 0.5) \times 10^{-3}$. Errorbars: 95% confidence interval. The data at rotation number $R_\Omega = 0$ is reproducible within 0.17%, (b) Slope values dC_f/dR_Ω as a function of Reynolds number Re_s around rotation number $R_\Omega = 0$. The dashed line is a least-squares-fit of the data.

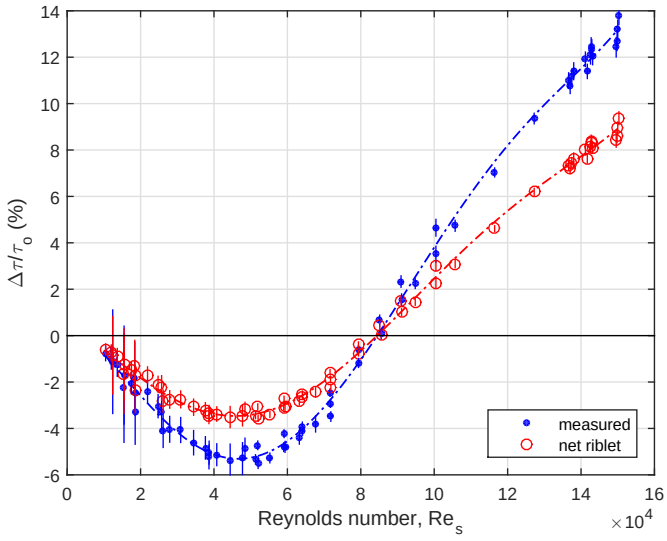

Figure 2.13: Measured and net drag change by riblet inner cylinder under exact counter-rotation ($R_\Omega = 0$). The dashed lines are polynomial fits of the obtained results between $Re_s = 1.0 \times 10^4$ to 15×10^4.

2.5.2. DATA VALIDATION

The data is compared to other available data of drag reduction research with similar riblets (Bechert *et al.* [21], Hall and Joseph [4]), while keeping in mind that riblet performance can be sensitive to experimental geometry, measurement accuracy and riblet surface quality. Figure 2.14 presents the obtained net drag change $\Delta\tau/\tau_0$ as a function of the riblet spacing Reynolds number s^+ measured with the current experimental facility and is limited to $s^+ > 3.5$ ($\sim Re_s > 10^4$).

The overall trend of the curve is comparable with earlier reported results; a maximum drag reduction between riblet spacing $s^+ = 11-16$ and a zero drag reduction cross-over point between $s^+ = 21-27$. Higher riblet spacing s^+ is associated with wall roughness compared to the high skin friction and the riblets exceeds their drag reducing benefits. Hall and Joseph [4] performed similar drag measurements with riblets on the inner cylinder surface with only outer cylinder rotation ($Re_i = 0$) and reported a maximum drag reduction of 5.1%. Their flow is driven by the outer cylinder while the shear stress is measured on the inner cylinder. No comments are made for global rotation or possible rotation effects, while both phenomena will influence the turbulent structures and velocity fields and consequently manipulate the drag performance of surfaces when compared to boundary layer or fluid channel experiments. Secondly and possibly more important, they observed high frequency vibrations of the inner cylinder during measurements in the range of $s^+ = 7-20$ ($Re_s = 1 \times 10^4$ to 3×10^4). They reported that their flow is presumably in the midst of a flow transition, which makes direct comparison of the results difficult.
Bechert *et al.* [21] performed their riblet measurements in the Berlin oil channel facil-

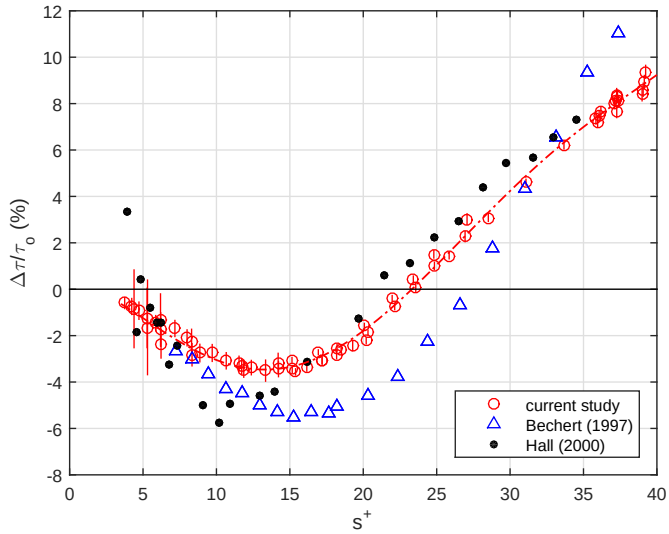

Figure 2.14: Net riblet drag change $\Delta\tau/\tau_0$ as a function of the riblet spacing s^+. Compared to drag results obtained in an oil channel [21] and an outer-cylinder rotating Taylor-Couette [4].

ity with a very accurate shear-stress balance. Their curve looks equivalent to ours, but their observed maximum drag reduction is around 5.5% at $s^+ = 16$. The zero drag reduction cross-over point is at a higher s^+-value of $s^+ = 27$, resulting in a wide range of drag reduction. After the cross-over point the curve has a steeper slope compared to the slope of the current study. The noticeable round/flat area of the riblet tips (Fig. 2.3) can conceivably be a reason for the deviation in drag results, as the tip sharpness is a crucial factor for the drag reducing performance of any riblet geometry [21].

2.6. CONCLUSION

Previous studies have demonstrated that a small amount of drag reduction is achievable by riblets, but requires high accuracy of the experimental setup. The changes in drag can often be within the scatter of the measurements. In our study, the friction coefficients are reproducible within 0.6% for all working fluids and are more accurate at higher shear Reynolds numbers Re_s, where the torque meter is more precise with relatively less noise. We verified the presence of different flow regimes by PIV measurements and concluded that the friction coefficients and the drag performance of riblets are strongly determined by the flow regimes. In the Taylor-vortex flow regime, the riblets induce extra drag compared to a smooth surface, which is considered to be an artefact of the experimental setup rather than a drag characteristic of riblets. Therefore, the derived riblet data is limited to $Re_s > 10^4$ for the comparison to the data obtained by other researchers, as the low Reynolds number flow characteristics in a TC facility differs significantly from typical turbulent channel and pipe flows. For fully turbulent

flow, the measured torque can be reduced by 5.3% by applying riblets.
PIV measurements at Reynolds number $Re_s = 4.7 \times 10^4$ show a change in the azimuthal velocity profile by applying riblets on the inner cylinder surface. The velocity gradient at the inner cylinder wall decreases significantly, which is associated with a lower level of turbulence.
A rotation effect occurs by the drag changes under exact counter-rotating conditions. The proposed model indicates the change in mean azimuthal bulk flow velocity. The maximum observed drag reduction of 5.3% at the inner cylinder wall implies a change of 1.4% in the mean azimuthal bulk velocity, which is also verified by PIV measurements. By taking the rotation effect into account, we obtain a proper method to rectify the net drag change by riblets, which reasonably fits earlier reported data.
The Taylor-Couette facility has shown to be a suitable facility for accurate torque measurements to characterize the drag performance of surfaces.

REFERENCES

[1] A. J. Greidanus, R. Delfos, S. Tokgoz, and J. Westerweel, *Turbulent Taylor-Couette flow over riblets: drag reduction and the effect of bulk fluid rotation,* Experiments in Fluids **56**, 1 (2015).

[2] D. M. Bushnell, *Viscous drag reduction in boundary layers*, Vol. 123 (AIAA, 1990).

[3] V. Kalashnikov, *Dynamical similarity and dimensionless relations for turbulent drag reduction by polymer additives,* Journal of non-newtonian fluid mechanics **75**, 209 (1998).

[4] T. Hall and D. Joseph, *Rotating cylinder drag balance with application to riblets,* Experiments in fluids **29**, 215 (2000).

[5] K. Koeltzsch, Y. Qi, R. Brodkey, and J. Zakin, *Drag reduction using surfactants in a rotating cylinder geometry,* Experiments in fluids **34**, 515 (2003).

[6] K. Watanabe, T. Takayama, S. Ogata, and S. Isozaki, *Flow between two coaxial rotating cylinders with a highly water-repellent wall,* AIChE journal **49**, 1956 (2003).

[7] T. H. van den Berg, S. Luther, D. P. Lathrop, and D. Lohse, *Drag reduction in bubbly Taylor-Couette turbulence,* Physical review letters **94**, 044501 (2005).

[8] C. D. Andereck, S. Liu, and H. L. Swinney, *Flow regimes in a circular Couette system with independently rotating cylinders,* Journal of Fluid Mechanics **164**, 155 (1986).

[9] D. P. Lathrop, J. Fineberg, and H. L. Swinney, *Transition to shear-driven turbulence in Couette-Taylor flow,* Physical Review A **46**, 6390 (1992).

[10] G. S. Lewis and H. L. Swinney, *Velocity structure functions, scaling, and transitions in high-Reynolds-number Couette-Taylor flow,* Physical Review E **59**, 5457 (1999).

[11] B. Eckhardt, S. Grossmann, and D. Lohse, *Torque scaling in turbulent Taylor-Couette flow between independently rotating cylinders,* Journal of Fluid Mechanics **581**, 221 (2007).

[12] F. Ravelet, R. Delfos, and J. Westerweel, *Influence of global rotation and Reynolds number on the large-scale features of a turbulent Taylor-Couette flow,* Physics of Fluids (1994-present) **22**, 055103 (2010).

[13] S. Tokgöz, *Coherent Structures in Taylor-Couette Flow: Experimental Investigation*, Ph.D. thesis, TU Delft, Delft University of Technology (2014).

[14] R. Delfos, F. Ravelet, and J. Westerweel, *Scaling of torque in turbulent taylor-couette flow with background rotation,* in *Advances in Turbulence XII* (Springer, 2009) pp. 629–632.

[15] J. W. Daily and R. E. Nece, *Chamber dimension effects on induced flow and frictional resistance of enclosed rotating disks,* Journal of Fluids Engineering **82**, 217 (1960).

[16] A. Hudson and P. Eibeck, *Torque measurements of corotating disks in an axisymmetric enclosure,* Journal of fluids engineering **113**, 648 (1991).

[17] M. Kilic and J. M. Owen, *Computation of flow between two discs rotating at different speeds,* in *ASME Turbo Expo 2002: Power for Land, Sea, and Air* (American Society of Mechanical Engineers, 2002) pp. 749–759.

[18] G. E. Elsinga, F. Scarano, B. Wieneke, and B. Van Oudheusden, *Tomographic particle image velocimetry,* Experiments in Fluids **41**, 933 (2006).

[19] S. Tokgoz, G. E. Elsinga, R. Delfos, and J. Westerweel, *Spatial resolution and dissipation rate estimation in taylor–couette flow for tomographic piv,* Experiments in fluids **53**, 561 (2012).

[20] J. Westerweel and F. Scarano, *Universal outlier detection for piv data,* Experiments in fluids **39**, 1096 (2005).

[21] D. Bechert, M. Bruse, W. Hage, J. T. Van der Hoeven, and G. Hoppe, *Experiments on drag-reducing surfaces and their optimization with an adjustable geometry,* Journal of Fluid Mechanics **338**, 59 (1997).

[22] J. van der Hoeven, *Observations in the turbulent boundary-layer-high resolution DPIV measurements over smooth and riblet surfaces,* Ph.D. thesis, TU Delft, Delft University of Technology (2000).

[23] B. Dubrulle, O. Dauchot, F. Daviaud, P.-Y. Longaretti, D. Richard, and J.-P. Zahn, *Stability and turbulent transport in Taylor-Couette flow from analysis of experimental data,* Physics of Fluids (1994-present) **17**, 095103 (2005).

[24] G. I. Taylor, *Stability of a viscous liquid contained between two rotating cylinders,* Philosophical Transactions of the Royal Society of London. Series A, Containing Papers of a Mathematical or Physical Character , 289 (1923).

[25] A. Esser and S. Grossmann, *Analytic expression for Taylor-Couette stability boundary,* Physics of Fluids (1994-present) **8**, 1814 (1996).

[26] S. Dong, *Turbulent flow between counter-rotating concentric cylinders: a direct numerical simulation study,* Journal of Fluid Mechanics **615**, 371 (2008).

[27] L. Van Bokhoven, H. Clercx, G. Van Heijst, and R. Trieling, *Experiments on rapidly rotating turbulent flows,* Physics of Fluids (1994-present) **21**, 096601 (2009).

[28] E. Aydin and H. Leutheusser, *Plane-couette flow between smooth and rough walls,* Experiments in fluids **11**, 302 (1991).

3

SCALING AND RIBLET DRAG PERFORMANCE UNDER PERIODIC TURBULENT CONDITIONS

3.1. INTRODUCTION

Typical research on turbulent flows often engage steady flows with a reasonably constant bulk velocity in time. However, pulsating flows are unsteady due to an oscillating velocity superimposed on a steady velocity and deliver interesting and complex fluid dynamics to investigate. The flow behaviour depends on a time-averaged velocity, a velocity amplitude and an oscillation period. The periodicity results in temporal change of fluid motions and modifies the flow conditions and statistics.

An extensive amount of experimental investigations have been carried out to understand the fundamentals of pulsating pipe flows, see e.g. the reviews by Çarpinlioglu and Gündogdu [1] or Nabavi and Siddiqui [2]. Many studies on pulsatile flow focus on industrial and bio-fluids processes that deal with periodic fluid transport and their associated flow effects, such as fluid mixing [3], enhanced heat transfer [4, 5], surface cleaning [6], artery blood flows [7, 8], and many more. However, research on turbulent drag reduction under periodic flow conditions are very uncommon. Drag reduction is often investigated for steady flow conditions, but in practical applications the flow would not always be steady. The question is whether drag reduction is maintained under unsteady flow conditions and to understand the reciprocal relation between drag reducing solutions and unsteady turbulent flows. For example, an exciting field of interest is rowing, where a boat experiences velocity variations during one rowing cycle (Figure 3.1). Prior to the regulation assessment, discussion is needed to what extent such performance enhancements in competitive sports are still acceptable in the domain of fair play.

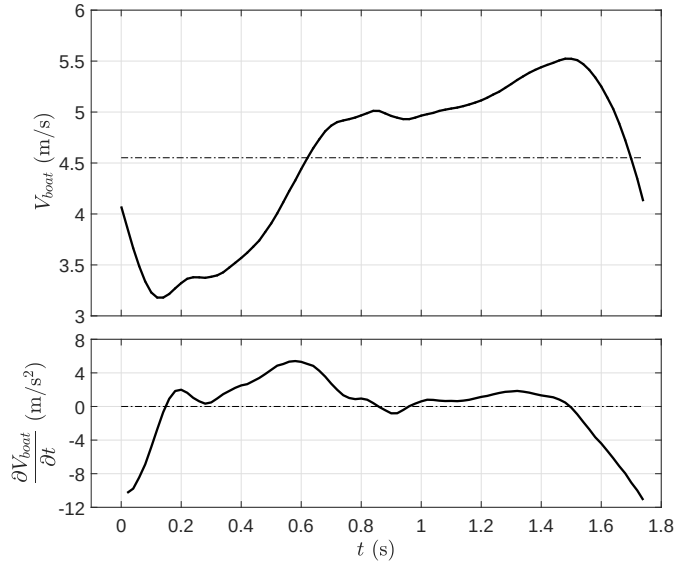

Figure 3.1: Boat velocity V_{boat} (top) and estimated boat acceleration $\partial V_{boat}/\partial t$ (bottom) during one rowing cycle, with $\langle V_{boat} \rangle$ = 4.55 m/s and stroke rate 34.5 min^{-1} (i.e. T =1.74 s). Field data obtained from an international lightweight single sculler. The velocity variations are due to (1) non-continuous propulsion and (2) induced boat acceleration in opposite direction of the rower mass displacement.

In this study, a Taylor-Couette (TC) system has been applied to investigate the frictional drag of a periodic driven turbulent flow. The fluid is set in motion in a closed geometry between two rotating cylinders, which are considered to be moving boundary conditions. Under pulsatile boundary conditions, the fluid motions are related to the velocity amplitude and oscillation period of the pulsatile rotating cylinders. As the generated shear stress on the cylinders is connected to the fluid motions, a relation between the frictional drag and these two driving parameters is expected.
Previously, it was demonstrated that the TC-facility is an accurate, easy-to-use, and compact test-facility to measure the frictional resistance of surfaces under steady turbulent flow conditions [9]. This time, additional measurements are undertaken to analyze the drag reducing ability of a riblet surface under periodic turbulent flow conditions.
The outline of this chapter starts with the experimental setup and conditions in Section 3.2. In Section 3.3, the difference in frictional drag between steady and unsteady flow related to the two driving parameters (i.e. velocity amplitude and oscillation period) is described and explained, as well as the riblet drag performance under periodic flow conditions. Finally, the conclusions are summarized in Section 3.4.

3.2. EXPERIMENTAL SETUP & CONDITIONS

3.2.1. TAYLOR-COUETTE FACILITY

A Taylor-Couette facility is applied for the current investigation, as shown in the schematic illustration in Figure 3.2. The setup consists of two co-axial acrylic glass cylinders that both can rotate independently. The inner cylinder radius is $r_i = 110$ mm and total length is $L_i = 216.7$ mm. The outer cylinder has a radius $r_o = 120$ mm and a length $L_o = 222.1$ mm. Note that the subscripts i are assigned for the inner cylinder and o for

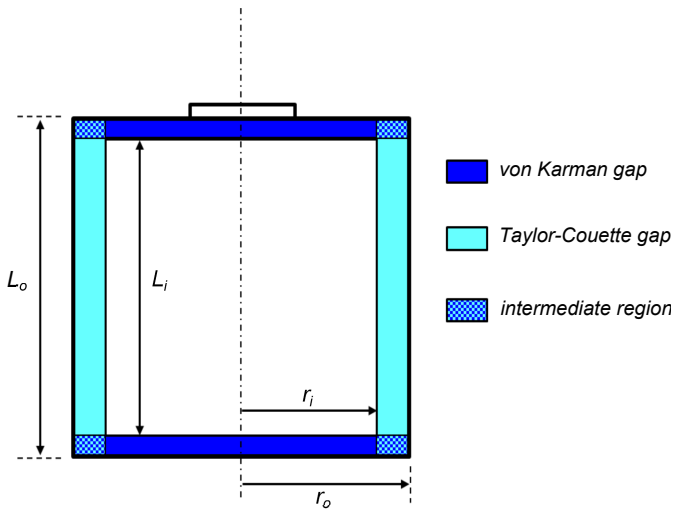

Figure 3.2: Schematic interpretation of the Taylor-Couette facility.

the outer cylinder. The radial gap between the cylinders is $d = r_o - r_i = 10.0$ mm, the so-called *Taylor-Couette* gap. The gap ratio is $\eta = r_i/r_o = 0.917$. The gaps between the top and bottom end-plates of the inner and outer cylinder are around $h = 2.5-3.0$ mm and are called the *von Kármán* gaps, named after the classical von Kármán swirling flow [10]. The TC-system was filled with tap water as the working fluid.% (T_f =19.5 ± 0.2 ^{o}C).

The fluid motions between the rotating cylinders generated a shear stress on the surfaces that was recorded with a co-rotating torque meter (HBM T20WN/2Nm, abs. precision ±0.01 Nm) that is assembled in the shaft between the driving motor (Maxon, 250W) and inner cylinder. The outer cylinder is driven by an identical external motor via a driving belt. Experiment control and data acquisition is program-executed. The total torque M_{tot} and rotation rate ω_i of the inner cylinder are recorded at a sampling rate of 2 kHz.

3.2.2. EXPERIMENTAL CONSIDERATIONS

The flow between the two concentric cylinders is driven by the rotation of the inner and/or outer cylinder. The current experiments were performed under exact counter-rotation conditions, which represents identical rotation velocity of the two cylinders in opposite direction, such that $U_i = -U_o$. The rotation velocity of the inner cylinder is defined by $U_i = \omega_i r_i$, with ω_i as the inner cylinder angular frequency. For exact counter-rotation conditions, the outer cylinder angular frequency is given by $\omega_o = -\omega_i r_i/r_o$. The shear velocity between the two rotating cylinders equals $U_{sh} = \omega_i r_i - \omega_o r_o = |2\omega_i r_i|$. Under steady flow conditions, a fully developed flow is very similar to a planar Couette flow with the exception of the presence of curvature effects and centrifugal forces. During the oscillation experiments, the velocity was modulated as a sinusoidal function, such that the velocity of the inner cylinder is $U_i = \langle U_i \rangle - \Delta U_i \sin(2\pi t/T)$ and the outer cylinder velocity is $U_o = \langle U_o \rangle + \Delta U_o \sin(2\pi t/T)$, see Figure 3.3a. Consequently, the shear velocity between the two rotating cylinders becomes

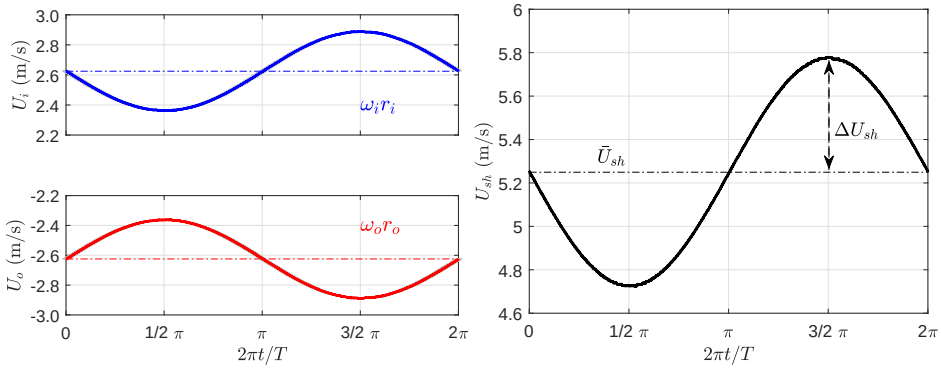

Figure 3.3: Example of velocity progression during one period of periodic driven cylinders, with an amplitude $\Delta U_o/U_o = \Delta U_i/U_i = 0.10$. a) Inner (positive) and outer (negative) rotation velocity, $U_i = \omega_i r_i$ and $U_o = \omega_o r_o$. b) Relative shear velocity between two cylinders, with $U_{sh} = U_i - U_o = 2|U_i|$.

$U_{sh} = \langle U_{sh} \rangle - \Delta U_{sh} \sin(2\pi t/T)$, where $\langle U_{sh} \rangle$ is the mean shear velocity, ΔU_{sh} the oscillation amplitude (= $\Delta U_i + \Delta U_o$) and T the oscillation period (Fig. 3.3b). The *relative* oscillation amplitude is given by $\mathscr{A} = \Delta U_{sh} / \langle U_{sh} \rangle$, such that the normalized shear velocity becomes $U_{sh} / \langle U_{sh} \rangle = 1 - \mathscr{A} \sin(2\pi t/T)$.
In this study, the measured torque M_{tot} of the inner cylinder is converted into the power P_{tot} needed to rotate the cylinder (i.e. $P \equiv M\omega_i$). Under periodically driven conditions, the rotational inertia of the cylinder contributes significantly to the power P_{tot}, as an additional amount of power (P_{inrt}) is needed to accelerate and decelerate the total mass of the inner cylinder:

$$P_{inrt} = \left(\frac{\partial \omega_i}{\partial t} \cdot I_{inrt} \right) \omega_i \tag{3.1}$$

$$\text{with} \quad \frac{\partial \omega_i}{\partial t} = -\frac{\pi}{T} \frac{\Delta U_{sh}}{r_i} \cdot \cos(2\pi t/T) \qquad \text{and} \qquad I_{inrt} = \tfrac{1}{2} \cdot \sum m_j (r_j^2 + R_j^2)$$

In Equation 3.1, $\frac{\partial \omega_i}{\partial t}$ is the angular acceleration and I_{inrt} the moment of inertia, with m_j the individual mass of the cylinder components (j = axis, end plates, cylinder shell), while r_j and R_j are the inner and outer radius of component j, respectively. In Figure 3.4, the estimated phase-averaged power corresponding to rotational inertia, which is measured with an empty TC-facility (i.e. no water, but air), corresponds very well with the analytical approximation (Eq. 3.1). Small differences are addressed to internal power losses of the system (e.g. coupling flexibility). Straightforward, the instantaneous power P_d to overcome the hydrodynamic drag is considered to be equal to $P_d = P_{tot} - P_{inrt}$, and is also shown in Figure 3.4.

The region of the *von Kármán* gaps and the *Taylor-Couette* gap (Fig. 3.2) have each their own characteristic fluid motions, both contributing to the turbulent shear stress acting on the inner cylinder. In the current study, the torque contributions of the TC-gap M_{tc} under dynamic exact counter-rotation conditions is assumed to be similar as under steady conditions, which is around $70-75\%$ of the total hydrodynamic drag M_d [9] and equals $P_{d,tc} = 0.70 - 0.75 P_d$. The time-averaged drag power of the Taylor-Couette gap $\langle P_{d,tc} \rangle$ is defined by the inner wall shear stress τ_w and angular frequency of the inner cylinder ω_i:

$$\langle P_{d,tc} \rangle = \langle \omega_i M_{tc} \rangle = 2\pi r_i^2 L_i \langle \omega_i \tau_w \rangle \tag{3.2}$$

As the geometric parameters r_i and L_i are constants, the time-averaged drag power $\langle P_{d,tc} \rangle$ scales with $\langle \omega_i \tau_w \rangle$ and quantifies the turbulent drag change when operating under periodically driven boundary conditions in contrast to steady boundary conditions.

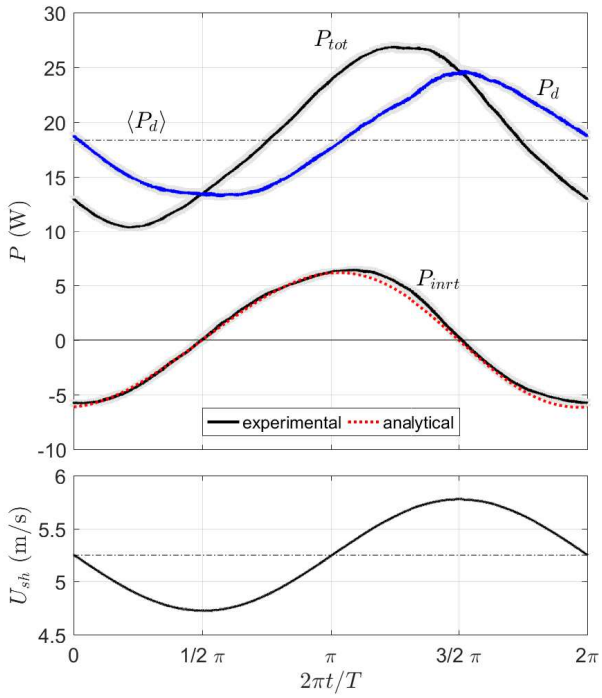

Figure 3.4: a) The measured phase-averaged inertia power P_{inrt} with an empty TC-system (black, solid line) and the analytical approximation (red, dotted line). b) The measured phase-averaged power P_{tot} and reconstructed power due to hydrodynamic drag P_d. The operational conditions are $\langle U_{sh} \rangle$ = 5.2 m/s, ΔU_{sh} = 0.52 m/s and T = 3 s. The shaded area represents the 95% confidence interval.

SCALING PARAMETERS

Under steady conditions, the shear velocity is maintained constant over time $U_{sh} = \langle U_{sh} \rangle$ and prescribes the shear Reynolds number Re_s that indicates the ratio between inertial forces to viscous forces (Eq. 3.3). As discussed by Greidanus *et al.* [9], under steady conditions the turbulent friction coefficient C_f scales with $C_f \sim Re_s^{-1/4}$ in the typical range of Re_s and while $\tau_w = 1/2 C_f \rho U_{sh}^2$, the drag power scales with $\langle P_{d,tc} \rangle \sim U_{sh}^{11/4}$. However, pulsatile boundary conditions induce acceleration (or deceleration) of the fluid and manipulate the fluid motions in the boundary layer. Therefore, a second and a third dimensionless parameter are introduced; the oscillatory Reynolds number Re_{osc} and the Womersley number Wo. The oscillatory Reynolds number $Re_{osc} = \mathscr{A} Re_s$ represents the additional inertial forces due to the oscillating velocity amplitude ΔU_{sh} (Eq. 3.4), while the Womersley number Wo denotes the transient inertial force in relation to the viscous forces (Eq. 3.5). When the Womersley number is very low ($T \to \infty$), the oscillating flow is considered to be quasi-stationary, such that the acceleration and deceleration of the flow has marginal influence on the fluid behaviour and the scal-

ing remains $\langle P_{d,tc}\rangle \sim \frac{1}{T}\int_0^T U_{sh}^{11/4} dt$. When the Womersley number Wo increases, the acceleration/deceleration is playing a significant role and changes the shape of the boundary layer profile. The fluid is not capable to respond in time to the transient forces caused by the pulsatile boundary conditions, which results in a phase lag between the oscillation input and fluid response, which was also reported by Trip *et al.* [11], Verschoof *et al.* [12]. Under these conditions, the general scaling becomes invalid, $\langle P_{d,tc}\rangle \nsim \frac{1}{T}\int_0^T U_{sh}^{11/4} dt$. Overall, the drag power $\langle P_{d,tc}\rangle$ is related to the three main dimensionless parameters, i.e. $\langle P_{d,tc}\rangle = f(Re_s, Re_{osc}, Wo)$.

$$Re_s = \frac{\langle U_{sh}\rangle d}{\nu} \tag{3.3}$$

$$Re_{osc} = \frac{\Delta U_{sh} d}{\nu} = \mathscr{A} Re_s \tag{3.4}$$

$$Wo = \sqrt{\frac{2\pi}{\nu T}} d \tag{3.5}$$

EXPERIMENTAL OUTLINE

The first part discusses the change in turbulent frictional drag compared to steady boundary conditions, as the periodic acceleration/deceleration influence the fluid motions in the boundary layer. The utilized time-averaged shear velocity is $\langle U_{sh}\rangle = 5.2$ m/s, corresponding to a shear Reynolds number $Re_s = 5.7 \times 10^4$. The oscillation velocity amplitude has a range of $\mathscr{A} = 0 - 0.40$, yielding the oscillatory Reynolds numbers $Re_{osc} = 0 - 2.3 \times 10^4$, such that the flow is considered to be turbulent under all conditions. The oscillation period was varied from $T = 2.0 - 23$ s, resulting in a Womersley number from Wo =18.7 down to 5.5. An additional oscillation period $T = 600$ s ($\simeq Wo \equiv 1$) was included to verify the quasi-stationary analogy, i.e. $\langle P_{d,tc}\rangle \sim \frac{1}{T}\int_0^T U_{sh}^{11/4} dt$. These experimental conditions result to the scaling behaviour of a Taylor-Couette flow as a function of periodic driven boundaries under exact counter-rotating conditions.
Second, the riblet performance to reduce frictional drag under periodic driven boundary conditions has been evaluated. A shear Reynolds number $Re_s = 5.2 \times 10^4$ and oscillatory Reynolds numbers $Re_{osc} = 0 - 1.8 \times 10^4$ were adopted with constant oscillation period $T = 3.0$ s ($\simeq Wo \equiv 14.5$). The applied riblet surface had a triangular cross-section geometry with riblet spacing $s = 120$ μm and height h =110 μm. The orientation of the riblet grooves was in the azumithal direction of the rotating cylinder. The riblets were applied to the inner *and* outer cylinder surface to exclude a possible rotation effect of the flow, as it is discussed by Greidanus *et al.* [9], see Chapter 2. For all experiments, 20 or more consecutive oscillation periods were recorded to obtain a reliable convergence of the phase-averaged torque $\langle M_{tot}\rangle$.

3.3. RESULTS & DISCUSSION

Under periodic flow conditions, the turbulent intensity increases due to the growth of the velocity fluctuations (u', v'). The additional drag power $\Delta\langle P_{d,tc}\rangle$ relative to steady boundary conditions with an identical shear Reynolds number Re_s is equivalent to:

$$\Delta\langle P_{d,tc}\rangle = \langle P_{d,tc}\rangle_{Re_s,Re_{osc},Wo} - \langle P_{d,tc}\rangle_{Re_s,0,0} \tag{3.6}$$

The subscripts indicate the scaling parameters that represents the experimental conditions, such that $Re_{osc} = 0$ and $Wo = 0$ applies to steady boundary conditions. The time-averaged drag change DC for periodic driven turbulence in contrast to steady boundary conditions is quantified by:

$$DC = \frac{\langle P_{d,tc}\rangle_{Re_s,Re_{osc},Wo}}{\langle P_{d,tc}\rangle_{Re_s,0,0}} - 1 \tag{3.7}$$

The influence of the oscillatory Reynolds number Re_{osc} and Womersley number Wo on the turbulent drag change will be discussed in the next paragraph.

3.3.1. THE EFFECT OF OSCILLATION AMPLITUDE AND PERIOD TIME

Figure 3.5 displays the relation between the measured change of turbulent drag DC, while maintaining a constant oscillation period $T = 3.0$ s (i.e. $Wo = 15.4$). No significant impact is observed on the drag change for small oscillation velocity amplitudes, i.e. $Re_{osc}/Re_s \leq 0.05$. These small velocity amplitudes ($\Delta U_{sh} \leq 0.26$ m/s) are considered smaller than the general turbulent velocity fluctuations u' under identical steady boundary conditions, when assuming $u' \sim$ 2-3 u_τ with $u_\tau = \sqrt{\tau_{w,0}/\rho} \sim 0.13$ m/s. Additional to that, the period time scale T is very different compared to the turbulent Kolmogorov time scale τ_n ($T/\tau_n \sim \mathcal{O}(10^3 - 10^5)$). The small perturbations caused by the periodic driven modulations have negligible influence on the flow behaviour and statistics for small oscillation amplitudes ($Re_{osc}/Re_s \leq 0.05$). For large oscillation amplitudes $Re_{osc}/Re_s \geq 0.10$, the turbulent fluctuations and intensity increase and results in a noticeable drag change DC.

The influence of the oscillation period time T was investigated by varying the period time $T = 2 - 25$ s for multiple oscillation velocity amplitude Re_{osc}/Re_s. The results of three amplitudes $Re_{osc}/Re_s = 0.20$, 0.30 and 0.40 are presented in Figure 3.6 (graph), which shows the relative drag change as a function of the Womersley number Wo. For low Wo, the acceleration/deceleration of the fluid is marginal and the flow conditions are considered to be quasi-steady-state. An approximation of the quasi-steady-state condition is obtained by the measurements with period time $T = 600$ s (~10 min), which corresponds to a Womersley number $Wo = 1$. In Figure 3.6 (table), the values of the measured drag change under quasi-steady-state conditions corresponds very well

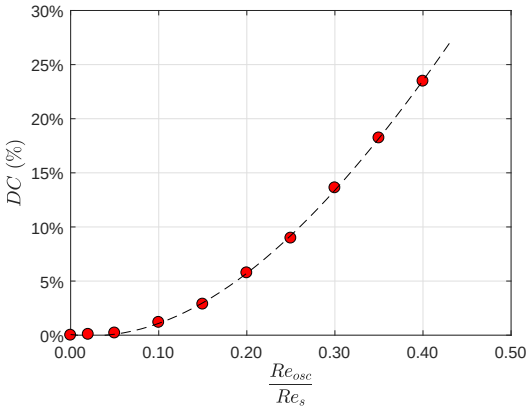

$\mathscr{A} = Re_{osc}/Re_s$	$\langle P_{d,tc} \rangle$ (W)	DC (%)
0.00	12.61	0.00
0.02	12.62	0.08
0.05	12.64	0.20
0.10	12.76	1.19
0.15	12.97	2.87
0.20	13.33	5.76
0.25	13.74	8.97
0.30	14.33	13.62
0.35	14.90	18.23
0.40	15.57	23.47

Figure 3.5: Drag change DC as a function of the relative velocity amplitude Re_{osc}/Re_s at $Re_s = 5.7 \times 10^4$ for an oscillation period $T = 3.0$ s ($Wo = 15.4$). The dashed line represents the second-order fit to the obtained results, such that $DC = f\left((Re_{osc}/Re_s)^2\right)$ at a constant Wo.

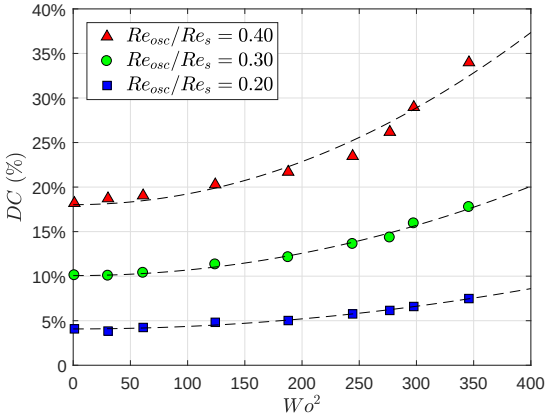

$\mathscr{A} = Re_{osc}/Re_s$	DC_0 (%) Exp.	DC_0 (%) Theory
0.00	0	0
0.02	0.01	0.05
0.05	0.13	0.30
0.10	0.87	1.20
0.15	2.00	2.71
0.20	4.08	4.81
0.25	6.80	7.51
0.30	10.10	10.82
0.35	13.90	14.72
0.40	18.19	19.21

Figure 3.6: Drag change DC as a function of Womersley number Wo^2 for different amplitudes $Re_{osc}/Re_s = 0.20$, 0.30 and 0.40 at $Re_s = 5.7 \times 10^4$. The dashed lines represent the second-order fit to the obtained results, such that $DC = f\left(\left(Wo^2\right)^2\right)$ at a constant Re_{osc}/Re_s. The table indicates the measured drag change values DC_0 for a very low Womersley numbers $Wo \simeq 1$ and the analytical DC_0 values ($Wo \rightarrow 0$) for the applied amplitude range $Re_{osc}/Re_s = 0$ - 0.40.

with the analytical/theoretical values obtained via $DC_0 \sim \frac{1}{T}\int_0^T (U_{sh}/\langle U_{sh}\rangle)^{11/4}\,dt = \frac{1}{2\pi}\int_0^{2\pi}(1+\mathscr{A}\sin(\alpha))^{11/4}\,d\alpha$. When the oscillation period T reduces (i.e. $Wo \uparrow$), the acceleration/deceleration of the fluid becomes more violent, while the turbulent eddies have not sufficient time to adapt to the changing situation and increases the frictional drag.

UNIVERSAL SCALING

The drag change DC is determined with varying Re_{osc} and Wo. The results are presented in Figure 3.7a as a function of the two scaling parameters. In order to explore similarity in the drag change response to the two driving parameters Re_{osc} and Wo, a second mean shear velocity $\langle U_{sh} \rangle = 2.6$ m/s ($Re_s = 2.9 \times 10^4$) was applied. The results, shown in Figure 3.7b, are similar and suggest that the drag change DC is independent of the mean shear velocity $\langle U_{sh} \rangle$. Nevertheless, the results at $\langle U_{sh} \rangle = 2.6$ m/s are considered to be less accurate as the quantified torque-values associated with the additional drag $\Delta \langle P_d \rangle$ are in the order of the absolute precision of the torquemeter (~ 0.01 Nm). Therefore, the scaling analogy was performed with the data obtained at the high mean shear velocity $\langle U_{sh} \rangle = 5.2$ m/s. The asymptotic lines in Figure 3.7 represents the ratio $\langle P_{d,tc} \rangle_{Re_s,0,0} / P_{inrt}^{max}$ and indicate the relative presence of inertia under the applied conditions.

The acceleration term of the periodic driven boundary conditions is defined by the oscillation velocity amplitude ΔU_{sh} and period T:

$$\frac{\partial U_{sh}}{\partial t} = 2\pi \frac{\Delta U_{sh}}{T} \cos(2\pi t / T) \tag{3.8}$$

The acceleration term is made dimensionless with $\langle U_{sh} \rangle$, ν, d^2 and delivers a non-dimensional relation defined by the Womersley number Wo, the oscillatory Reynolds number Re_{osc} and the shear Reynolds number Re_s, such that the maximum acceleration is quantified by $Wo^2 Re_{osc}/Re_s$:

$$\left(\frac{d^2}{\nu \langle U_{sh} \rangle} \right) \left| \frac{\partial U_{sh}}{\partial t} \right|_{max} = Wo^2 \frac{Re_{osc}}{Re_s} \tag{3.9}$$

When the acceleration becomes negligible, i.e. $Wo^2 Re_{osc}/Re_s \to 0$, the drag change DC equals the quasi-steady-state solution $DC_0 \sim \frac{1}{T} \int_0^T (U_{sh}/\langle U_{sh} \rangle)^{11/4} \, dt$. However, when the acceleration becomes more relevant (i.e. increase of $Wo^2 Re_{osc}/Re_s$), the drag response shows an identical trend for all the applied velocity amplitudes Re_{osc}/Re_s (Fig. 3.8a). The drag change DC scales linearly with the squared acceleration $\left(Wo^2 Re_{osc}/Re_s\right)^2$. Consequently, the results show an adequate overlap when the quasi-steady-state values DC_0 are subtracted from the drag change values DC of each particular velocity amplitude Re_{osc}/Re_s, as demonstrated in Figure 3.8b. This resembles that the summation of the two elementary components gives an universal relation of the drag change DC as a function of periodic driven boundary conditions relative to steady boundary conditions for exact counter-rotating cylinders:

$$DC = \frac{1}{2\pi} \int_0^{2\pi} (1 + \mathscr{A} \sin(\alpha))^{11/4} \, d\alpha + \mathscr{K}^* \cdot \left(Wo^2 \frac{Re_{osc}}{Re_s} \right)^2 - 1 \tag{3.10}$$

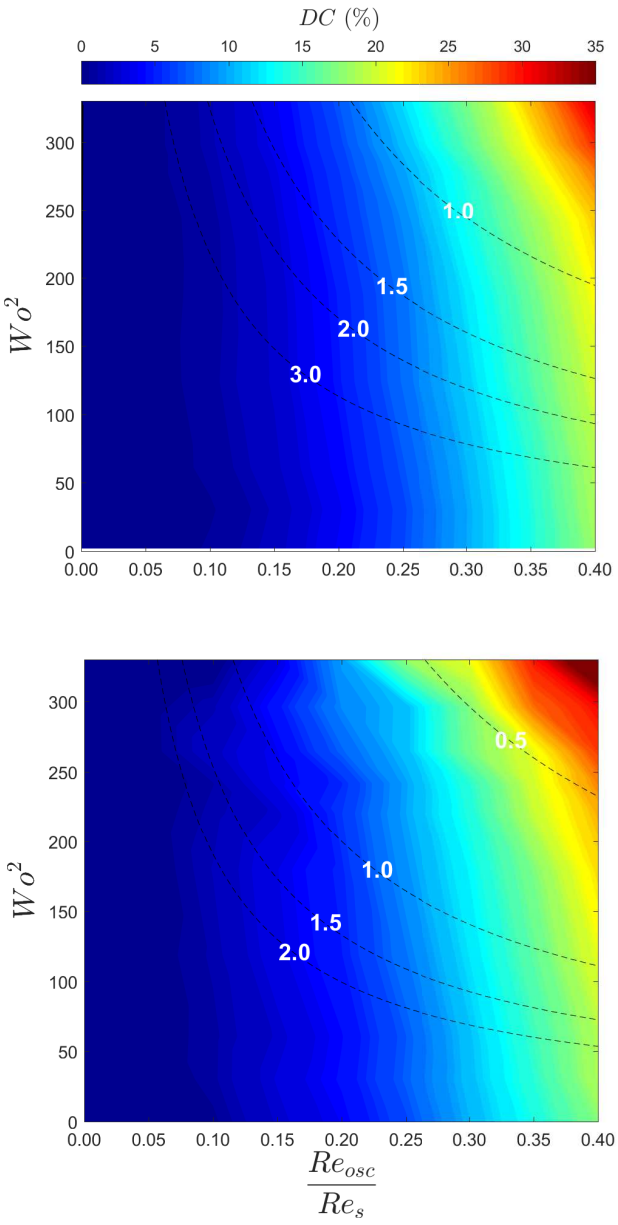

Figure 3.7: Contourmap of the drag change DC as a function of the velocity amplitude Re_{osc}/Re_s and Womersley number Wo^2, for: a) $Re_s = 5.7 \times 10^4$ and b) $Re_s = 2.9 \times 10^4$. The asymptotic lines represents the ratio of $\langle P_{d,tc} \rangle / P_{inrt}^{max}$, where $P_{d,tc} \sim C_f U_{sh}^2$ and $P_{inrt} \sim U_{sh}$.

The first term represents an analytical quasi-steady state solution DC_0 with the accompanying velocity modulation, while the second term involves the magnitude of the

boundary acceleration with the associated velocity fluctuation, where $\mathscr{K}^*$ is the conditional scaling-factor between the additional drag and the dimensionless acceleration under exact counter-rotating cylinders, in this case $\mathscr{K}^* = 7.3 \times 10^{-6}$.

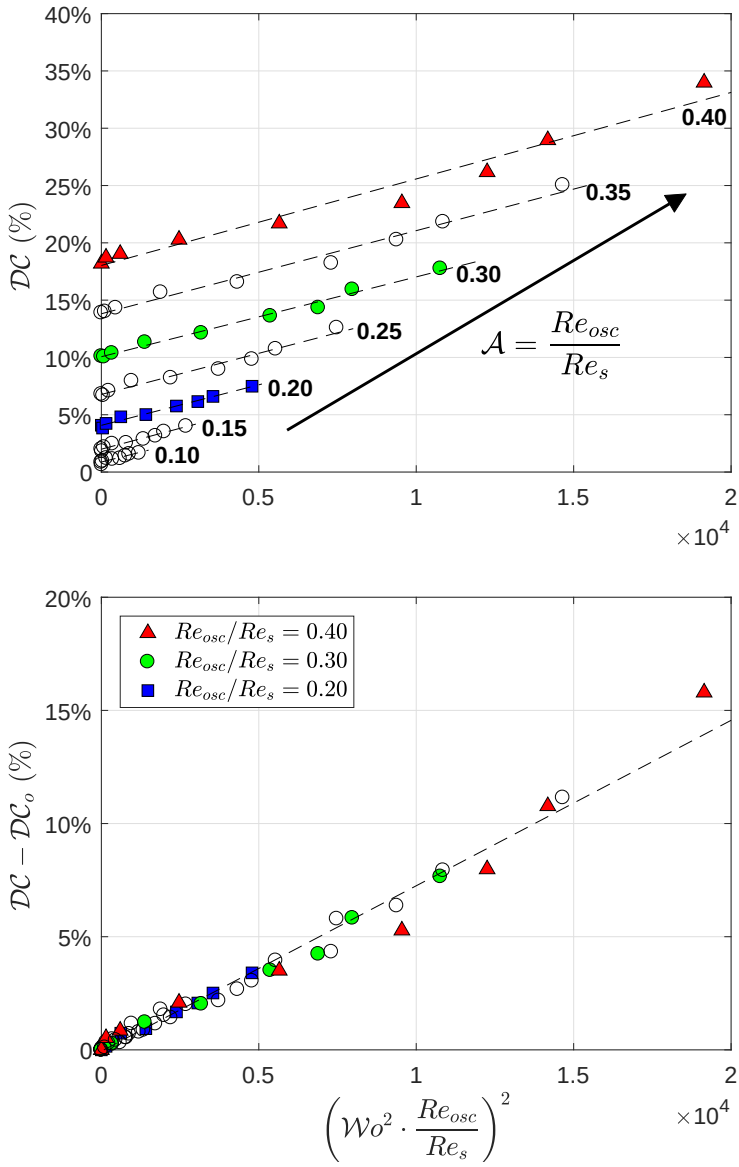

Figure 3.8: a) Drag change DC as a function of the acceleration, such that $DC = DC_0 + \mathscr{K}_{\mathscr{A}} \cdot \left(Wo^2 Re_{osc}/Re_s\right)^2$, with $\mathscr{A} = Re_{osc}/Re_s$. The individual slopes are $\mathscr{K}_{0.10} \approx 6.9 \times 10^{-6}$, $\mathscr{K}_{0.15} \approx 7.3 \times 10^{-6}$, $\mathscr{K}_{0.20} \approx 7.1 \times 10^{-6}$, $\mathscr{K}_{0.25} \approx 7.2 \times 10^{-6}$, $\mathscr{K}_{0.30} \approx 7.0 \times 10^{-6}$, $\mathscr{K}_{0.35} \approx 7.3 \times 10^{-6}$, $\mathscr{K}_{0.40} \approx 7.5 \times 10^{-6}$. b) Universal scaling relation $DC - DC_0 = \mathscr{K}^* \cdot \left(Wo^2 Re_{osc}/Re_s\right)^2$, with $\mathscr{K}^* \approx 7.3 \times 10^{-6}$.

3.3.2. RIBLET PERFORMANCE IN PERIODIC DRIVEN FLOWS

The influence of a periodically driven flow on the riblet drag performance has been studied in two steps; (1) drag measurements at several shear Reynolds numbers $Re_s = 2.0 \times 10^4$ to 9.0×10^4 under steady boundary conditions (i.e. $Re_{osc} = 0$), and (2) drag measurements at one shear Reynolds number $Re_s = 5.2 \times 10^4$ with varying oscillation Reynolds number $Re_{osc} = 0 - 1.8 \times 10^4$, at a constant oscillation period $T = 3.0$ s ($\simeq Wo \equiv 14.5$). In the current study, the drag change DC_{rib} has been determined by the change in the time-averaged drag between riblet and smooth surfaces under identical experimental conditions concerning Re_s, Re_{osc} and Wo:

$$DC_{rib} = \frac{1}{2}\left(\frac{\langle P_{d,tc}\rangle^{rib}}{\langle P_{d,tc}\rangle^{0}} - 1\right)_{Re_s, Re_{osc}, Wo} \tag{3.11}$$

where the superscripts rib and 0 refers to the measurements with the riblet and smooth surface respectively. The factor $\frac{1}{2}$ has been introduced to account for the applied riblets at the inner *and* outer cylinder surface.

Figure 3.9a represents an equivalent riblet-curve as reported by Bechert *et al.* [13], and indicates the drag change DC_{rib} as a function of the shear Reynolds number Re_s. The errorbars are significant larger at low shear Reynolds numbers, where the torque-sensor is less precise with relative much noise, as was already mentioned in Section 3.3.1. The current DC_{rib}-values are nearly identical to the earlier obtained values, where the riblets had been applied only at the inner cylinder surface [9]; a maximum drag reduction of $DC_{rib} = -3.5\%$ at $Re_s = 4.7 \times 10^4$, and a drag saving regime between $Re_s = 1.0 \times 10^4 - 8.5 \times 10^4$.

Figure 3.9b shows the riblet drag performance for periodic driven boundary flow, where the drag change DC_{rib} is a function of the applied velocity amplitude Re_{osc}/Re_s. When assuming quasi-steady-state conditions (i.e. $Wo \rightarrow 0$), the flow is hardly disturbed by the triangular protrusions and the drag would slightly change due to the velocity variation. However, under the actual experimental conditions (i.e. $Wo = 14.5$), the DC_{rib}-effect declines significantly when the velocity amplitude Re_{osc}/Re_s increases. As was demonstrated, large oscillation velocity amplitudes increases the turbulent drag and has been associated with the growth in turbulent fluctuations. It is believed that the turbulent fluctuations induce an earlier transition towards the surface roughness regime of the triangular riblets, which diminishes their drag reducing effectiveness, similar as was reported by Jiménez [14]. This suggests that the application of riblets becomes less effective when smaller oscillation periods T are applied. Higher intensive accelerations might even result in drag increase compared to the smooth surfaces under identical periodic driven boundary conditions.

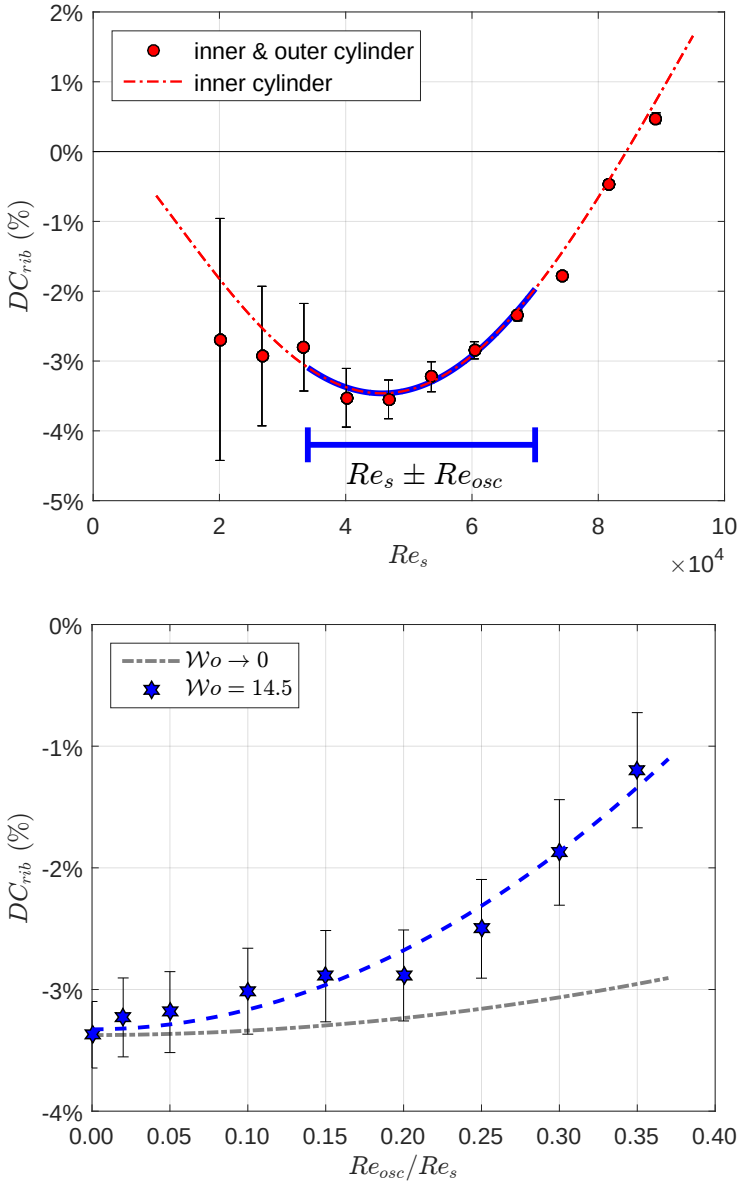

Figure 3.9: a) Riblet drag change DC_{rib} under constant boundary conditions. b) Riblet drag change DC_{rib} under periodic driven flow, $Re_s = 5.2 \times 10^4$ with varying oscillatory Reynolds number $Re_{osc} = 0 - 1.8 \times 10^4$, indicated by $Re_s \pm Re_{osc}$ in Figure 3.9a. The dash-dotted line suggests the quasi-steady-state condition, dashed line is best-fit to the data points. Errorbars indicate the estimated 95% confidence interval.

3.4. SUMMARY & CONCLUSION

To summarize, a Taylor-Couette system was used to study the frictional drag under periodic driven boundary conditions for exact-counter rotating cylinders. The inner and outer cylinder velocity were modulated as a sinusoidal function, such that the shear velocity between the two cylinders became $U_{sh} = \langle U_{sh} \rangle - \Delta U_{sh} \sin(2\pi t/T)$. The chosen scaling parameters are the shear Reynolds number $Re_s = 5.7 \times 10^4$, the oscillation Reynolds number $Re_{osc} = 0 - 2.3 \times 10^4$ and the Womersley number $Wo = 5.5 - 18.7$.
Very small velocity amplitudes $\mathscr{A} = Re_{osc}/Re_s \leq 0.05$ have a marginal impact on the drag change DC in contrast to steady boundary conditions as the perturbations of these velocity amplitudes are considered to be smaller than the turbulent velocity fluctuations (i.e. $\Delta U_{sh} < u'$), for which they are absorbed into the general turbulent statistics. Larger velocity amplitudes $\mathscr{A} = Re_{osc}/Re_s \geq 0.10$ start to induce additional turbulent fluctuations and with that a growth in turbulent drag.
Furthermore, it was validated that the Womersley number Wo is the most important parameter to quantify the additional turbulent drag. For very low Womersley numbers ($Wo \ll 1$), the viscous forces are predominating the transient forces and the drag increase DC equals the quasi-stationary relation $DC_0 \sim \frac{1}{T}\int_0^T (U_{sh}/\langle U_{sh} \rangle)^{11/4}$. However, for higher Womersley number Wo, the acceleration becomes more severe and surpasses the viscous forces, which results in a substantial drag increase. In addition to the quasi-stationary value (DC_0), the total drag change DC can be described by a second term related to the dimensionless acceleration, which is quantified by $\mathscr{K}^* \cdot \left(Wo^2 Re_{osc}/Re_s\right)^2$ with $\mathscr{K}^*$ as the conditional scaling-factor.
The drag performance of riblets under periodic driven boundary conditions was identified. Under weak accelerations, the riblet surface structures are capable to reduce frictional drag of the periodic driven turbulent flow compared to a smooth surface. The efficiency to reduce frictional drag declines drastically when the acceleration becomes more moderate. Indications support the belief that the application of riblet surfaces under vigorous accelerating conditions will only increase the frictional drag compared to a smooth surface.

REFERENCES

[1] M. Ö. Çarpinlioglu and M. Y. Gündogdu, *A critical review on pulsatile pipe flow studies directing towards future research topics,* Flow Measurement and Instrumentation **12**, 163 (2001).

[2] M. Nabavi and K. Siddiqui, *A critical review on advanced velocity measurement techniques in pulsating flows,* Measurement science and technology **21**, 042002 (2010).

[3] R. Truesdell, P. Vorobieff, L. Sklar, and A. Mammoli, *Mixing of a continuous flow of two fluids due to unsteady flow,* Physical Review E **67**, 066304 (2003).

[4] M. Mackley and P. Stonestreet, *Heat transfer and associated energy dissipation for oscillatory flow in baffled tubes,* Chemical Engineering Science **50**, 2211 (1995).

[5] E. A. Elshafei, M. S. Mohamed, H. Mansour, and M. Sakr, *Experimental study of heat transfer in pulsating turbulent flow in a pipe,* International Journal of Heat and Fluid Flow **29**, 1029 (2008).

[6] C. Gillham, P. Fryer, A. Hasting, and D. Wilson, *Enhanced cleaning of whey protein soils using pulsed flows,* Journal of Food Engineering **46**, 199 (2000).

[7] D. N. Ku, *Blood flow in arteries,* Annual review of fluid mechanics **29**, 399 (1997).

[8] C. Poelma, P. Vennemann, R. Lindken, and J. Westerweel, *In vivo blood flow and wall shear stress measurements in the vitelline network,* Experiments in fluids **45**, 703 (2008).

[9] A. J. Greidanus, R. Delfos, S. Tokgoz, and J. Westerweel, *Turbulent Taylor-Couette flow over riblets: drag reduction and the effect of bulk fluid rotation,* Experiments in Fluids **56**, 1 (2015).

[10] P. Zandbergen and D. Dijkstra, *Von kármán swirling flows,* Annual review of fluid mechanics **19**, 465 (1987).

[11] R. Trip, D. Kuik, J. Westerweel, and C. Poelma, *An experimental study of transitional pulsatile pipe flow,* Physics of fluids **24**, 014103 (2012).

[12] R. A. Verschoof, A. K. te Nijenhuis, S. G. Huisman, C. Sun, and D. Lohse, *Periodically driven taylor–couette turbulence,* Journal of Fluid Mechanics **846**, 834 (2018).

[13] D. Bechert, M. Bruse, W. Hage, J. T. Van der Hoeven, and G. Hoppe, *Experiments on drag-reducing surfaces and their optimization with an adjustable geometry,* Journal of Fluid Mechanics **338**, 59 (1997).

[14] J. Jiménez, *Turbulent flows over rough walls,* Annu. Rev. Fluid Mech. **36**, 173 (2004).

4

WATER TUNNEL ASSESSMENT AND CHARACTERIZATION

4.1. INTRODUCTION

Frictional drag of surfaces is of importance to many sectors with internal and external flows wherein the turbulent boundary layers play a crucial role in the total energy consumption. Drag reduction may particularly be relevant to industrial applications where reduction in the pressure gradient in pipe flows and reduction in fuel consumption during vehicle transport can generate substantial energy savings, and with that ecological and economical benefits.

In order to study the fluid-surface interaction and the related frictional resistance of surfaces, the water tunnel at the Delft University of Technology (TU Delft) was used as a test facility. The water tunnel was previously used in the research of and described by Foeth [1], Zverkhovskyi [2] and Pennings [3]. In this chapter, the characterization of the water tunnel and coherent flow are investigated to quantify the global and the local flow velocities, and the drag force of a turbulent flow along a flat plate.

4.2. EXPERIMENTAL FACILITY

4.2.1. WATER TUNNEL

The current water tunnel was originally constructed as a cavitation tunnel for the investigation of cavitation for propellers and hydrofoils [1]. For the study of (turbulent) boundary layer flows, Zverkhovskyi [2] redesigned and replaced the original test section and diffuser, such that the test section length was enlarged from 0.6 to 2.0 m, which made it possible to investigate the drag reduction by air cavities. The closed-loop water flow is propelled by a motor driven impeller. Originally, the water bulk velocity was controlled by a fixed shaft revolution rate that corresponds to a specific mean bulk velocity, but resulted in large velocity fluctuations of the water flow. These bulk velocity fluctuations were minimized by Pennings [3] by optimizing the velocity control system that drives the tunnel impeller. The pressure drop over the contraction part of the water tunnel is measured by a differential pressure sensor (DPS), which indicates the flow bulk velocity in the test section (Eq. 4.1). The installation of an analog motor controller made it possible to couple the impeller-motor to the DPS in order to obtain an active feedback control system that was capable of maintaining a defined pressure drop over the contraction. The improved control system reduced the bulk velocity fluctuations tremendously compared to the original configuration [3]. In the current study, two types of pressure sensor diaphragms were applied to the DPS (Validyne, DP15) in order to obtain two bulk velocity ranges with high accuracy (±0.5% full-scale (FS)). The first transducer configuration (3-30F, $\Delta P < 8.6$ kPa) has an operating velocity range of $0.4 < U_b < 4.2$ m/s, while the second transducer configuration (3-34F, $\Delta P < 22$ kPa) is limited to a bulk velocity of $U_b < 6.7$ m/s. In the remainder of this chapter, the two sensor configurations are labeled "sensor low U_b" and "sensor high U_b", respectively.

A nearly constant bulk velocity U_b is maintained over the length of the test section due to a reclining bottom wall, which partially compensates the boundary layer growth in the streamwise direction. The inlet cross-section area of the test section is 300×300 mm^2, while the outlet cross-section area is 300×315 mm^2. The maximum applied bulk velocity is $U_b = 5.5$ m/s. The incoming flow is tripped with a 2 mm high zigzag tripwire to ensure a turbulent boundary layer at all relevant tunnel velocities. The tripwire is

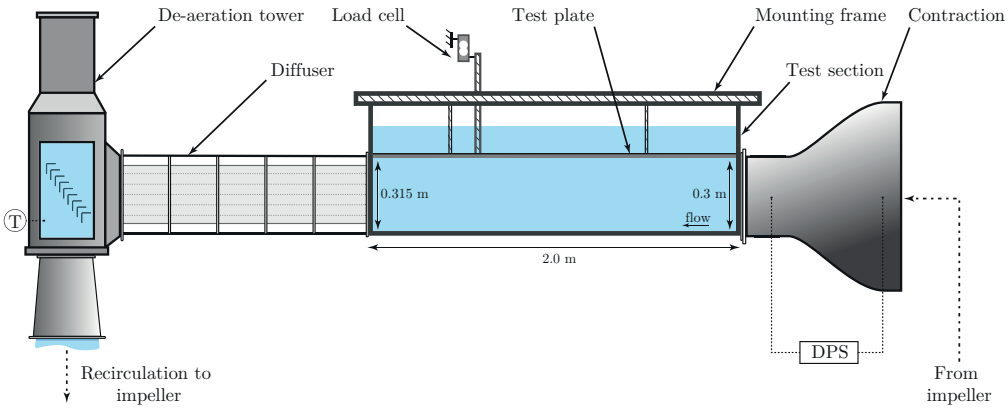

Figure 4.1: Schematic illustration of the water tunnel. The flow is from right to left.

located 100 mm before the test section to minimize the transition effects. The water temperature is recorded with a PT-100 sensor in the de-aeration tower.

Several flat test plates were used in order to measure the frictional properties of different surfaces. First, the test plates were mounted to a moving frame placed inside the water tunnel. The test plates function as the top wall of the water tunnel and are aligned with the top wall of the contraction part and the diffuser of the water tunnel with high precision via a digital level unit ($\pm 0.01^o$). The total surface area of a test plate is 1998×297 mm^2, and it can move freely during the force measurements. The gaps around the test plate (approx. 1.0-1.5 mm) are shielded in order to minimize possible flow disturbances. The frictional properties of the test plates are determined via a force balance system that includes a calibrated load cell. The load cell measures the longitudinal displacement that is induced by the friction force of the water flow on the test plate, typically around 1- 35 N. The force balance system and the calibration procedure are described in more detail by Zverkhovskyi [2]. The data sampling frequency for all parameters was $F_s = 1$ kHz. Optical measurement techniques, such as Particle Image Velocimetry (PIV) and Background-Oriented Schlieren (BOS), are applicable due to the fully optical access of the test section.

4.2.2. PARTICLE IMAGE VELOCIMETRY SYSTEM

Particle Image Velocimetry (PIV) is an optical measurement technique that is often used in fluid mechanics research and engineering [4]. The method identifies the instantaneous velocity fields of a flow by estimating the displacements of small seeding particles that follow the fluid motions with high accuracy. The seeding particles are illuminated by a thin laser light sheet creating an imaging plane, for example oriented in the streamwise/wall-normal direction (i.e. the xy-plane). An optical camera records this planar image and registers the location of the illuminated particles.
Two consecutively recorded images at time t and $t + \Delta t$ are used to determine the in-

stantaneous velocity field. The image plane is divided into multiple small areas called the interrogation windows. For example, an interrogation window can have an area of 32 × 32 pixels that contains a small group of particles (open symbols, Fig. 4.2a). The second consecutive image at time $t + \Delta t$ contains the group of particles that have moved inside the interrogation window (closed symbols, Fig. 4.2a). A cross-correlation method estimates the group particle displacement between the two recorded images. The correlation map identifies a maximum correlation value that represents the most probable average displacement over the particles (Fig. 4.2b). Consequently, the streamwise and wall-normal components of the velocity in the corresponding interrogation window are estimated as $u = \Delta x/\Delta t$ and $v = \Delta y/\Delta t$, respectively. The velocity vectors are obtained from multiple interrogation windows in the entire field of view, together reconstructing the instantaneous velocity field within the plane of observation. Pre- and post-processing methods are often applied to enhance the quality and accuracy of the estimated velocity field.

In this study, a standard 2D-2C PIV system was applied to the water tunnel facility (Fig. 4.3). For the low operating velocity range (i.e. "sensor low U_b"), three measurement positions in the streamwise direction were allocated to determine the local velocities and flow characteristics of the water tunnel. The positions were located at $x_1 = 0.2$ m, $x_2 = 1.0$ m and $x_3 = 1.7$ m from the leading edge of the test plate. At all three positions, a large field of view (22×17 cm^2) was applied to determine the bulk velocity U_b and to measure the turbulent intensity u_{rms} and v_{rms} at the center of the water tunnel. A second smaller field of view (7.5×6.0 cm^2) was applied to study the velocity profile in more detail and to identify the boundary layer growth over the length of the test section. The measurement plane was situated at the centerline of the water tunnel to minimize possible side wall disturbances. Only the small field of view (7.5×6.0 cm^2) was applied at the last position ($x_3 = 1.7$ m) for the transducer configuration "sensor high U_b".
The seeding particles in the field of view were illuminated by a laser light sheet using a double-pulsed 50 mW Nd:YAG laser (Litron L-class 50-50). The images were recorded by a 1280×1024 pixel CCD-camera (FlowMaster, LaVision). The double-pulsed double-frame recording was performed at a low frequency (3-4 Hz) until a total number of 500 consecutive image pairs was captured, which would be sufficient to achieve statistical convergence of the mean velocity field data. Hollow glass particles (Sphericell) with a particle diameter of $d_p = 10$ μm were used as tracers ($\rho_p = 1.1 \times 10^3$ kg/m^3) and were assumed to accurately follow the flow. Calibration, data acquisition, and image processing were performed using commercial software (Davis, LaVision). A multi-pass interrogation method was used, where the final interrogation windows had a size of 16 × 16 pixels with a 50% overlap. The corresponding spatial resolution of the velocity vectors were 1.36 mm and 0.47 mm for the large and the small field of view, respectively. Spurious vectors were identified using the universal outlier detection method [5] and were replaced by linear interpolation.

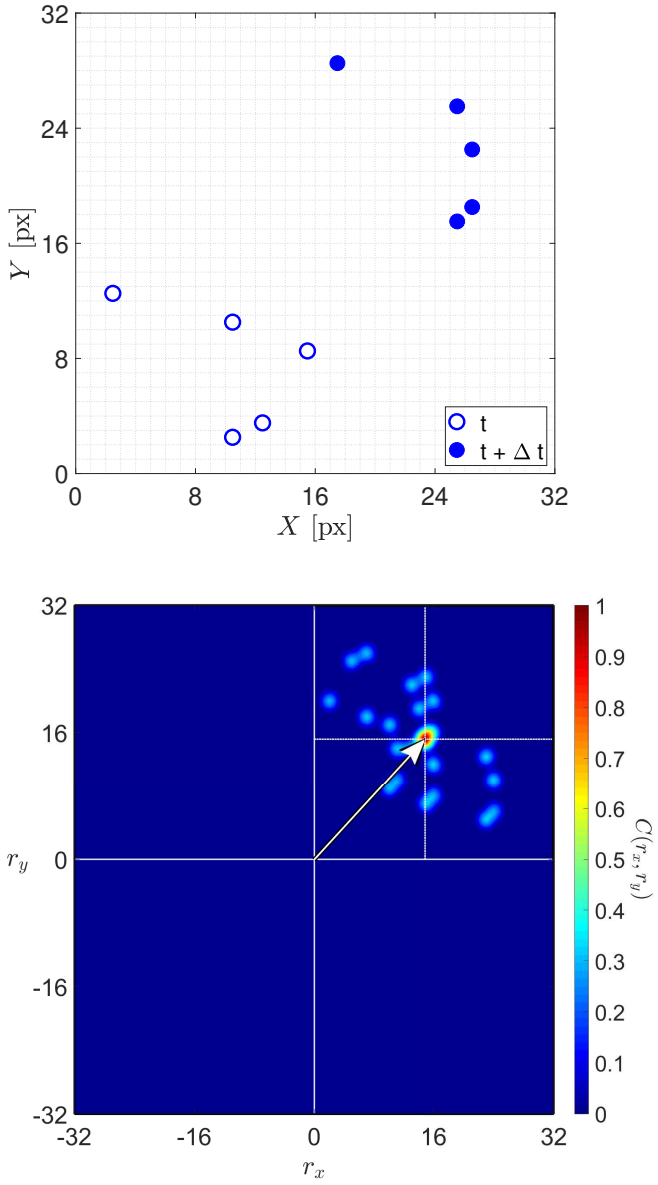

Figure 4.2: Concept of the 2D-2C PIV method. a) A group of particles inside an interrogation window (32 × 32 pixels), with the first image at t (open symbols) and the second image at $t + \Delta t$ (closed symbols). b) The correlation map with a correlation maximum at $r_x = 14.9$ and $r_y = 15.2$, representing the average pixel displacement inside the interrogation window. Calibration determines the length scale of one pixel in the physical domain.

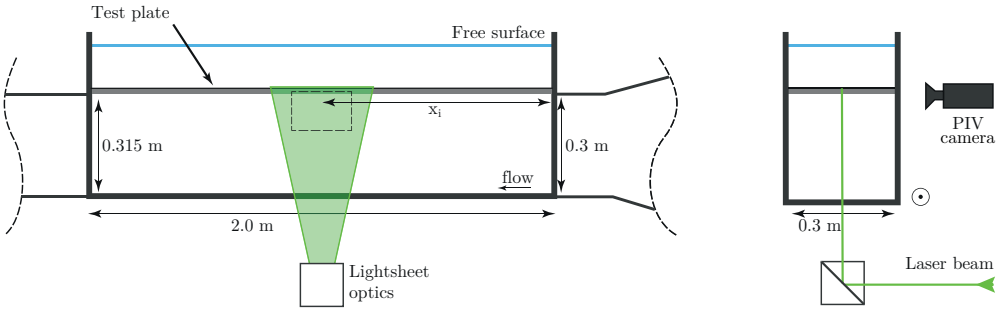

Figure 4.3: Illustration of the experimental PIV set-up applied to the test section of the facility. The field-of-views are located close to the wall at $x_1 = 0.2$ m, $x_2 = 1.0$ m and $x_3 = 1.7$ m from the leading edge of the test plate. The laser sheet is situated at the centerline of the water tunnel. The flow moves from right to left.

4.3. RESULTS

The bulk velocity U_b and the friction-induced drag force F_d are registered as *global* characteristic parameters of the water tunnel, while the PIV measurements indicate *local* flow characteristics at the allocated positions. The local friction is prescribed by the fluid motions of the flow at that location, and characterizes the boundary layer thickness and the shape of the velocity profile. In theory, integration of the local friction estimates the global friction of the total test surface [6].

4.3.1. WATER TUNNEL CHARACTERISTICS

The pressure difference ΔP over the contraction part of the water tunnel is monitored by the aforementioned DPS and is used to control the flow velocity U_b of the water tunnel. Assuming incompressible flow, the differential pressure ΔP is converted into a bulk velocity dimension U_b via the equation of Bernoulli:

$$U_b = \sqrt{\frac{2\Delta P}{\rho(1-(S_2/S_1)^2)}} \tag{4.1}$$

The parameter S_2/S_1 represents the outlet/inlet area-ratio of the contraction part over which the pressure difference is measured ($S_2/S_1 \sim 0.17$).

Figure 4.4a shows a typical distribution of the data regarding the estimated bulk velocity U_b at the outlet of the contraction section derived from the measured pressure drop ΔP (Eq. 4.1), while Figure 4.4b shows the distribution of the measured force signal F_d induced by the frictional drag of the turbulent flow on the test plate. Both distributions can be considered to be normal distributions. The data contain fluctuations around the mean value, which are presumed to be common characteristic artifacts of the water tunnel.

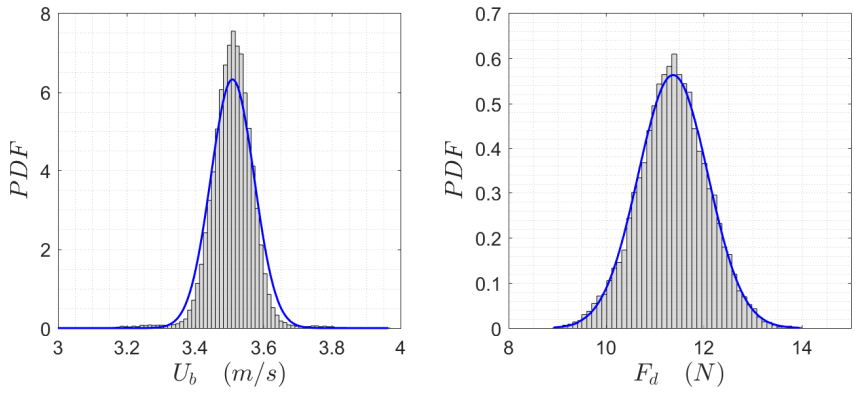

Figure 4.4: Distribution of a) the estimated velocity at the contraction outlet and b) the measured force signal, at bulk velocity U_b = 3.51 m/s. To both distributions, a Gaussian fit curve (normal distribution) is added.

The relative root-mean-square (RMS) values of the bulk velocity U_{rms}/U_b and the drag force F_{rms}/F_d are displayed in Figure 4.5. In general, the relative RMS-values are high for low bulk velocities U_b and decrease with higher bulk velocities. An exception is observed around U_b =2.0-2.4 m/s with high relative RMS-values. It is believed that the frequency of operational vibrations at this bulk velocity U_b is in the order of the eigen-frequency of the tunnel and test section. It should be noted that this did not influence the global bulk velocity U_b and drag force $\bar{F}_d$ values, as was indicated by new measurements at a later stage.

The drag force F_d, the bulk velocity U_b, and the water temperature were measured and analyzed in order to determine the frictional properties of a conventional flat plate and to quantify the accuracy of the water tunnel as a test facility. The measured drag

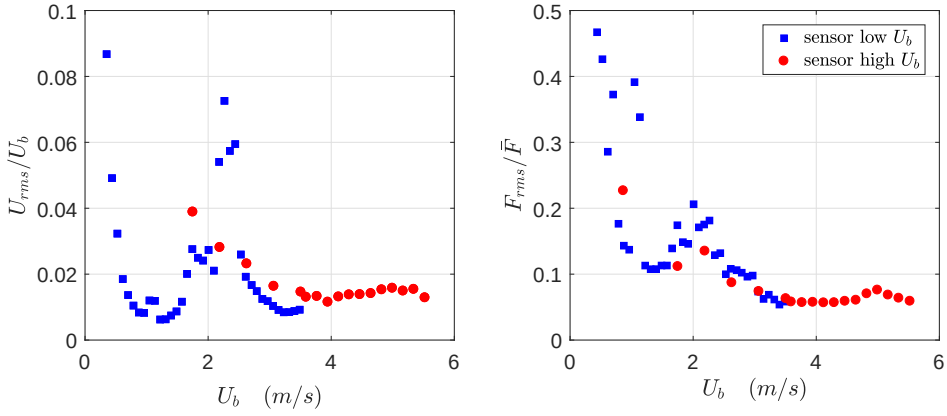

Figure 4.5: Root-mean-square (RMS) values based on the Gaussian fit of a) the velocity data and b) the force signals.

force $\bar{F}_d$ represents the averaged wall shear stress $\bar{\tau}$ of the total plate area A. The wall shear stress $\bar{\tau}$ is normalized with the dynamic pressure $\frac{1}{2}\rho U_b^2$ to obtain the global drag coefficient C_d of the test plate (Eq. 4.2):

$$C_d = \frac{\bar{F}_d}{\frac{1}{2}\rho U_b^2 A} \tag{4.2}$$

The drag coefficient C_d is related to the Reynolds number Re_L based on the length of the test plate $L = 2$ m, with $Re_L = U_b L/\nu$. In order to quantify the capabilities and accuracy of the present water tunnel, the obtained results are compared with literature. A common empirical relation to compute the drag coefficient C_d for smooth surfaces is Grigson's correlation, which is given by:

$$C_d = \left(0.93 + 0.1377(log_{10}Re_L - 6.3)^2 - 0.06334(log_{10}Re_L - 6.3)^4\right) \frac{0.075}{(log_{10}Re_L - 2)^2} \tag{4.3}$$

In practice, the boundary layer has a virtual origin located upstream of the leading edge of the test plate, due to e.g. the contraction section and the trip-wire. The PIV measurements of the velocity profiles indicated that this virtual origin is located around 0.7-1.0 m upstream.
Figure 4.6 displays the measured drag coefficient C_d as a function of the Reynolds number Re_L and indicates that the obtained results are in good agreement with the correlation values: the mean disparity is around ±0.76%, the standard deviation is 0.81% and the maximum deviation is 1.8%. The errorbars represent the 95% confidence intervals $\sim \pm 2C_{d,rms}/\sqrt{N}$, where $C_{d,rms}$ is proportional to F_{rms}/U_b^2 and N is the estimated amount of independent data points. The variation of the errorbars are among others related to the RMS-values of the force signal; see Figure 4.5.

4.3.2. FLOW CHARACTERISTICS

GENERAL BULK FLOW CONDITIONS

The velocity fields at the three allocated positions x_1, x_2 and x_3 are obtained via PIV measurements. The bulk velocity U_b was verified and indicated a small acceleration of the flow over the length of the water tunnel, which results in a very small favorable pressure gradient dP/dx. Joshi *et al.* [7] quantified the strength of the imposed favorable pressure gradient in terms of the acceleration parameter $K = \frac{\nu}{U_b^2}\frac{dU_b}{dx}$. The acceleration parameter of the current measurements is $K = \mathcal{O}(10^{-8})$ for all imposed bulk velocities U_b and suggests that the pressure gradient has negligible effects on the turbulent structures in the boundary layer, as $K < \mathcal{O}(10^{-6})$.

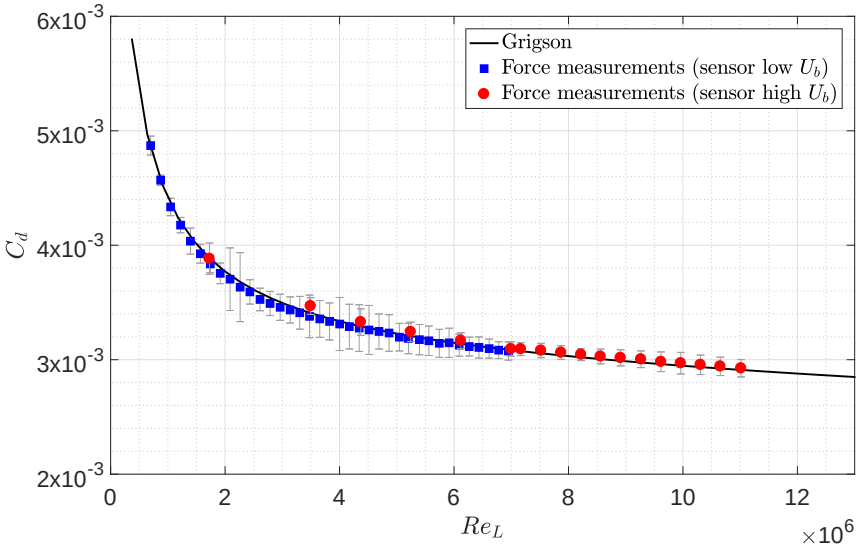

Figure 4.6: Global measured drag coefficient C_d versus Reynolds number Re_L.

The level of turbulence is defined by the turbulence strength of the flow, u_{rms} and v_{rms}. The honeycomb, the contraction section and the trip-wire at the walls induce some turbulence at the start of the test section. For a spatially developing flow, the turbulent boundary layer grows along the wall in streamwise direction. According to Sagaut and Cambon [8], the turbulent kinetic energy (TKE) at the centerline decays in streamwise direction, which is supported by the obtained RMS-values of u and v shown in Table 4.1. As reported, the decay is small at low Reynolds numbers Re_L ($= U_b L/\nu$), which explains the higher turbulence intensity u_{rms} at the initial positions x_1 and x_2 for low bulk velocity U_b. Finally, assuming cross-flow of the water tunnel (i.e. $w = v$), Table 4.1 indicates nearly isotropic turbulence $u_{rms} \cong v_{rms} \cong w_{rms}$ with low turbulence intensity at the centerline for bulk velocities of $U_b = 1.7$ m/s and above.

Table 4.1: Positional turbulence intensity values u_{rms}/U_b and v_{rms}/U_b at the centerline of the water tunnel. Positions: $x_1 = 0.2$ m, $x_2 = 1.0$ m and $x_3 = 1.7$ m.

U_b (m/s)	(%)	x_1	x_2	x_3
0.35	u_{rms}	4.4	3.9	1.1
	v_{rms}	1.1	3.4	2.3
0.52	u_{rms}	2.8	3.1	0.9
	v_{rms}	1.1	2.5	1.7
0.70	u_{rms}	2.1	2.3	0.8
	v_{rms}	1.0	2.0	1.4
0.87	u_{rms}	1.8	1.7	0.7
	v_{rms}	0.9	1.7	1.0
1.04	u_{rms}	1.7	1.5	1.2
	v_{rms}	1.0	1.6	1.1
1.22	u_{rms}	1.4	1.4	1.4
	v_{rms}	0.9	1.3	1.2
1.74	u_{rms}	1.0	1.1	0.9
	v_{rms}	0.9	1.1	0.8
2.61	u_{rms}	0.8	0.8	0.7
	v_{rms}	0.8	0.9	0.7
3.48	u_{rms}	0.7	0.9	0.8
	v_{rms}	0.7	0.9	0.7

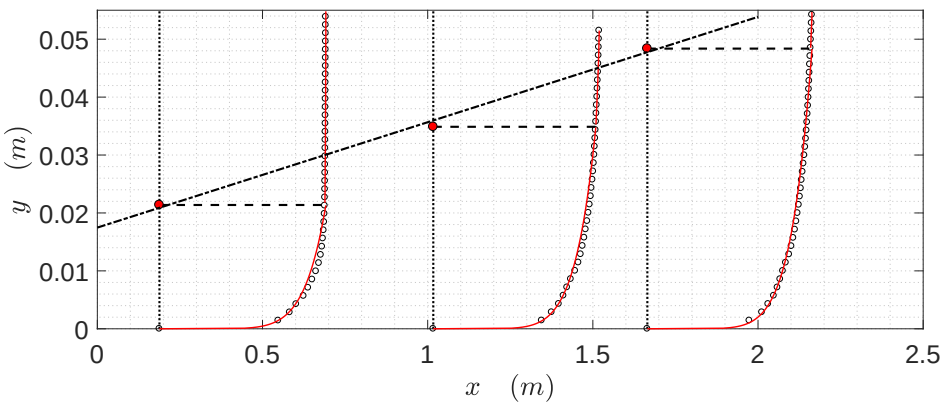

Figure 4.7: Mean velocity profiles $\bar{u}(y)$ for $U_b = 3.48$ m/s at x_1, x_2 and x_3. The solid lines displays the local fit $\bar{u}(y) = U_b(y/\delta_{99})^{1/8}$. The closed symbols indicate the local boundary layer thickness $\delta_{99} = (45/4)\theta_x$ at x_1, x_2 and x_3. Dot/dashed line represents the boundary layer thickness growth in streamwise direction, here $\delta_{99}(x) = 0.018x + 0.018$.

BOUNDARY LAYER DEVELOPMENT

The boundary layer (BL) grows in streamwise direction along the wall. Figure 4.7 presents the mean velocity profiles at the three positions x_1, x_2 and x_3 for bulk velocity U_b = 3.48 m/s. The velocity profiles of the boundary layer approximately satisfy $\bar{u}(y) = U_b(y/\delta_{99})^{1/8}$, with streamwise velocity u, mean bulk velocity U_b, wall-normal distance y, and BL thickness δ_{99} that indicates the distance from the wall where $\bar{u}$ has 99% of the value of U_b. The BL thickness δ_{99} is determined via the momentum thickness θ, which is defined by the integral over the velocity profile (Eq. 4.4):

$$\theta = \int_0^y \frac{\bar{u}}{U_b}\left[1 - \frac{\bar{u}}{U_b}\right] dy \tag{4.4}$$

and

$$\theta \approx \int_0^{\delta_{99}} \left(\frac{y}{\delta_{99}}\right)^{1/8}\left[\left(1 - \frac{y}{\delta_{99}}\right)^{1/8}\right] dy = \frac{4}{45}\delta_{99} \tag{4.5}$$

The BL thickness δ_{99} becomes $\delta_{99} = (45/4)\theta$, considering the $(1/8)^{th}$-power for the velocity profiles (Eq. 4.5). Figure 4.7 denotes a linear growth of the turbulent boundary layer over distance. Given the linear growth, the estimated averaged momentum thickness and BL thickness at $x_0 = 0$ m are $\theta|_{x_0} = 1.6$ mm and $\delta_{99}|_{x_0} = 1.8$ cm, respectively. For bulk velocities above $U_b > 1.5$ m/s, the BL thickness at position x_3 is in the order of $\delta_{99} = 0.045 - 0.055$ m.

FRICTION DETERMINATION FROM VELOCITY DATA

The local velocity measurements assist the reconstruction of the total plate drag force. Proper values are obtained by the Clauser chart method [9], which is based on the estimation of the local wall friction velocity u_τ. The local wall friction velocity u_τ is determined by fitting the velocity profile to the universal law of the wall in the logarithmic overlap region of the boundary layer ($y^+ > 50$ and $y/\delta_{99} < 0.2$):

$$\bar{u}^+ = \frac{1}{\kappa}\ln(y^+) + B \tag{4.6}$$

where $\bar{u}^+ = \bar{u}/u_\tau$, $y^+ = yu_\tau/\nu$, $\kappa = 0.41$ is the von Kármán constant and $B = 5.2$ is an additive constant [10]. For this method, a substantial thickness of the logarithmic overlap layer is preferred to achieve adequate results (i.e. high-Re_L flow). The local wall shear stress τ_w is subsequently obtained by $\tau_w = \rho u_\tau^2$, which delivers the local skin-friction coefficient $c_f = 2\tau_w/(\rho U_b^2)$. Figure 4.8 illustrates the local skin-friction coefficient c_f as a function of the local Reynolds number $Re_x = U_b x/\nu$. The local Reynolds numbers corresponds with the positions x_1, x_2 and x_3. The dashed line indicates the empirical power law $c_f = a(Re_x)^b$ that follows the obtained local skin-friction coefficient values

c_f. Integration of the empirical power law eventually determines the overall plate drag coefficient C_d for the specific Reynolds number Re_L. Figure 4.9 displays these reconstructed drag coefficients C_d for $Re_L = 0.7 \times 10^6 - 10.4 \times 10^6$ (open symbols), which are compared to the obtained results by the drag force measurements (solid line). The overall mean difference is ±2.7% with a standard deviation of 3.2% and a maximum deviation of 10.1% at $Re_L = 0.7 \times 10^6$. It should be noted that for the second transducer configuration ("sensor high U_b"), the local shear stress values at x_1 and x_2 are extrapolated from the local shear stress values obtained by the Clauser chart method with the first transducer configuration ("sensor low U_b"), when considering $\tau_w \propto U_b^2$. Furthermore, the results are sensitive to the choice of κ and B, as a wide range of values have been reported, e.g. $0.33 \leq \kappa \leq 0.45$ and $3.5 \leq B \leq 6.1$ [11]. Nevertheless, the initial choice of $\kappa = 0.41$ and $B = 5.2$ appears to fulfill a proper reconstruction of the total plate drag force, in contrast to other κ-values (dotted lines in Fig. 4.9).

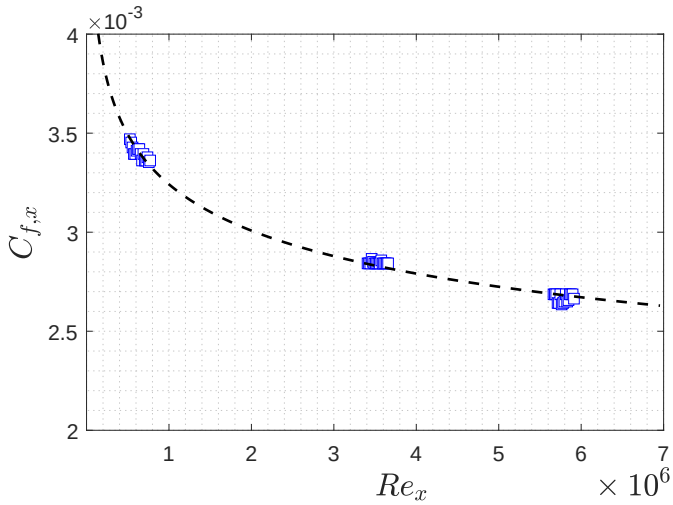

Figure 4.8: Local skin-friction coefficient $c_f = 2\tau_w/(\rho U_b^2)$ as a function of the local Reynolds number $Re_x = U_b x/\nu$ for bulk velocity $U_b = 3.5$ m/s. Dashed line indicates the empirical power law $c_f = a(Re_x)^b$, with $a = 0.0144$ and $b = -0.108$.

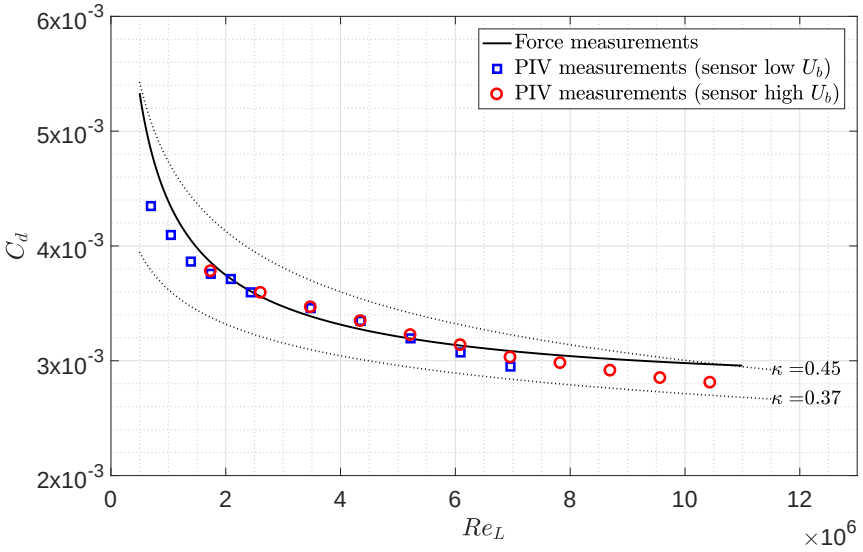

Figure 4.9: Plate drag coefficient C_d versus Reynolds number Re_L. Solid line: obtained via force measurements; Open symbols: reconstructed via the Clauser chart method; Dotted lines: alternative reconstructed results with initial choice of the von Karman constant, i.e. $\kappa = 0.37$ and $\kappa = 0.45$.

4.4. SUMMARY & CONCLUSION

The water tunnel was used in order to study the fluid-structure interaction of a turbulent boundary layer (TBL) with its surface. The water tunnel and turbulent flow were characterized by global and local measurements in order to quantify the accuracy and proper use of the test facility for frictional drag studies.

The global flow velocity and shear stress measurements were performed by a differential pressure sensor and a force balance system, respectively. Small fluctuations in the controlled bulk velocity U_b as well as in the friction-induced drag force F_d were observed, both related to the characteristic features of the water tunnel. These fluctuations had no anomalous effects on the obtained results.

The 2D-PIV measurements were used to determine the local velocity fields. The boundary layer growth in the streamwise direction induces a small acceleration of the flow, but was considered to have a negligible effect on the turbulent structures in the boundary layer since the acceleration parameter is $K < O(10^{-6})$. At high bulk velocity $U_b > 1.7$ m/s, the bulk flow is considered to be nearly isotropic with low turbulence intensity at the centerline of the water tunnel (i.e. $u_{rms} \cong v_{rms} \cong w_{rms}$).

The global force measurements result in an identical response of the shear stress following Grigson's empirical relation $C_d = f(Re_L)$ with a high accuracy. The local velocity profiles facilitate the reconstruction of the total shear stress of the fluid motions. The Clauser chart method showed to be a suitable method to quantify the local skin-friction coefficient c_f and accordingly the total frictional drag of the plate C_d. When following this procedure, the results are sensitive to the initial choice of parameters κ and B.

REFERENCES

[1] E.-J. Foeth, *The structure of three-dimensional sheet cavitation*, Ph.D. thesis, Delft University of Technology (2008).

[2] O. Zverkhovskyi, *Ship drag reduction by air cavities*, Ph.D. thesis, Delft University of Technology (2014).

[3] P. Pennings, *Dynamics of Vortex Cavitation*, Ph.D. thesis, Delft University of Technology (2016).

[4] R. J. Adrian and J. Westerweel, *Particle image velocimetry*, 30 (Cambridge University Press, 2011).

[5] J. Westerweel and F. Scarano, *Universal outlier detection for piv data,* Experiments in fluids **39**, 1096 (2005).

[6] F. M. White, *Fluid mechanics* (WCB, 1999).

[7] P. Joshi, X. Liu, and J. Katz, *Effect of mean and fluctuating pressure gradients on boundary layer turbulence,* Journal of Fluid Mechanics **748**, 36 (2014).

[8] P. Sagaut and C. Cambon, *Incompressible homogeneous isotropic turbulence,* in *Homogeneous Turbulence Dynamics* (Springer, 2018) pp. 99–244.

[9] F. H. Clauser, *The turbulent boundary layer,* in *Advances in applied mechanics*, Vol. 4 (Elsevier, 1956) pp. 1–51.

[10] S. B. Pope, *Turbulent flows,* (2001).

[11] E.-S. Zanoun, F. Durst, and H. Nagib, *Evaluating the law of the wall in two-dimensional fully developed turbulent channel flows,* Physics of Fluids **15**, 3079 (2003).

5

COMPLIANT SURFACES IN TURBULENT FLOWS

5.1. INTRODUCTION

The interaction of compliant surfaces with their wall-bounded flows has been studied over decades since the early experiments published by Kramer [1, 2]. The main research investigates the application of compliant coatings to delay laminar-to-turbulent transition, reduce skin friction drag, and suppress flow-induced noise and vibrations. Theoretical analyses on system instabilities, experimental investigations, and direct numerical simulations over the years have shown the (im)possibilities of compliant materials effecting the desired aforementioned purpose, resulting in a series of contradictions and controversies. A review on classical and more recent studies are given by Bushnell *et al.* [3], Riley *et al.* [4] and Gad-el Hak [5], which delivers a valuable direction to the state-of-the-art research on compliant walls.

The present knowledge quantifies the compliance of flexible walls as a result of the response to the pressure fluctuations in the turbulent boundary layer of the flow. Dominant near-wall flow structures instigate quasi-periodic bursting events and result in velocity fluctuations in the streamwise and wall-normal directions (i.e. u' and v'), which are the elementary components of the Reynolds shear stress ($-\rho\langle u'v'\rangle$) in the turbulent boundary layer [6, 7]. The velocity fluctuations contribute to the near-wall pressure fluctuations, indicated by the conservation of momentum for incompressible flows:

$$\bigtriangledown p = -\rho\left(\frac{\partial \mathbf{u}}{\partial t} + (\mathbf{u}\cdot\bigtriangledown)\,\mathbf{u}\right) + \mu\bigtriangledown^2\mathbf{u} \tag{5.1}$$

The pressure gradient $\bigtriangledown p$ is related to the velocity fluctuations in time and space, in the absence of external forces. Thus, the bursting events in the turbulent boundary layer result in pressure fluctuations that are able to deform the flexible wall, dependent on the material properties of the compliant layer. Reduction in turbulent drag is based on the hypothesis is that a favorable compliant surface is triggered by a pre-bursting event and should thereby impede new burst formations. The suppression of the velocity fluctuations in the turbulent boundary layer then results in a decrease in the present Reynolds stresses by assuming $-\rho\langle(u'+u_c)(v'+v_c)\rangle$, where u_c and v_c represents the wall dynamics in streamwise and wall-normal directions [8].

The response of a compliant surface to the pressure fluctuations in a TBL flow was theoretically examined by Duncan [9] and more recently by Benschop *et al.* [10]. A stable response was directly linked to the pressure pulses that represent the turbulent flow structures in a turbulent boundary layer. However, instability only occurs when the ratio between the dynamic pressure of the flow p_{rms} with respect to the shear modulus of the coating $|G^*|$ reaches a critical value [9]. This critical value depends on a not-well-understood function, including the coating properties, such as the coating damping $\tan(\delta)$, coating thickness h_c and flow Reynolds number Re. The flow-induced surface instabilities (FISI) appear on the coating-fluid interface as a wave-train package moving in the flow direction. Two main FISI-types were classified by Gad-El-Hak *et al.* [11], Gad-el Hak [12] and Carpenter and Garrad [13]:

1) *Static-divergence*: slowly moving waves $U_{wave} < 0.05U_{bulk}$, with very large amplitudes and long wavelengths.
2) *Traveling wave-flutter*: fast moving waves $U_{wave} \sim C_t$, with lower amplitudes and shorter wavelengths. The shear-wave velocity of the compliant material is given by $C_t = (|G^*|/\rho_c)^{1/2}$.

Apart from theoretical examinations, several experimental investigations were performed on the interaction between a turbulent boundary layer flow and a compliant surface [14–23]. Measurements of the instantaneous displacement of the compliant surface in combination with the related wall-bounded velocity field contributes to the understanding of the physics of fluid-surface interaction. Examples of combined measurements are optical holographic interferometry with laser Doppler velocimetry [19] and a laser-based electro-optic transducer with hot-wire measurements [21]. The latter study reports a favorable interaction between a compliant coating and turbulent boundary layer in the sense that it reduces turbulent activities (i.e. Reynolds stresses). Non-intrusive detection techniques are desired to avoid impediment of the surface deformations. Recent developments show the simultaneous use of Mach-Zehnder interferometry in combination with tomographic Particle Image Velocimetry (PIV) [22, 23].

In the present study, the interaction of compliant surfaces with a turbulent boundary layer flow is investigated. The main objectives of this study are to investigate how the compliant wall responds to a turbulent boundary layer and to explore the ability to reduce turbulent skin friction. Three in-house produced compliant coatings with different material properties are applied to explore the interface wave characteristics as a function of the coating properties and the bulk velocity (U_b). The coatings are tested on flat plates in the TU Delft water tunnel [24]. The fluid-surface interaction is quantified by:

- Plate force measurements, in order to determine the skin friction;
- Background Oriented Schlieren (BOS), in order to reconstruct the instantaneous surface deformation field of the coating surface;
- Particle Image Velocimetry (PIV) measurements, in order to measure the streamwise and the wall-normal velocity components u and v of the fluid flow.

Section 5.2 discusses the aforementioned measurements methods. The experimental facility is explained in Section 5.2.1. The coating preparation and characterization are described in Section 5.2.2. The reconstruction method to determine the coating deformation is described in more detail in Section 5.2.3. This method is based on the so-called Free Surface-Synthetic Schlieren (FS-SS) method [25–27], which is derived from the Background Oriented Schlieren (BOS) principle [28, 29] and makes use of the refraction of light rays that distort the background image. The implementation of the PIV system is discussed in Section 5.2.4. The results and the discussion are given in Section 5.3, with the main findings summarized in Section 5.4.

5.2. EXPERIMENTAL SETUP

5.2.1. WATER TUNNEL

The experiments were performed in the cavitation tunnel at the Delft University of Technology that was previously used in the investigations by Foeth [30], Zverkhovskyi [24] and Pennings [31]. Zverkhovskyi [24] adapted and utilized the test section to investigate the drag reducing ability of air cavities. The adapted test section is open at the top, which makes it possible to mount test plates in order to determine the frictional properties of various surfaces via a force balance system. The inlet cross-section area is 300×300 mm^2, while the outlet cross-section area is 300×315 mm^2 due to an inclined bottom wall. The sloped wall largely compensates the boundary layer growth in streamwise direction, such that a nearly constant bulk velocity U_b is maintained. The maximum applied bulk velocity is 5.6 m/s (~500 L/s). The boundary layers at the wall are tripped just before the test section to ensure a turbulent boundary layer at all relevant tunnel velocities. The test plates have a total surface area of 1998×297 mm^2 and have free movement during the force measurements. The gaps around the test plate (approx. 1.0-1.5 mm) are shielded in order to minimize possible flow disturbances. The test section is fully optically accessible, which makes it possible to apply BOS and PIV measurements.

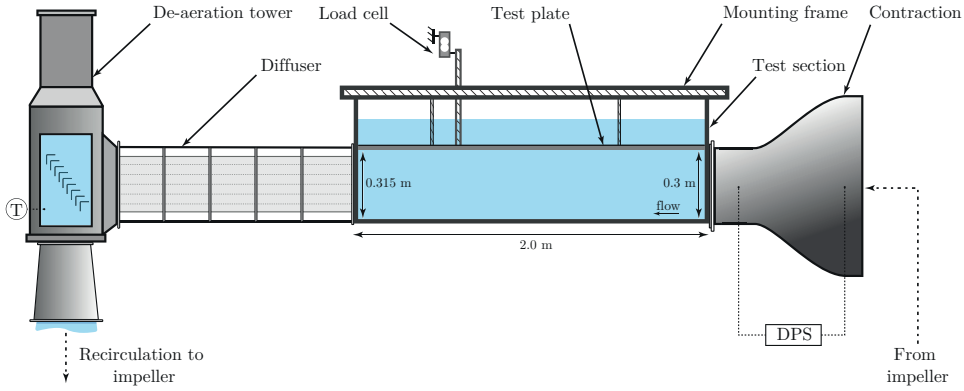

Figure 5.1: Schematic illustration of the water tunnel.

5.2.2. COMPLIANT MATERIAL

MATERIAL CHOICE

Polydimethylsiloxane (PDMS) has conventionally been applied as compliant visco-elastic material in fluid-surface interaction studies [18, 22, 23, 32, 33]. Nevertheless, due to a continuous progress of covalent crosslink reactions between polymer chains, PDMS samples experience an ageing process that modifies the mechanical properties of the material [34, 35]. Due to the ongoing research on the coating-equipped test plates, it was essential to use a visco-elastic material that maintains its mechanical properties over a sufficient period of time.

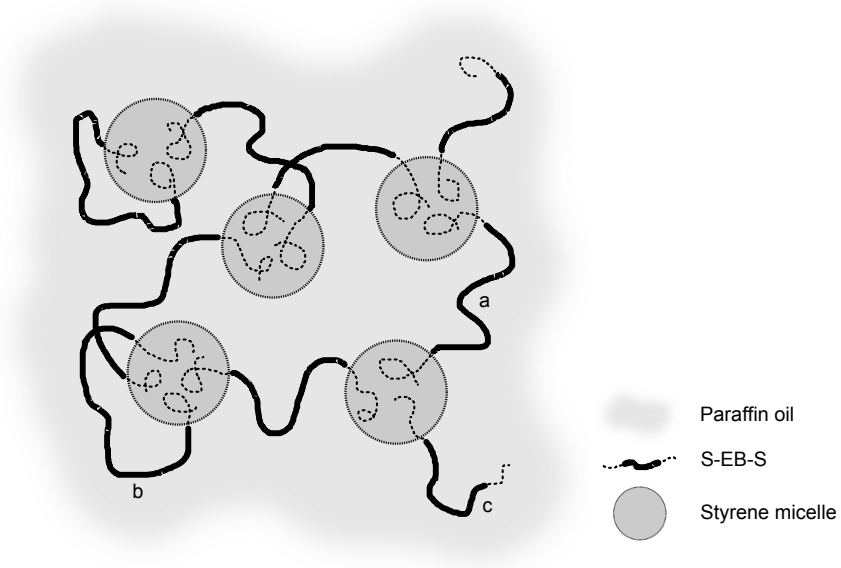

Figure 5.2: SEBS/Oil micelles network formation; (a) bridges: each styrene endblock colonize in a different micelle, (b) loops: each styrene endblock colonize in the same micelle, (c) dangling-ends: one styrene endblocks remains unsettled. Illustration based on Laurer *et al.* [40].

Three compliant coatings were therefore produced in-house from a mixture of triblock-copolymer polystyrene-b-(ethylene-co-butylene)-b-styrene (S-EB-S) and mid-block selective paraffin oil. The styrene end-blocks are thermodynamically incompatible with the paraffin oil and group themselves into micelles to minimise interfacial area, which are considered to be the cross-link points in the material. These points are connected by the ethylene/butylene mid-blocks via physical cross-linking and give formation to a three dimensional network (Fig. 5.2). A higher concentration of S-EB-S increases the micelles and cross-link density, which in part determines the mechanical properties of the visco-elastic material. Other parameters that influence the mechanical properties of the visco-elastic material are the molar mass and the styrene content of the triblock copolymer and the type of applied hydrocarbon oil [36–39].

MATERIAL PREPARATION & CHARACTERIZATION

The polystyrene-b-(ethylene-co-butylene)-b-styrene (SEBS, Kraton G-1650E) with a molar mass of ±100.000 g/mol and styrene content of around 29% was provided by Kraton Polymers. The paraffin oil (Sigma-Aldrich, 18512) was obtained from Sigma-Aldrich and has a dynamic viscosity of 110-230 mPa·s and a density of 0.827-0.89 g/cm^3 at 20^{o}C. The flash point temperature of the paraffin oil is 215^{o}C, which is a point of attention during the material synthesis process.
The coating-equipped test plate has a total surface area of 1998×297 mm^2 with an intended coating thickness of 5 mm, which makes the total volume of the coating around

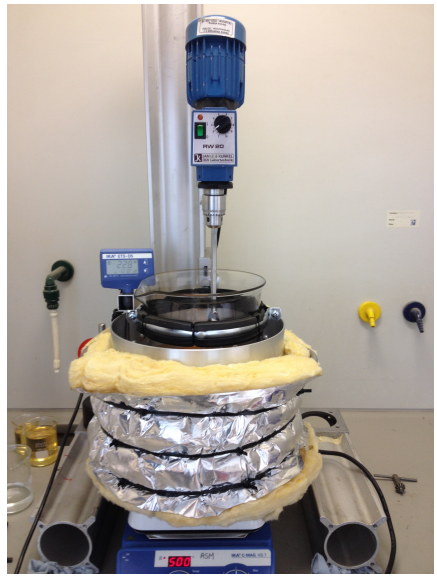

Figure 5.3: Set-up configuration for the coating synthesis. Glass beaker contains the mixture of paraffin oil and SEBS polymer, and is located in an oil bath. The mixture is continuously stirred while heated. The oil bath is placed on a heating plate, which is controlled via a feedback temperature sensor.

3 L (~ 2.6 kg). For each coating composition, sufficient amount of SEBS and paraffin oil was carefully weighed and mixed in a 5L glass beaker at room temperature. The glass beaker was placed in an isolated oil bath, which itself was placed on a heating plate (max. 1000 W, IKA C-MAG HS7) equipped with a temperature feedback sensor (Fig. 5.3). The temperature was raised up to 120^{o}C and maintained for 30 min. The mixture was then mechanically stirred for 3-4 hours at 120-140^{o}C, until a homogeneous transparent solution was obtained. The stirrer was removed and the solution was cooled down to room temperature by natural convection (i.e. without stirring).

The SEBS-concentration determines the material properties of the three coatings (e.g. coating stiffness $|G^*|$). The micelles density is larger when the SEBS-concentration is increased, which results in a higher material stiffness. At room temperature, the three coatings are a rubber-like transparent material. Rheological behaviour measurements were performed using a commercial rheometer (ARES-G2, TA Instruments) with a parallel plate geometry and a diameter of 25 mm. The storage modulus G' and loss modulus G'' at 20^{o}C are measured as a function of strain between 10^{-3} % and 10 % at an angular frequency of 2π rad/s (Fig. 5.4a) and as a function of frequency between 0.1-100 rad/s at 0.5% strain (Fig. 5.4b). The results confirmed the material stiffness increases with increasing SEBS-concentration.

Temperature-sweeping was used to estimate the polymer flow temperature T_m with a temperature increment of 2.5^{o}C/min. The temperature range was 20-150^{o}C, with an angular frequency of 2π rad/s and 0.5% strain (Fig. 5.5). The polymer flow tempera-

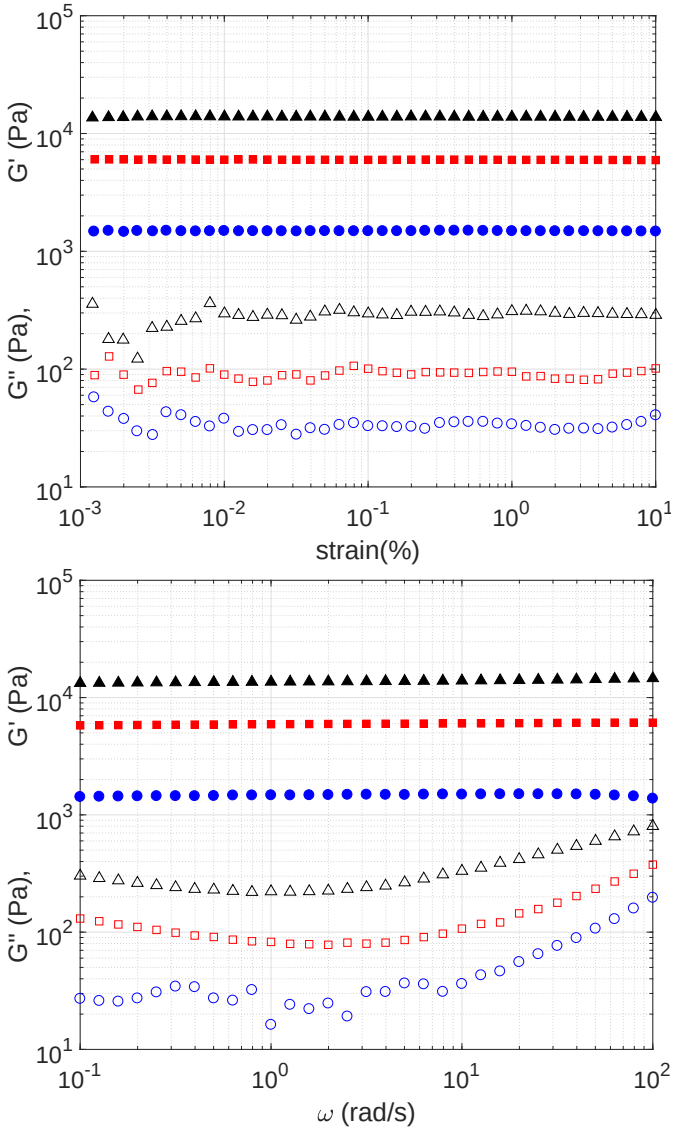

Figure 5.4: Storage modulus G' (closed symbols) and loss modulus G'' (open symbols) of coating 1 (circles), coating 2 (squares) and coating 3 (triangles); as a function of a) strain with an angular frequency of 2π rad/s, and b) angular frequency with 0.5% strain. Coating properties are summarized in Table 5.1.

ture is around 77^{o}C (coating 1), 86^{o}C (coating 2), and 96^{o}C (coating 3). This transition temperature T_m is of great interest for the material post-processing to obtain a homogeneous smooth coating surface on the test plate.

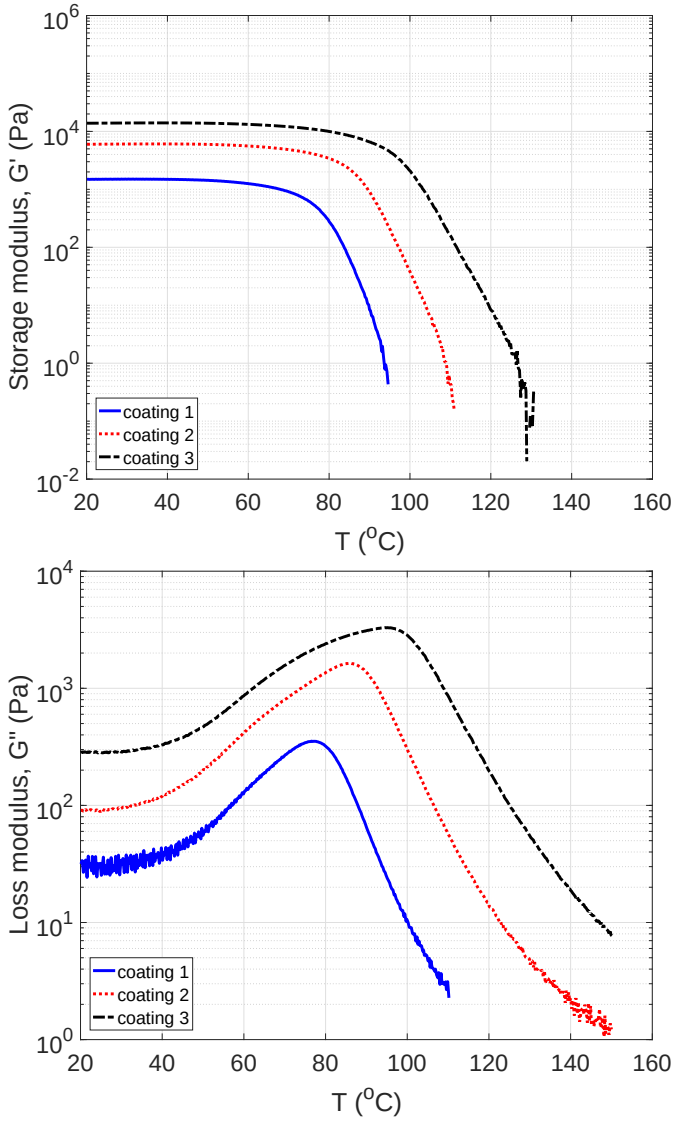

Figure 5.5: a) Storage modulus G' and b) loss modulus G'' of coating 1 (solid line), coating 2 (dotted line) and coating 3 (dot/dashed line) as a function of temperature, with an angular frequency of 2π rad/s and 0.5% strain, all at 20^oC. Coating properties are summarized in Table 5.1.

The surface deformation of the coatings under the turbulent boundary layer flow is determined by Background Oriented Schlieren (BOS) based on the refraction method, described in Section 5.2.3. The refractive index of the coating is required to reconstruct the surface height at the interface. The refractive indices n_i were measured with an Abbe refractometer, which is able to determine the critical angle α_i. Light illumination

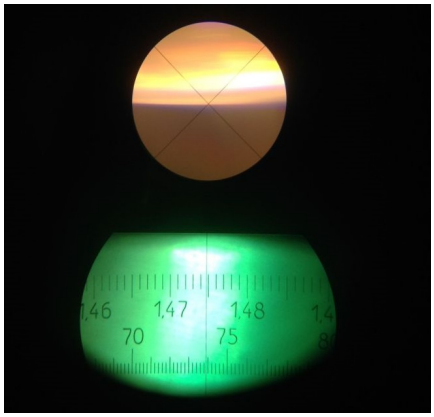

Figure 5.6: Measurement of the refractive index; Boundary line runs through the reticle crosslines (top), Refractive index scale (bottom).

under this critical angle α_i will completely be reflected. The refractive index is given by $n_i = 1/\sin(\alpha_i)$. The working principle of the refractometer is validated using distilled water ($n_w = 1.333$) and glass calibration sample ($n_{test} = 1.5165$) at room temperature (20^oC). Figure 5.6 shows an example of the measurement of coating 1. The dark/light boundary line needs to cross the reticle crosslines to obtain the refractive index, in this case $n_{c_1} = 1.475$.

COATING PROCESSING

Standard test plates in the water tunnel are manufactured from plexiglas (PMMA), which has a glass transition temperature of $T_g = 110^oC$. This is in the range of the polymer flow temperature of the coatings. Therefore, the coatings were applied on a 10 mm thick flat polycarbonate plates, which has a glass transition temperature of $T_g = 147^oC$. The polycarbonate plate was leveled with high precision inside a large oven. At room temperature, pieces of the visco-elastic material (~ 2.6 kg) were deposited on the plate that was constructed with an additional raised edge of 5 mm (Fig. 5.7a). The temperature was increased by 10^oC above the polymer flow temperature of the specific material under slow heating to avoid thermal stresses ($+2^oC$/min). The oven temperature was maintained for 2 hours, such that the material could spread out over the entire plate as a very viscous liquid. After slowly cooling to room temperature (-1^oC/min), the result is a transparent coating layer with a homogeneous coating thickness of 5 mm (Fig. 5.7b).

Table 5.1 summarizes the measured material properties within this study. The frequency-averaged storage modulus G' and loss modulus G'' determine the complex shear modulus $G^* = G' + iG''$ with $|G^*| = \sqrt{(G')^2 + (G'')^2}$, which is used to calculate the shear-wave propagation velocities $C_t = (|G^*|/\rho_c)^{1/2}$ [5]. The shear wave velocities C_t are within the range of the flow velocities of the water tunnel and flow-induced surface instabilities (FISI) can be expected. The material is considered to be incompressible within the range of operation (i.e bulk modulus $K \sim 5$ GPa), which presumes a Poisson's ratio of $\sigma \simeq 0.5$.

Figure 5.7: Pre- and post-heating of the coating material a) Pieces of coating material on a constructed polycarbonate plate, and b) Smooth coating layer with a homogeneous thickness, in the order of ~5 mm.

Table 5.1: Material properties of the three compliant coatings at standard conditions.

	$SEBS$ (w%)	G' (kPa)	G'' (kPa)	ρ_c (kg/m^3)	C_t (m/s)	T_m (^{o}C)	n (-)
coating 1	4.8	1.5	0.05	862	1.31	77	1.475
coating 2	7.8	6.0	0.13	864	2.63	86	1.475
coating 3	11.9	13.9	0.35	866	4.01	96	1.475

5.2.3. SURFACE DEFORMATION MEASUREMENTS

The instantaneous deformation field $\zeta(x, y, t)$ of the compliant surface was measured via the Free Surface-Synthetic Schlieren (FS-SS) method [25], which is a non-intrusive optical detection techniques that is based on the Background Oriented Schlieren (BOS) principle [28, 29]. A random dot pattern was placed behind the coating-fluid interface and was back-illuminated by a homogeneous LED-screen to obtain a high contrast. The dot pattern was front-observed by a high-speed 4Mpx-camera via a mirror, which was placed below the water tunnel (Fig. 5.8).

The distorted image of the reference dot pattern is the result of light rays passing through the deformed compliant surface. The apparent local displacement of the reference image is directly proportional to the local surface gradient [41]. The displacement field was computed via an in-house Digital Image Correlation (DIC) algorithm, where groups of dots inside a small interrogation window are correlated in order to obtain the local displacement. DIC algorithms have demonstrated to be accurate and robust for PIV measurements [42, 43]. A multi-pass correlation was used with a final interrogation window of 16×16 pixels with a 50% overlap. A simple median filter method was applied to detect spurious vectors that were replaced by linear interpolation [44]. The

reconstruction of the surface interface will be discussed in the next subsection.
The refraction method has to fulfill at least two requirements for a reliable reconstruction of the surface deformation. First, the camera-pattern distance H needs to be large enough compared to the field size L to meet the *paraxial approximation*. In the present case, the field of view had an area of 100×100 mm^2 in the center of the plate and the camera-pattern distance was around $H = 1400$ mm thereby satisfying the paraxial approximation, i.e. $\beta \simeq L/\left(\sqrt{2}H\right) \ll 1$. Second, the wave amplitude and surface curvature need to be small to fulfill the *linear approximation*. The DIC algorithm is inferior when strong surface deformations occur; strong strained refracted patterns or dots that move in opposite direction within one interrogation window will result in bad displacement vectors. A Dot Tracking Algorithm (DTA) would be more appropriate when strong deformations occur [45]. The pattern-surface distance was minimal at 15 mm ($= h_c + h_p$) and could be adjusted by inserting glass spacer plates of various thicknesses $h_g = 2$, 10 or 20 mm; an increase in pattern-surface distance amplifies the deformations and with that the resolution. However, this may also lead to ray crossing in regions of large strain resulting in inaccurate displacement values, which avoids an unambiguous reconstruction of the coating surface (Fig. 5.9).

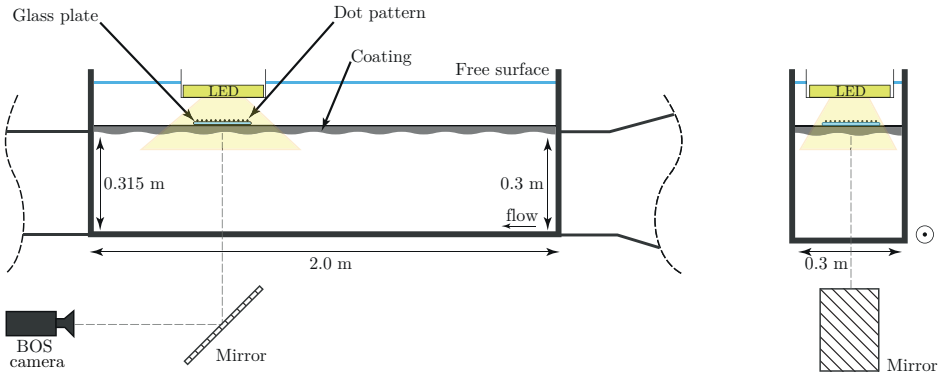

Figure 5.8: Background-Oriented Schlieren (BOS) set-up in order to perform surface deformation measurements. The camera observes the random dot pattern via a mirror and the transparant coating material. The total distance between the camera and the dot pattern is $H = 1400$ mm. The flow moves from right to left.

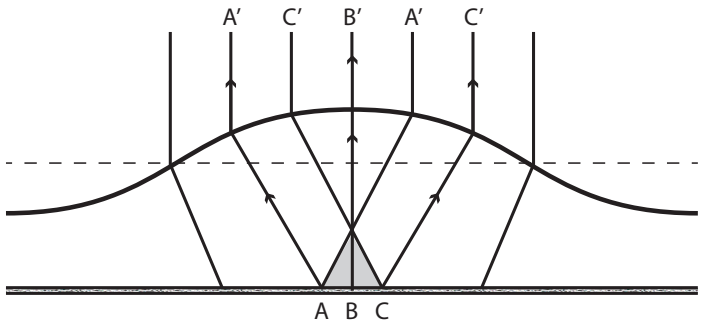

Figure 5.9: Ray crossing, due to large surface curvature and/or large dot pattern-surface distance (Eq. (5.3)). In this ray crossing example, the dot pattern markers A-B-C are observed as A'-C'-B'-A'-C'. Illustration based on Moisy *et al.* [25].

A number of 2000 successive images were taken with a fixed sampling frequency F_s of 1200 Hz for coating 1 with a glass spacer plate $h_g = 2$ mm. For the other measurements, the sampling frequency F_s was linearly increased with the bulk velocity U_b, namely from $F_s = 200$ Hz at $U_b = 0.87$ m/s to $F_s = 1240$ Hz at $U_b = 5.39$ m/s. A summary of the measurement parameters is given in Table 5.2.

Table 5.2: Parameters of the BOS measurements. Glass spacer plate h_g, image sampling frequency F_s, water tunnel bulk velocity U_b.

	h_g (mm)	F_s (Hz)	U_b (m/s)
coating 1	2	1200	0.87 – 5.39
	10	200 – 1240	0.87 – 5.22
	20	200 – 1240	0.87 – 5.22
coating 2	20	200 – 1240	0.87 – 5.39
coating 3	20	200 – 1240	0.87 – 5.22

RECONSTRUCTION METHOD

The surface reconstruction method is based on the work by Moisy *et al.* [25]. The slope of the coating surface $\nabla\zeta$ is considered to be proportional to the measured displacement field $\delta\mathbf{r}(x,y)$ of the refracted image, following:

$$\nabla\zeta = (1/H - 1/(\alpha \cdot h_d)) \cdot \delta\mathbf{r}(x,y) \tag{5.2}$$

The paraxial approximation represents a large camera-pattern distance H and eliminates $1/H$ in Equation 5.2. Parameter α accounts for the refraction of rays through the deformed surface surface, i.e. $\alpha = 1 - (n_w/n_c)$, with n_w and n_c as the refractive indices of the water and the coating, respectively. The effective dot pattern-surface distance h_d is the sum of the thicknesses of the layers weighted by the refractive index ratio:

$$h_d = h_c + (n_c/n_p) \cdot h_p + (n_c/n_g) \cdot h_g \tag{5.3}$$

where subscripts c, p and g are for coating, polycarbonate and glass spacer, respectively. The spatially averaged displacement field $\overline{\delta\mathbf{r}}$ is subtracted from the measured displacement field $\delta\mathbf{r}$ in order to correct for small vibrations of the experimental setup. The mean surface height is set to zero (i.e. $\overline{\zeta} = 0$) and is used as an integration constant to obtain a complete surface reconstruction. An example of a refracted image is displayed in Figure 5.10a. The figure displays a section (300px × 300px) of the total refracted image (2016px × 2016px), which is recorded at a bulk velocity of $U_b = 4.9$ m/s, with the fluid flow from top to bottom of the image. The deformation of the surface is visible by the stretching and compression of the dot images of the reference pattern. Particularly, the deformation is mainly in the flow direction and suggests that waves are present with their crests perpendicular to the flow. In Figure 5.10b, the computed displacement field $\delta\mathbf{r}(x,y)$ of the refracted image is plotted on top of the reconstructed

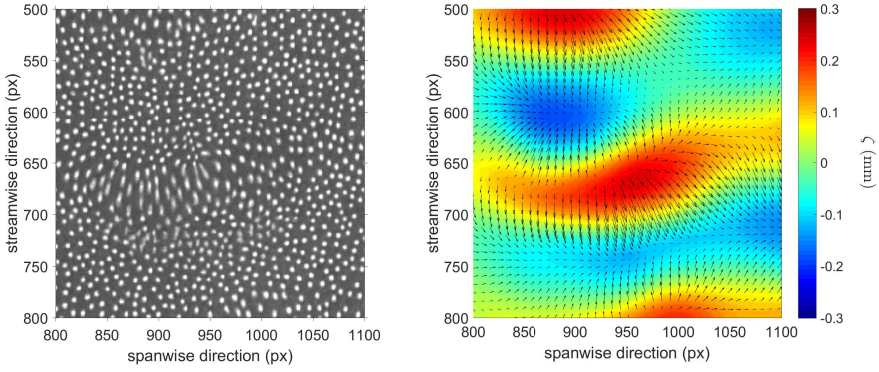

Figure 5.10: A representative image and the processed data, where 300 px equals 16 mm. a) Random image of a deformed dot-pattern. b) Computed displacement vector field (arrows) and reconstructed surface height field (color).

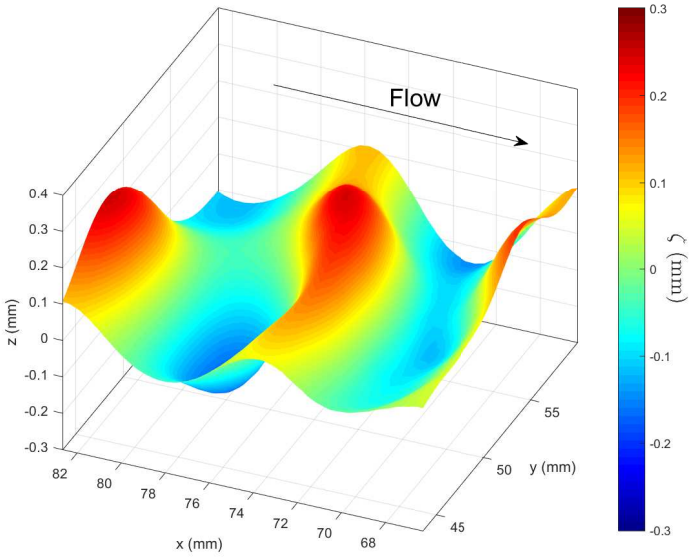

Figure 5.11: The 3D representation of the coating surface corresponding to the example in Figure 5.10.

surface height field $\zeta(x, y)$. The arrows of the displacement field diverge at a crest and converge at a valley and confirms the integration method. The corresponding 3D representation of the coating surface is shown in Figure 5.11.

5.2.4. FLOW VELOCITY MEASUREMENTS

Particle Image Velocimetry (PIV) was used to study the instantaneous velocity fields and turbulent statistics of the turbulent flow. A standard 2D-2C PIV configuration was applied to the test facility, as is displayed in Figure 5.12. The field of view (FOV) is around 8.7×7.0 mm^2 in streamwise and wall-normal direction respectively and was situated 1.7 m downstream from the entrance of the test section. The FOV was illuminated by a light sheet ($\Delta z_0 < 1$ mm) using a double-pulsed 50 mW Nd:YAG laser (Litron L-class 50-50) and was located in the center of the tunnel. The images were recorded by a 1280×1024 pixel CCD-camera (FlowMaster, LaVision) and show a part of the wall and the near-wall flow region. Hollow glass particles (Sphericell, $d_p = 10\mu$m) were used as tracers, with a given particle density of approximately $\rho_d = 1.1 \times 10^3$ kg/m^3. The response time scale of particle relaxation $\tau_p = d_p^2 \rho_p / (18\rho_f \nu)$ was 5.6 μs. The particles are expected to follow the flow even in the near-wall regime as the expected inner turbulence time-scale $\tau_\nu = \nu / u_\tau^2$ is minimally >20 μs, where ν is the kinematic viscosity (m^2/s) and u_τ is the friction velocity (m/s). Calibration is done using a calibration grid with dot-spacing of 0.5 mm. The pixel size is determined to be 6.7 μm, resulting in a $M_0 = 1$ magnification.

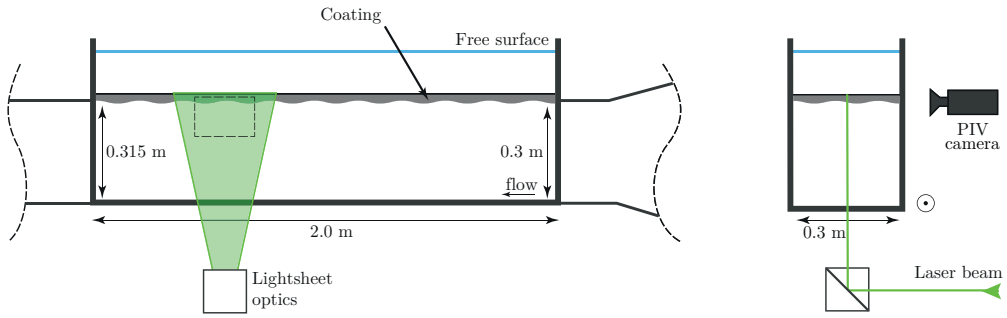

Figure 5.12: Illustration of the experimental PIV set-up applied to the test section of the facility. The field-of-view is located at 1.7 m downstream from the entrance of the test section and at the centerline of the water tunnel. The flow moves from right to left.

A total amount of 500 successive PIV image pairs were taken at a low frequency (3-4 Hz) to ensure reliable statistical convergence of the mean velocity field and turbulent parameters. The time delay Δt between the first and second image is chosen such that the particle displacement between the two images is around 8-10 pixels far-away from the wall. Data analysis was performed using a commercial software (DaVis v7, LaVison). A multi-pass correlation was used, with a final interrogation window size of 64×64 pixels with a 75% overlap resulting in a vector spacing of 0.11 mm. The final 64×64 pixels window was the minimum size to satisfy the criterion of 5 particles per interrogation window. Close to the wall, the velocity profiles show relatively low spatial resolution due to the large interrogation window. The corresponding vector spacing is $7-20$ wall-units (y^+) for bulk velocities $U_b = 1.7-5.2$ m/s, respectively. The reconstruction of the velocity profile closer to the wall requires a higher spatial resolution and can be obtained with advanced correlation algorithms. Particle Tracking Velocimetry (PTV) was used to determine the displacement of individual particles close to the wall ($y < 1$ mm) and enhances the spatial resolution of the mean velocity profile up to 1 pixel ($\sim 0.5-1.5$ y^+), by means of the so-called *super-resolution* method [46]. First, an in-house PIV correlation algorithm with elongated interrogation windows (~64px×32px, 50% overlap) is used that provides similar results as the earlier used commercial software. Second, the measured estimate of the local velocity field is used as an input for the PTV processing, which improves the successful and fast detection of particle pairs as it substantially reduces the search area. In the end, the particle displacement Δx_p between two successive images (with Δt) results in the velocity of all individual particles. The particle velocities are averaged with respect to the mean position of the compliant wall to obtain the mean velocity profile.

5.3. RESULTS & DISCUSSION

5.3.1. FRICTION FORCE MEASUREMENTS

The coatings on the plate have a homogeneous thickness with a very smooth surface due to the liquifying and re-solidifying process. Atomic force microscopy (AFM) was used to quantify the surface roughness parameters, and indicated a roughness average R_a =0.489 nm, a root-mean-square R_q =0.655 nm, a maximum valley depth R_v =-5.865 nm and a maximum peak height R_p =6.593 nm. The measured force $\bar{F}$ represents the averaged shear stress $\bar{\tau}$ times the total test plate area A, such that $\bar{\tau} = \bar{F}/A$. The averaged shear stress $\bar{\tau}$ is plotted against the bulk velocity U_b and was highly reproducible (Fig. 5.13). The results are compared with two common smooth-surface curves, namely the Grigson and the Prandtl-Schlichting correlation curves (also see Chapter 4.3.1). For low bulk velocities, the friction values of all three coatings are similar to those of a rigid smooth surface. Above a bulk velocity of 4.5 m/s, the shear stress of coating 1 deviates increasingly with the bulk velocity U_b; for example, the shear stress $\bar{\tau}$ has a +40% increase at $\bar{U}_b$ = 5.5 m/s. Coating 2 & 3 maintain their smooth surface behaviour up to the maximum available tunnel velocity of ~5.6 m/s.

The coatings are considered to be highly sensitive to pressure forces, with coating 1 being the most sensitive due to its low shear modulus $|G^*|$. For coating 1, the flat-plate friction diagram in Figure 5.14 shows the transition when the surface roughness k_s relative to the plate length L increases. Up till $Re_L = 9 \times 10^6$ ($U_b \sim$ 4.5 m/s), coating 1 follows the “hydrodynamic smooth”-line, while for higher Reynolds numbers the drag coefficient C_d sharply increases. The transition in roughness is presumably the result of flow-induced-surface-instability (FISI) waves with significant amplitudes. It should be noted that the current surface roughness k_s is based on the equivalent sandgrain roughness of Nikuradse [47] with the corresponding transition regime. The inflection (or 'dip') of the friction-curve is the main discrepancy with the traditional Moody-diagram, which shows a monotonic change of friction-values with increasing Reynolds number Re_L [48]. The drag coefficients above U_b =4.5 m/s are used to estimate the surface roughness k_s of the deformed coating by means of interpolation. The apparent surface roughness of the coating surface is shown in Figure 5.15, together with the estimated viscous sublayer thickness δ_v. A surface is considered to be hydrodynamic smooth when the surface roughness is smaller than the viscous sublayer $k_s < \delta_v$. Beyond the transition velocity U_b = 4.5 m/s, the "dynamic" effective roughness of the wavy surface grows quickly from k_s =40 μm to 130 μm, which corresponds to k_s^+ =6 to 27.

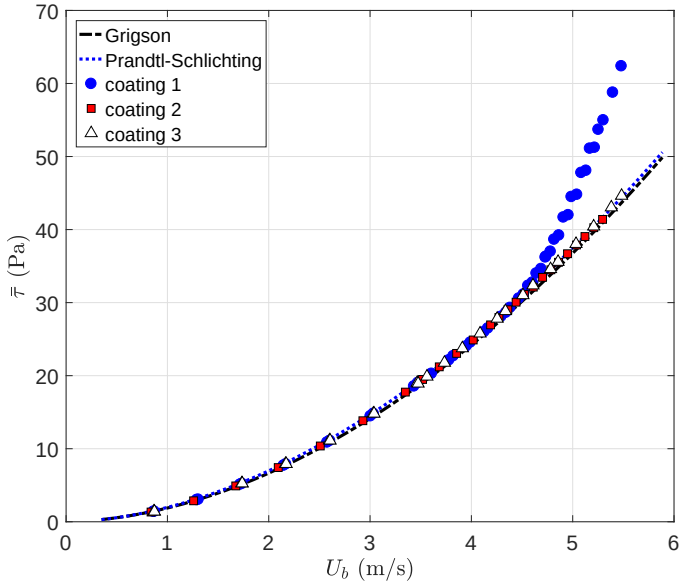

Figure 5.13: Shear stress $\bar{\tau}$ as a function of watertunnel bulk velocity U_b. Coating 1 (see Table 5.1) deviates from the estimated correlation lines of Grigson and Prandtl-Schlichting at $U_b = 4.5$ m/s and above.

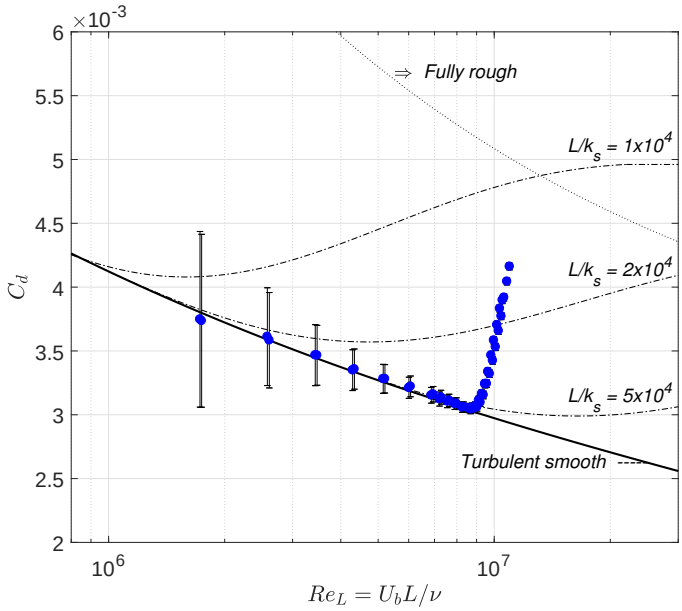

Figure 5.14: Drag coefficient C_d of coating 1 versus Reynolds number Re_L. Transition to a 'rough' surface from $Re_L = 9 \times 10^6$ and above. The friction lines are reproduced from [49].

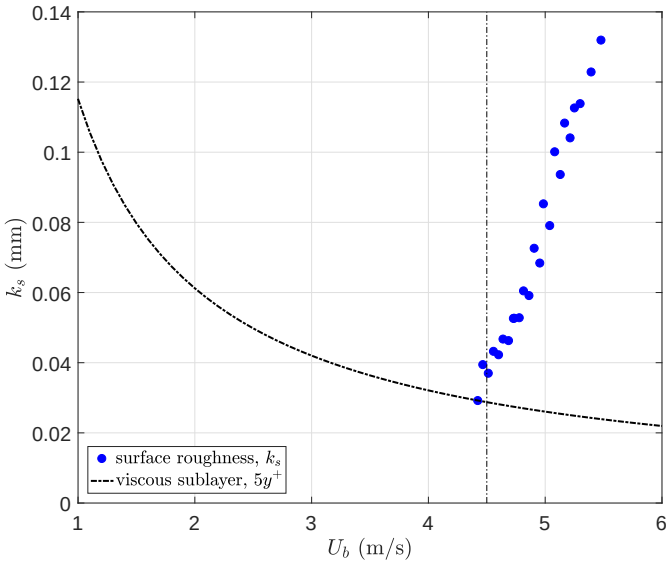

Figure 5.15: Estimated surface roughness k_s related to the measured drag coefficient C_d. The dot/dashed line represents the viscous sublayer thickness $\delta_v = 5\nu/u_\tau$, based on Grigson's correlation.

5.3.2. SURFACE RECONSTRUCTION

GLOBAL RESULTS AND DEFORMATION SCALING

Coating 1 is considered to be hydraulically "smooth" up to the bulk velocity U_b = 4.5 m/s, while coating 2 & 3 are "smooth" up to the maximum available tunnel velocity. The 2000 consecutive height fields $\zeta(x, y, t)$ were used to analyze the interaction of the turbulent boundary layer with the three compliant coatings. Figure 5.16 shows the distribution of the fluctuating surface height ζ for a bulk velocity U_b = 4.35 m/s over 2000 height fields. Compared to a normal distribution with an identical standard deviation of ζ_{rms} = 0.0123 mm, the surface height measurement data followed a double exponential distribution exhibiting a strong peak and long tails with a skewness of -0.064 and a kurtosis of 4.26.

For all the three coatings, the root-mean-square values of the surface height ζ_{rms} increased with the increasing bulk velocity U_b (Fig. 5.17a). For coating 1, an obvious sharp transition was observed around bulk velocity U_b = 4.5 m/s, beyond which the rms-values grow considerably faster. This supports the argumentation that the frictional increase above U_b > 4.5 m/s, as observed in the force measurements, is caused by an increase in the surface roughness, which may be related to growing waves with significant amplitudes.

Several authors have pointed to the dominant near-wall flow structures to cause pressure fluctuation in the turbulent boundary layer [6, 7, 50]. On their turn, these pressure fluctuation can deform the compliant surface of the wall. The deformation of the present three compliant coatings was also shown analytically using the one-way coupling approach [10]. Potential scaling parameters are the pressure fluctuations p_{rms}

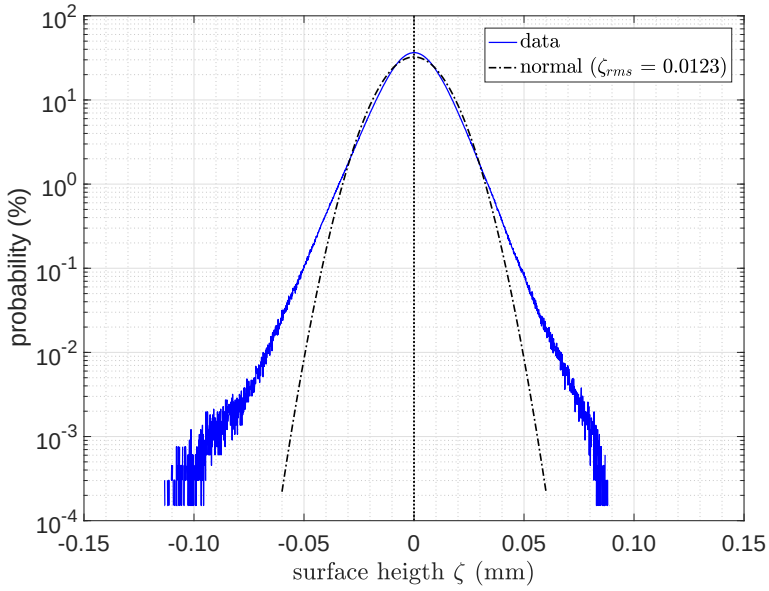

Figure 5.16: Distribution of the fluctuating surface height ζ of coating 1 at a bulk velocity U_b = 4.35 m/s. Statistics: ζ_{rms} = 0.0123 mm, skewness of -0.064, and kurtosis of 4.26.

and the coating shear modulus $|G^*|$ (i.e. coating stiffness), while the contribution of the shear stress fluctuation to the vertical displacement proved to be marginal. The surface-pressure fluctuation p_{rms} was estimated, based on the empirical model of the pressure spectrum by Goody [51, 52]. The emperical relation of the surface-pressure fluctuations p_{rms} is given by [10]:

$$\frac{p_{rms}^2}{\tau_w^2} = 0.0309 + 0.745(\ln(R_T))^2 \tag{5.4}$$

with τ_w as the wall shear stress and R_T as the ratio of the outer-layer-to-inner-layer time-scales, $R_T = (\delta_{99}/U_b)/(\nu/u_\tau^2)$. The scaled results show that the vertical displacement of all coatings collapse on a single line in the one-way coupled regime (Fig. 5.17b). This indicates that the turbulent flow and the related surface-pressure fluctuations p_{rms} deform the compliant coating in proportion to the inverse of the coating stiffness. The surface deformations have negligible effect on the turbulent flow and is therefore called a one-way coupled regime. Beyond $p_{rms}/|G^*| > 0.085$, coating 1 deviates from the scaling line and this is suggested to be a two-way coupled regime of coating 1, where the surface deformation influences the turbulent flow as well. For coating 2, the transition towards a two-way coupled regime seems to be around $p_{rms}/|G^*| \sim 0.03$, although this is still a premature conclusion due to insufficient amount of data in this regime.

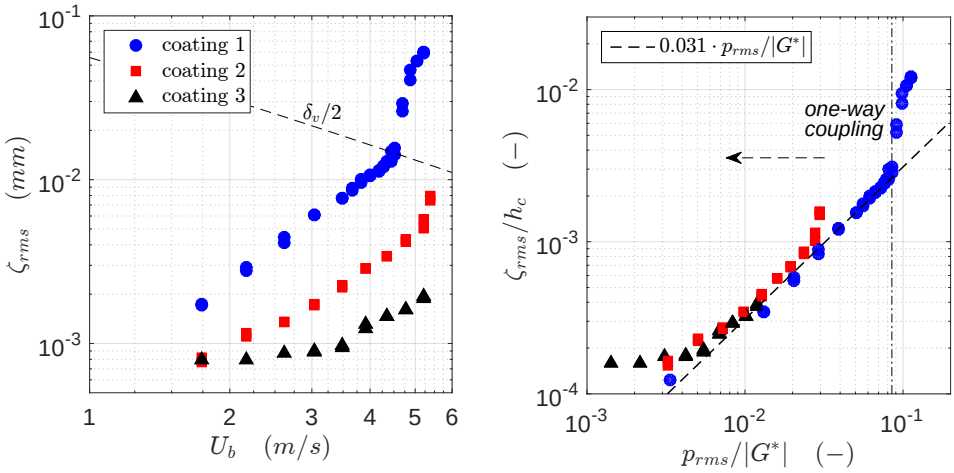

Figure 5.17: Vertical displacement of coating 1,2 & 3: a) Root-mean-square values ζ_{rms} as a function of the bulk velocity U_b. The estimated 1-way/2-way regime transition of coating 1 occures when the surface deformation is around $\zeta_{rms} > \delta_v/2$. b) scaled RMS-values ζ_{rms} to coating thickness h_c in relation to the scaled pressure fluctuations p_{rms} to coating shear modulus $|G^*|$. The scaling-factor 0.031 of the one-way coupled regime is a fit parameter which contains unknown factors, as discussed by Benschop *et al.* [10].

5

QUALITY ASSESSMENT

A solid reconstruction of the surface height depends, among others, on the maximum acceptable image strain or image deformation of the refracted image. Short waves with high wave amplitudes give large surface slopes, which results in regions with large image strain (~ excessive extension/compression of dots) and may exceed the linear approximation to obtain an accurate measurement of the displacement field. The two local strain components $\sigma_x(x,y) = \partial r_x(x,y)/\partial x$ and $\sigma_y(x,y) = \partial r_y(x,y)/\partial y$ are used to quantify the quality of the surface reconstruction [25]:

$$\sigma_{rms} = \sqrt{\frac{1}{N_x N_y} \sum_{x,y} max\left(|\sigma_x(x,y)|, |\sigma_y(x,y)|\right)^2} \tag{5.5}$$

where N_x and N_y are the number of displacement vectors in the x- and y-directionS, respectively. When the rms of the image strain is lower than $\sigma_{rms} < 0.15$, the surface reconstruction is considered to be reliable. Nevertheless, very low rms-values of σ_{rms} provides low resolution of the displacement field and results in a noisy gradient field. Figure 5.18 displays the image strain rms-values of the surface deformation corresponding to the results of Figure 5.17. The rms-values are quite low ($\sigma_{rms} \sim 0.01$) for the low bulk velocities $U_b < 2$ m/s. Coating 1 shows a rapid growth ($U_b > 4.5$ m/s) exceeding the desirable values with increasing bulk velocity U_b, which indicates excessive extension/compression of dots, related to steep undulations on the surface. Stiffer coatings 2 and 3 have substantial lower image strain rms-values σ_{rms} at high bulk velocities U_b, such that the selection of larger 'optical magnifiers' ($h_g > 20$ mm) would have in-

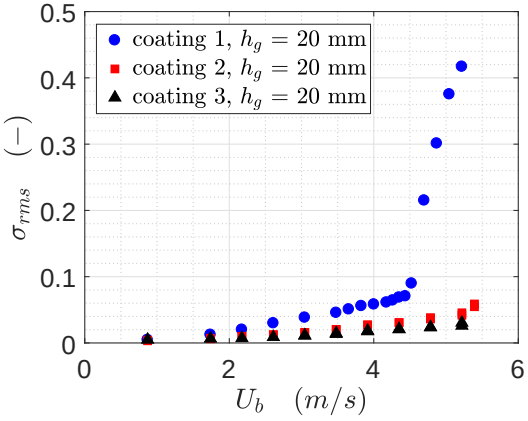

Figure 5.18: Image strain σ_{rms} of coating 1, 2 and 3 with glass spacer heights h_g = 20 mm.

creased the resolution of the displacement field $\delta\mathbf{r}(x, y)$.
A more detailed investigation of the robustness and repeatability of the results was done using three different glass spacer heights (h_g = 2, 10 & 20 mm) for the surface deformation measurements of coating 1. Figure 5.19a shows similar ζ_{rms}-values for all the three glass plates. Large image strain occurs when the glass thickness h_g is increased, which has been verified by the image strain rms-values σ_{rms} (Fig. 5.19b). Very large image strain leads to under-estimation of the actual wave/surface heights, as was demonstrated by Moisy *et al.* [25]. Even though the image strain of the deformed images of coating 1 exceeds the desirable rms-value $\sigma_{rms} < 0.15$, the surface reconstruction are considered to be reasonably as identical results were obtained from the analysis of the coating-fluid interface in the PIV images (see section 5.3.6).

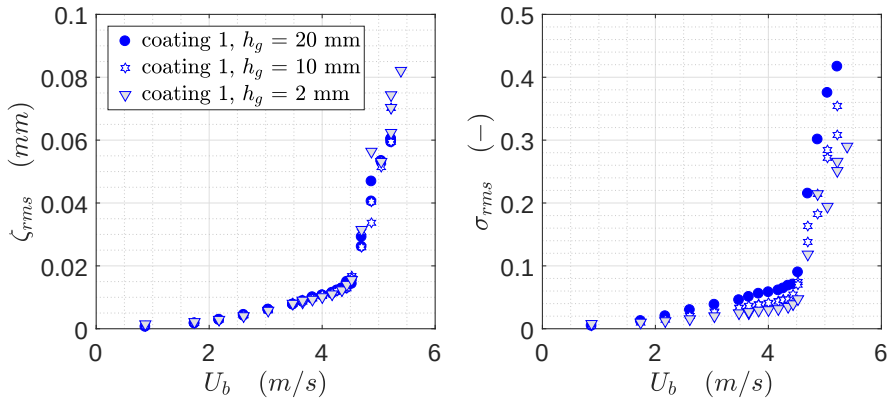

Figure 5.19: a) Surface fluctuation ζ_{rms} and b) image strain σ_{rms} of coating 1 as a function of bulk velocity U_b, with glass spacer heights h_g =2, 10 and 20 mm.

Overall, the global results show that coating 1 experiences an extraordinary interaction with the turbulent boundary layer compared to coatings 2 & 3. First, the absolute vertical surface displacement ζ is significantly larger at a low bulk velocity ($U_b < 4.5$ m/s), owing to the coating softness ($\sim 1/G^*$). Second, coating 1 deals with a transition from which the waves grow exceptionally with increasing bulk velocity U_b, resulting in an unusual 'dynamic' surface roughness. For these reasons, coating 1 has been selected for further consideration within this study to analyse the interaction between fluid flow and compliant surface.

5.3.3. SURFACE PATTERN DEPENDENCY ON THE FLUID VELOCITY

Figure 5.20 presents six instantaneous height fields $\zeta(x, y, t)$ of coating 1 with increasing bulk velocity U_b. At low bulk velocities $U_b < 4.5$ m/s, the surface deformations exhibit randomly oriented patterns (Fig. 5.20a). The time series show that the deformations move in the same direction as the fluid flow (from left to right). Positive surface undulations (crests) $\zeta_c > 0$ are usually preceded and/or succeeded by comparably dimensioned valleys $\zeta_v < 0$ and is attributed to the incompressibility of the coating material. When the bulk velocity U_b increases, the wave pattern shows a similar shape but with increasing wave amplitudes (Fig. 5.20b). At the transition velocity $U_b = 4.5$ m/s, this pattern is maintained in combination with incidentally appearing slender wave trains with larger amplitudes ($\pm$ 100 μm), where the wave crest is oriented in spanwise direction (Fig. 5.20c). Beyond the transition velocity $U_b > 4.5$ m/s, the surface deformations grow considerable larger than before and the wave trains now dominate the surface height field (Fig. 5.20d-5.20f). The time series of the surface height fields $\zeta(x, y, t)$ show that the wave trains are occasionally overtaken by waves with smaller amplitudes. This indicates that two types of waves are traveling in streamwise direction on the fluid-surface interface with different wave dynamics.

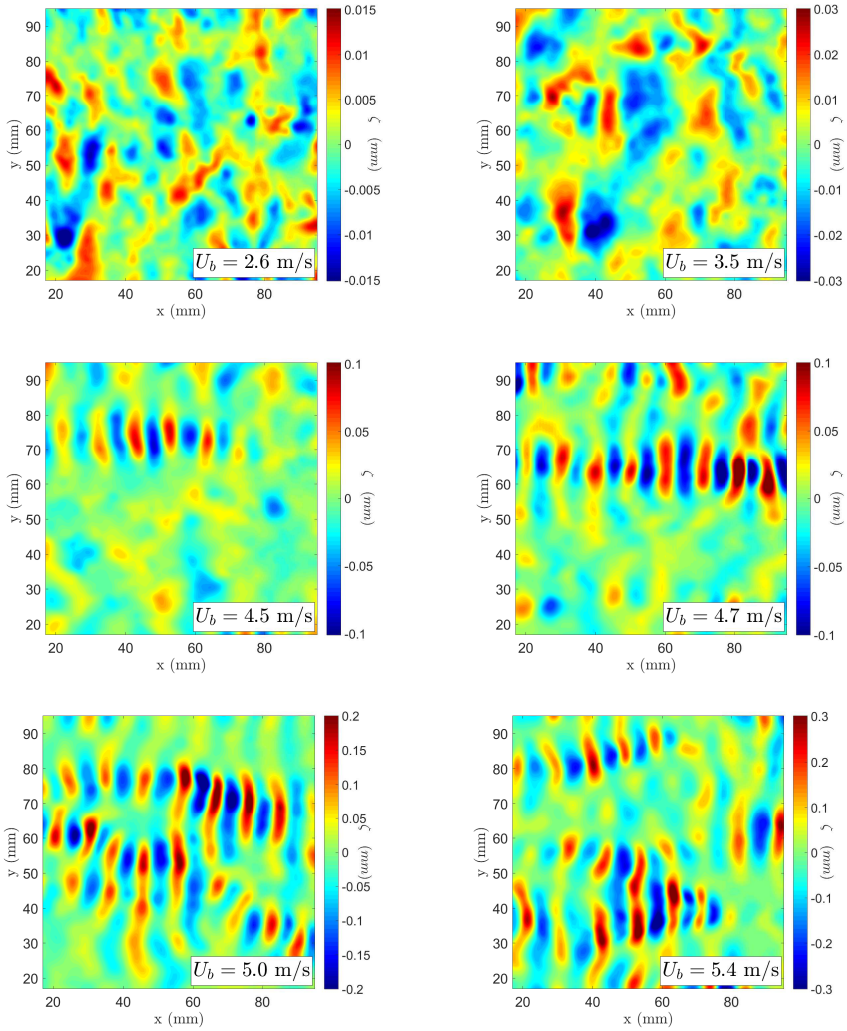

Figure 5.20: Instantaneous surface height fields $\zeta(x, y)$ at increasing bulk velocity U_b.

SURFACE SHAPE AND AMPLITUDE

The half-wave lengths and wave maxima/minima are obtained by a series of two consecutive zero-crossings and the corresponding local maximum (wave crest) or minimum (wave valley) in between. An example of the analysis is given in Figure 5.21. The mean wave characteristics related to the bulk velocity U_b are summarized in Table 5.3. The mean wave characteristics show that the undulations have a symmetric shape for all the studied bulk velocities up to a transition at $U_b = 4.5$ m/s; the length and the height of the crests ($\bar{l}_c$ and $\bar{\zeta}_c$) have similar dimensions as the valleys ($\bar{l}_v$ and $\bar{\zeta}_v$).

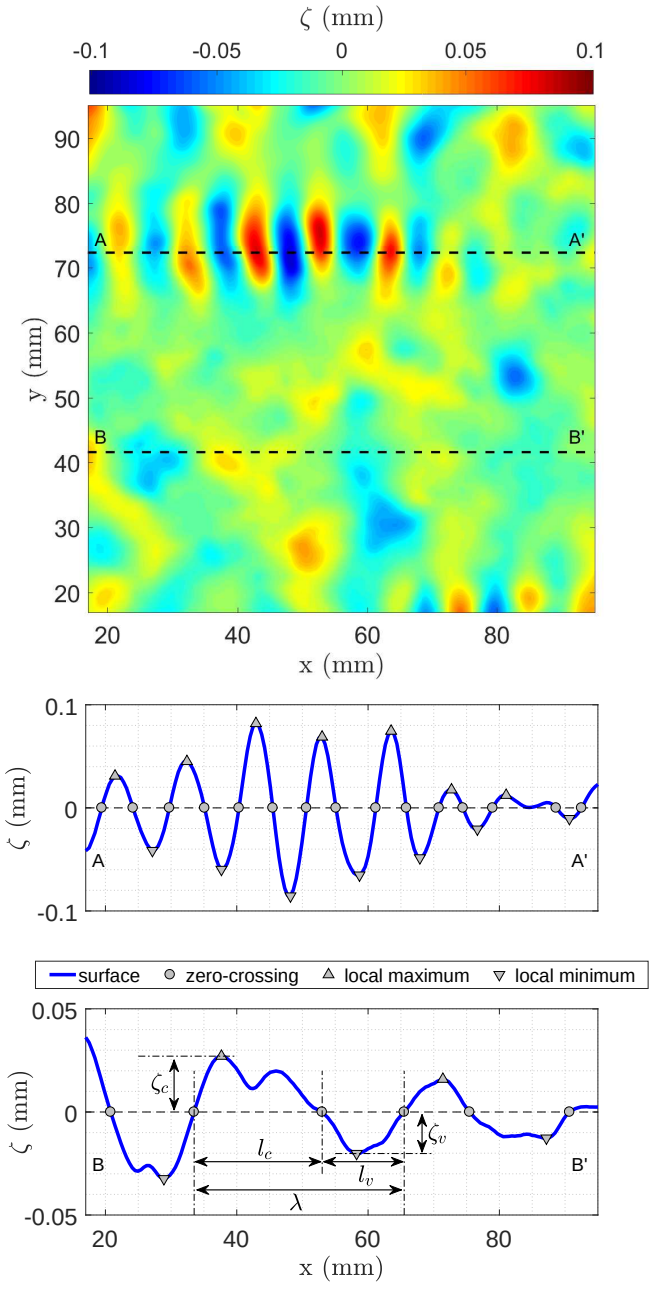

Figure 5.21: Example of wave analysis. a) Surface deformation field $\zeta(x, y)$ with cross-section lines *AA'* and *BB'*. b) Surface cross-section *AA'* and *BB'*, with the surface zero-crossings and the local minimum and maximum.

In the regime after the transition ($U_b > 4.5$ m/s), the wave values in Table 5.3 contain the wave characteristics of two different types of waves traveling on the surface interface, as was previously observed in the time series of the surface wave heights $\zeta(x, y, t)$. The values are therefore an average of the long waves with small amplitudes and short waves with large amplitudes. The waves, nevertheless, becoming increasingly asymmetric with increasing bulk velocity U_b; the crests being higher and shorter than the valleys, i.e. $\bar{\zeta}_c > |\bar{\zeta}_v|$ and $\bar{l}_c < \bar{l}_v$. This also results in a difference in the local wave steepness of the crest $\overline{\zeta_c/l_c}$ and the valley $\overline{\zeta_v/l_v}$; the slope of the crest being significantly steeper than the slope of the valley.

Table 5.3: Mean wave characteristics of coating 1.

U_b (m/s)	Re_L $\times 10^6$	$\bar{l}_c$ (mm)	$\bar{l}_v$ (mm)	$\bar{\lambda}$ (mm)	$\bar{\zeta}_c$ (μm)	$\bar{\zeta}_v$ (μm)	$\lvert\bar{\zeta}_v\rvert/\bar{\zeta}_c$ (-)	$\overline{\zeta_c/l_c}$ $\times 10^4$	$\overline{\zeta_v/l_v}$ $\times 10^4$
0.9	1.7	6.60	6.68	13.27	0.9	-1.0	1.11	2	-2
1.7	3.5	6.88	6.77	13.64	1.9	-2.0	1.05	3	-3
2.2	4.4	6.65	6.77	13.43	2.8	-2.9	1.04	5	-4
2.6	5.2	6.69	6.58	13.27	4.1	-4.3	1.05	7	-7
3.0	6.1	7.01	7.25	14.26	5.9	-6.3	1.07	9	-9
3.5	7.0	7.73	7.69	15.42	8.4	-8.7	1.04	11	-11
3.8	7.7	8.08	7.96	16.04	9.6	-9.9	1.03	12	-12
4.0	8.0	8.35	8.35	16.71	10.5	-10.8	1.03	13	-13
4.2	8.4	8.47	8.49	16.96	11.2	-11.6	1.04	13	-14
4.4	8.7	8.91	9.02	17.93	13.0	-13.5	1.04	15	-15
4.5	9.0	8.92	8.86	17.78	15.3	-15.9	1.04	18	-19
4.7	9.4	6.78	6.77	13.55	33.0	-34.9	1.06	58	-60
4.9	9.7	5.73	5.95	11.68	66.6	-62.7	0.94	131	-115
5.0	10.1	5.81	6.02	11.83	63.1	-60.1	0.95	124	-111
5.2	10.4	5.62	5.96	11.58	87.8	-79.6	0.91	175	-142
5.4	10.8	5.71	6.12	11.83	90.7	-82.2	0.91	176	-144

In Figure 5.17a, the root-mean-square values of the surface height field ζ_{rms} (coating 1) shows the sharp transition in amplitude growth with increasing bulk velocity U_b. This is not only due to an increase in the wave height, but also due to an increase in the percentage of surface area covered by these waves (see Figure 5.22), as was previously visualized by the instantaneous height fields $\zeta(x, y, t)$.

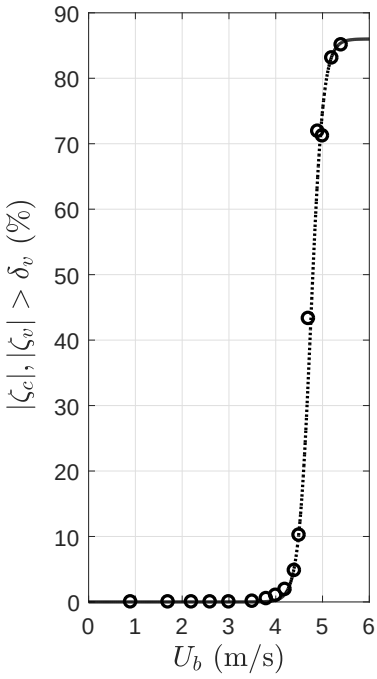

U_b (m/s)	δ_v (μm)	ζ_{rms} (μm)	$\lvert\zeta_c\rvert, \lvert\zeta_v\rvert > \delta_v$ (%)
0.9	141.1	1.4	0.0
1.7	75.2	2.1	0.0
2.2	61.2	2.8	0.0
2.6	51.7	4.0	0.0
3.0	44.8	5.8	0.0
3.5	39.5	8.0	0.1
3.8	36.2	9.3	0.5
4.0	34.7	10.1	1.0
4.2	33.3	11.0	1.9
4.4	32.1	12.3	4.8
4.5	30.9	15.6	10.2
4.7	29.9	31.5	43.3
4.9	28.9	56.4	71.9
5.0	27.9	53.5	71.2
5.2	27.2	74.4	83.1
5.4	26.2	82.1	85.1

Figure 5.22: Figure (left) indicates the percentage of surface area that is covered with waves where the absolute value of the crest $|\zeta_c|$ or the valley $|\zeta_v|$ is respectively higher or lower than the viscous boundary layer δ_v. The dotted line represents the data-fitted sigmoid curve. Table (right) presents the viscous boundary layer thickness δ_v, the coating surface fluctuation ζ_{rms} (coating 1) and the percentage of $|\zeta_c|, |\zeta_v| > \delta_v$ related to the bulk fluid velocity U_b.

5.3.4. SPATIAL CORRELATION

The spatial structure of the surface wave is characterised using the 2D two-point spatial correlation coefficient of the surface height field $C(r_x, r_y)$, which is defined by:

$$C(r_x, r_y) = \frac{\langle \zeta(x, y, t) \cdot \zeta(x + r_x, y + r_y, t) \rangle}{\langle \zeta(x, y, t)^2 \rangle} \tag{5.6}$$

Three correlation maps of streamwise/spanwise (x-y) direction are displayed in Figure 5.23, corresponding to the surface height fields $\zeta(x, y)$ of bulk velocities U_b = 3.5, 4.5 and 5.4 m/s respectively. Before transition (e.g. U_b = 3.5 m/s in Fig. 5.23a), the correlation maps reveal positive undulations being preceeded or succeeded by a valley. The finding that the negative minimum at $C(r_x, 0)$ deviates away from the origin $C(0, 0)$ with an increasing bulk velocity U_b, indicates that the wavelength is expanding. At the transition velocity U_b = 4.5 m/s, a second minimum is found nearer to zero, reflecting the occurrence of high amplitude and short wavelength wave trains (Fig. 5.23b). Beyond the transition bulk velocity (U_b > 4.5 m/s), a periodic sequence of positive maxima and negative minima is observed, indicating that the wave trains now dominate the surface deformation (Fig. 5.23c).

A more quantitative confirmation is done by analysing the correlation function based on the distance where the correlation coefficient has dropped to a value of 0.5. For a perfectly periodic wave train, $C(r_x, r_y) = C(\lambda_x/6, 0) = 0.5$ is chosen to estimate the characteristic (streamwise) wavelength. The preference would be to use $C(\lambda_x/4, 0) = 0$, however, the two lowest bulk velocities U_b = 0.9 and 1.7 m/s do not fulfill these requirements due to the absence of a zero-crossing. This Gaussian decay of $C(r_x, 0)$ is the result of a disordered deformation pattern in the reconstructed surface height fields $\zeta(x, y, t)$. Likewise, the characteristic (spanwise) wave width λ_y is estimated by $C(r_x, r_y) = C(0, \lambda_y/6) = 0.5$. The characteristic length scales λ_x and λ_y for all bulk velocities U_b are shown in Figure 5.24. The wavelength λ_x linearly increases (dash-dotted line) with bulk velocity between 2.5 m/s and pre-transition bulk velocity of 4.3 m/s, from $\lambda_x \sim$ 15 to 20 mm. The λ_x-values below U_b < 2.5 m/s deviate from this linear line due to the previously mentioned disordered deformation pattern at U_b =0.9 and 1.7 m/s or due to the occasional onset of surface waves with small amplitudes at U_b =2.2 m/s. At the transition velocity U_b = 4.5 m/s, the wavelength decreases rapidly with increasing bulk velocity to a wavelength-value around $\lambda_x \sim$ 11 mm. The wave width λ_y is around $\lambda_x \sim$ 25 mm before transition and then quickly increases up to $\lambda_x \sim$ 33 mm, confirming that the structure and the shape of pre- and post-transition waves are very different.

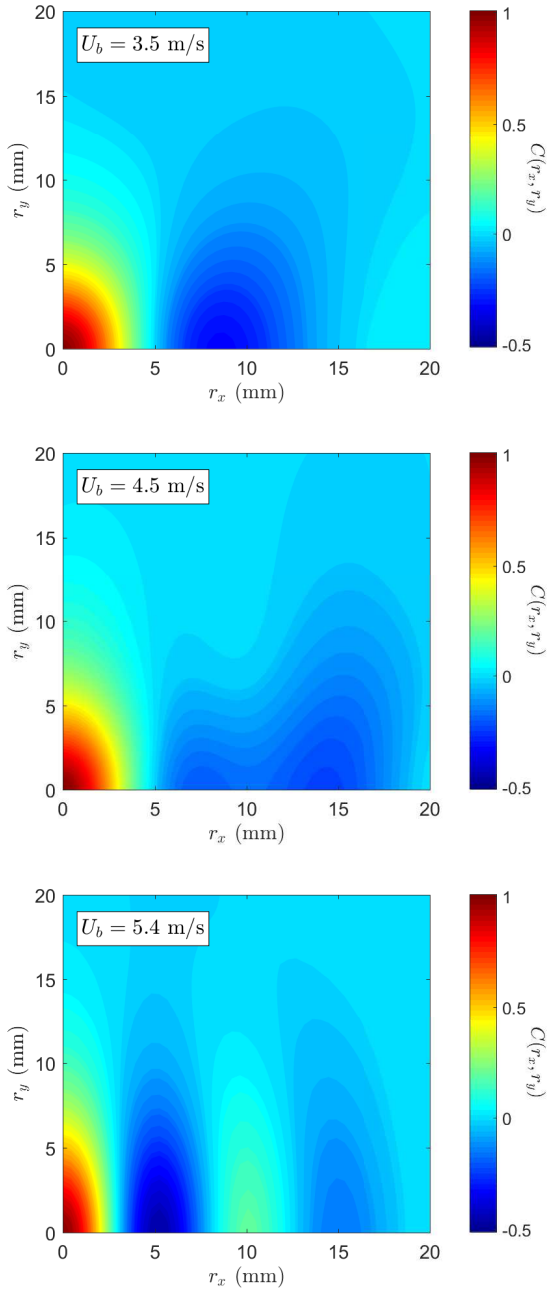

Figure 5.23: Correlation maps with the spatial correlation coefficient $C(r_x, r_y)$ for the three bulk velocities $U_b = 3.5$, 4.5 and 5.4 m/s, with r_x as streamwise direction and r_y as spanwise direction.

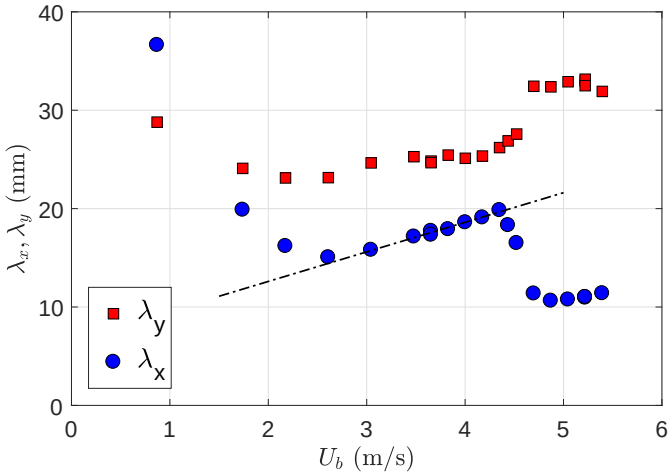

Figure 5.24: Streamwise (λ_x) and spanwise (λ_y) length scales vs bulk velocity U_b. The dash-dotted line indicates the linear growth of wavelength λ_x with the bulk velocity U_b in the one-way coupled regime.

5.3.5. SPATIO-TEMPORAL CORRELATION & DISPLACEMENT SPECTRA

The height-time diagrams and the spatio-temporal correlation maps of the aforementioned three bulk velocities (U_b = 3.5, 4.5 and 5.4 m/s) are visualised in Figure 5.25 and Figure 5.26, respectively. The height-time diagrams are compiled by plotting a narrow strip of the surface deformation $\zeta(x, y, t)$ in the streamwise direction into the (x, t)-plane, resulting in the surface deformation $\zeta(x, t)$ along the middle of the plate (Fig. 5.25). Below the transition velocity (< 4.5 m/s), the surface undulations propagate over the interface in streamwise direction, as can be seen by the regions of constant sign (i.e. crests or valleys). Around the transition velocity, shorter line segments of high amplitude propagate at a considerably lower velocity. These wave packets become more dominant for the higher bulk velocities. It is observed that, despite their lower velocity and high amplitude, these slow-moving wave packets are bounded by fast-moving low-amplitude waves. It suggests that the slow-moving waves are triggered *and* dampened by fast-moving waves, possibly due to the transfer of turbulent energy.

The spatio-temporal correlation of the surface deformation $\zeta(x, y, t)$ makes it possible to determine the characteristic wave propagation velocity as a function of the bulk velocity U_b. The spatio-temporal correlation $C(r_x, \tau)$ is the spatial and temporal averaged 2-time-2-point correlation of the surface deformation $\zeta(x, y, t)$ and is defined by:

$$C(r_x, \tau) = \frac{\langle \zeta(x, y, t) \cdot \zeta(x + r_x, y, t + \tau) \rangle}{\langle \zeta(x, y, t)^2 \rangle} \tag{5.7}$$

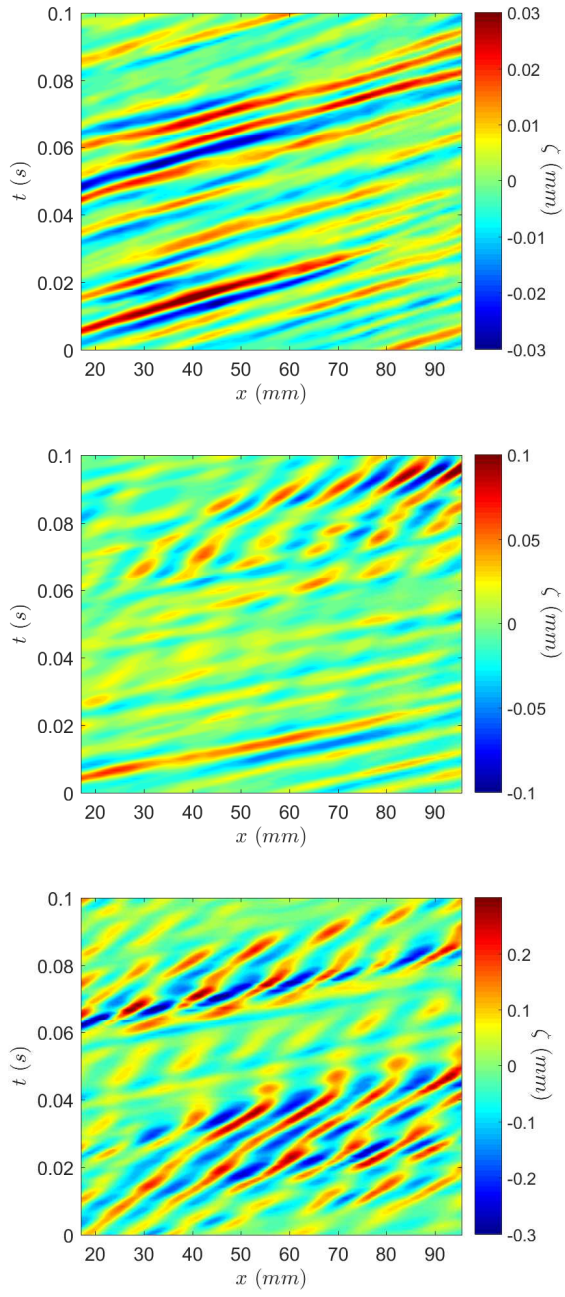

Figure 5.25: Height-time diagrams of the surface deformation $\zeta(x,t)$ along the middle of the plate in streamwise direction, for bulk velocities U_b = 3.5, 4.5 and 5.4 m/s.

The spatio-temporal correlation maps in Figure 5.26 clearly show the change in surface behavior as observed at the height-time diagrams. The corresponding characteristic wave propagation velocities c_w are quantitatively determined by the linear fit to the local maximum correlation-values in the spatial-temporal correlation map. The slope of the black dotted line corresponds to the propagation velocity of the wave that has a dominant presence on the surface interface, which is equal to $c_w = \Delta r_x / \Delta \tau$. The wave propagation velocities c_w are indexed in Table 5.4 for all bulk velocities U_b.

Table 5.4: The surface wave propagation velocities c_w related to the bulk velocity U_b. For $U_{b,trans} \leq 4.5$ m/s, a second wave appeared at the surface interface. The wave velocities of the dominant waves are in bold.

U_b (m/s)	Re_L $\times 10^6$	c_{w1} (m/s)	c_{w2} (m/s)
0.9	1.7	**0.60**	-
1.7	3.5	**1.31**	-
2.2	4.4	**1.63**	-
2.6	5.2	**1.99**	-
3.0	6.1	**2.37**	-
3.5	7.0	**2.67**	-
3.8	7.7	**3.03**	-
4.0	8.0	**3.21**	-
4.2	8.4	**3.32**	-
4.4	8.7	**3.42**	-
4.5	9.0	**3.49**	0.69
4.7	9.4	3.58	**0.71**
4.9	9.7	3.71	**0.85**
5.0	10.1	3.63	**0.86**
5.2	10.4	3.60	**0.90**
5.4	10.8	3.86	**0.90**

Below the transition velocity $U_b < 4.5$ m/s, the (phase) velocity of the propagating waves increases linearly with bulk velocity, $c_w = 70 - 80\% U_b$. This corresponds to the propagation velocity of the highest-intensity turbulent pressure fluctuations high up in the turbulent boundary layer (TBL) far away from the wall [53]. So, regarding the similar propagation velocity, it is believed that these pressure fluctuations are responsible for the surface deformation, and there is presumably a one-way coupling between the turbulent flow and the responding wall: the compliant wall is deformed by the pressure fluctuations, but the deformed wall does not alter the turbulent flow as has been indicated by the force measurements.

In the transitional regime, the wave packets (shorter waves, higher amplitudes) modify the correlation map; small wiggles appear around the local maximum of the correlation-values. From the transition bulk velocity U_b and above, the wave packets start to dominate the surface interface. The slope of the black dotted line still represents the dominant waves, while the white dotted line represents the secondary waves. The propagation velocity, or phase velocity, of the new primary waves (wave packets) is significantly

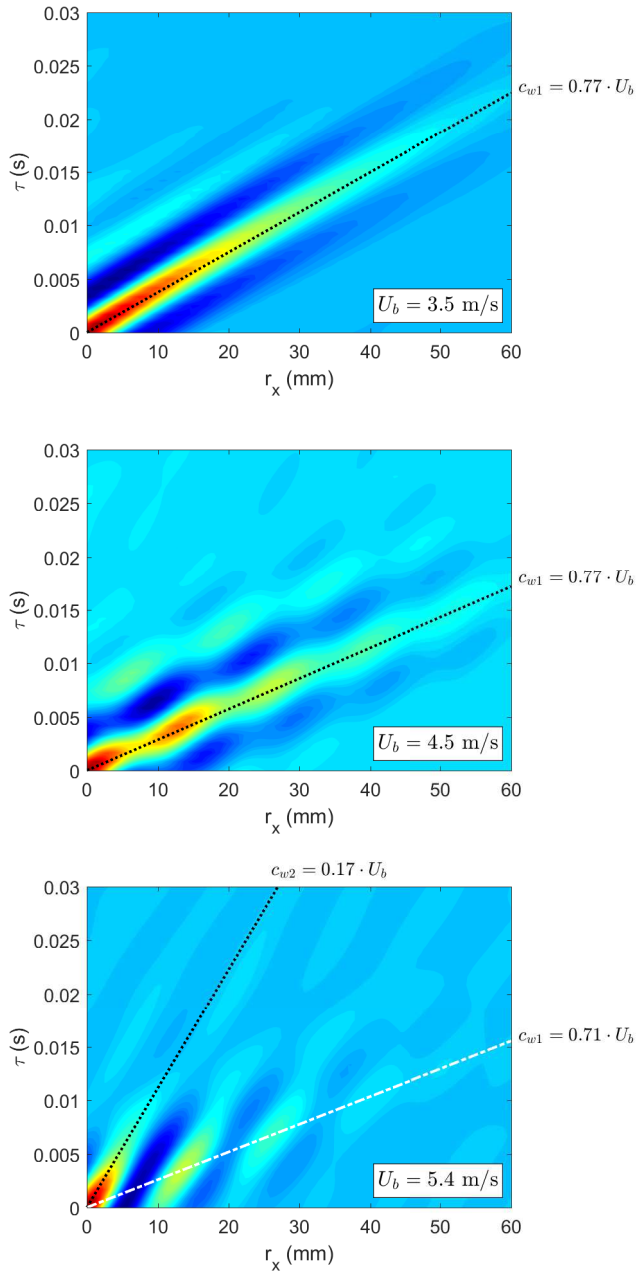

Figure 5.26: Spatio-temporal correlation map of bulk velocities U_b = 3.5, 4.5 and 5.4 m/s. The least square fit through the local maxima is given by the black dotted line (dominant wave) and the white dot-dashed line (secondary wave).

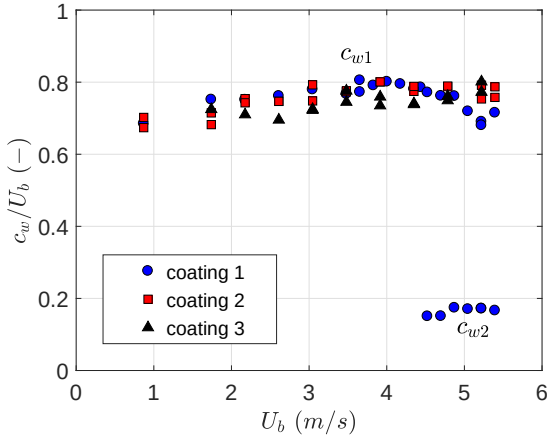

Figure 5.27: Surface wave velocity c_w/U_b as a function of the bulk velocity U_b.

lower than the primary waves before transition, namely around ~17% of the bulk velocity U_b (Fig. 5.27). It is worth mentioning that in this velocity regime, the waves on the surface of coating 2 and 3 maintained the similar traveling velocity as the pressure fluctuations, i.e. 70-80% of U_b. The lower propagation velocity of coating 1 is therefore presumed to be related to the complex dynamics of the visco-elastic material itself. The height-time diagrams suggest that the short waves are modulated by the fast moving undulations, which was also implied by the direct visualisations. The surface deformation is initiated by the large scale structures in the outer layer of the turbulent boundary layer, and simultaneously the upward undulations of the coating surface start to protrude through the laminar viscous sublayer. It seems likely that this is a necessary condition to transfer energy from the flow towards the coating to excite and initiate a surface wave that is defined by the material properties. Therefore, the front side of the wave packets moves with the same velocity as the pressure fluctuations of the turbulent boundary layer. Once initiated, the undulations progress at their own lower wave velocity (c_{w2}). The consequence is a two-way coupling: the interface waves are initiated by the turbulent flow, but once there, the turbulent flow experiences substantial high local roughness and increases the skin friction and turbulent activity.

DISPLACEMENT SPECTRA

The normalized spectra of the vertical surface displacement are shown in Figure 5.28. Each spectrum is normalized with ζ^2_{rms}, which is the integral of the spectrum. The spectrum was filtered and smoothed as discussed by Benschop *et al.* [10]. The rms-values of the filtered data varied between 83% and 98% of the rms-values of the unfiltered data.

The spectra can be divided into two groups; before and after transition. The dominant frequency before transition is around f = 144 Hz, while beyond the transition velocity U_b > 4.5 m/s the peak shifts to a lower value of f = 94 Hz. The peak shift is attributed to the change in wave dynamics for the transition from the one-way to the two-way coupled system.

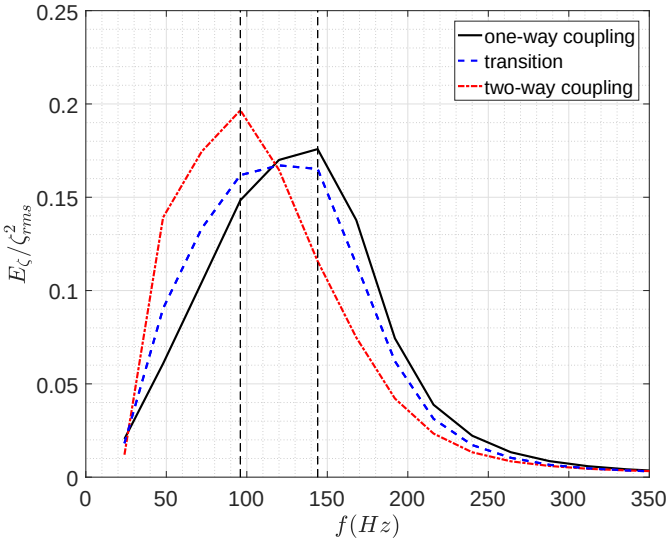

Figure 5.28: Surface displacement spectra E_ζ/ζ^2_{rms} as function of deformation frequency f. The three spectra correspond to the surface reconstruction results of bulk velocities U_b = 3.5 (black solid line), 4.5 (blue dashed line) and 5.4 m/s (red dash-dotted line), and represents the characteristic spectra for each regime.

An alternative method to characterize the streamwise wavelength λ_x is applied by combining the wave propagation velocity and the dominant frequency obtained from the displacement spectra, such that $\lambda_x = c_w/f$. Beyond transition, the secondary (long) waves are assigned with the one-way coupling frequency f = 144 Hz, while the dominant (short) waves of the wave packets have the two-way coupling frequency f = 96 Hz. The alternatively obtained wavelength λ_x as a function of the bulk velocity U_b is presented in Figure 5.29.

Before the transition velocity, the characteristic wavelengths λ_x are higher compared to the values obtained via the spatial correlation method (Fig. 5.23); the spatial correlation criterion $C(r_y, r_x) = C(0, \lambda_x/6) = 0.5$ underestimates the streamwise wavelength λ_x. A spatial correlation criteria $C(r_y, r_x) = C(0, \lambda_x/4) = 0$ would have been more appropriate where possible, as already mentioned in Section 5.3.4, which delivers similar wavelengths as the current alternative characterization method. In the two-way coupling regime ($U_b > 4.5$ m/s), when the dominant and the secondary waves are both present on the surface interface, the spatial correlation method does not distinguish the two types of waves and the alternative method to determine the wavelength λ_x is therefore preferred. The dominant waves have wavelengths around $\lambda_x \sim 9$ mm, while the secondary waves are around $\lambda_x \sim 26$ mm.

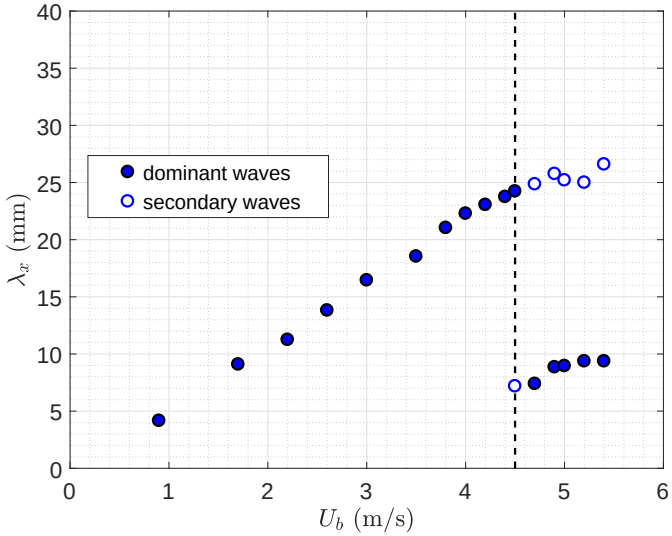

Figure 5.29: Wavelength λ_x of the dominant and the secondary waves in the one-way (U_b <4.5 m/s) and the two-way (U_b >4.5 m/s) coupled regime.

5.3.6. VELOCITY FIELD ANALYSIS

This section discusses the analysis of the particle image velocimetry (PIV) and particle tracking velocimetry (PTV) measurements, obtained by the measurements with the smooth and coated plate in the watertunnel described in Section 5.2. As discussed, only coating 1 was selected for further analysis of the interaction between fluid flow and the compliant surface. The raw images are used to determine the fluid-surface interface roughly, followed by characterization of the surface deformation. The velocity data is obtained by PIV, as well as PTV for the region close to the wall. The average of the instantaneous velocity data is used to determine the mean velocity profiles and to investigate other turbulent flow statistics. The velocity measurements were performed at five bulk velocities: three pre-transition bulk velocities (U_b = 1.7, 3.5 and 4.4 m/s) and two post-transition velocities (U_b = 4.8 and 5.2 m/s).

WAVE CHARACTERISTICS

The deformation of the surface interface is clearly visible in the raw image in Figure 5.30, and indicates the typical shape of a sinusoidal wave. The flow direction for all the PIV recordings is from right to left. The image shows a homogeneous grey-scale colour in the region of the coating, while the fluid flow mainly consists of a black background with random white spots representing the images of the tracer particles. Bright white spots at the coating/fluid boundary are substantial reflections from the interface, caused by small oil droplets present on the coating surface. The interface is difficult to detect using a computer algorithm, although the apparent boundary is readily visible by eye. It is stated 'apparent boundary', as the image is a 2d-impression of the coating/fluid, while the surface deformation measurements (i.e. BOS) demonstrated 3d-shaped waves. Therefore the coating/fluid boundary is determined by allocation of

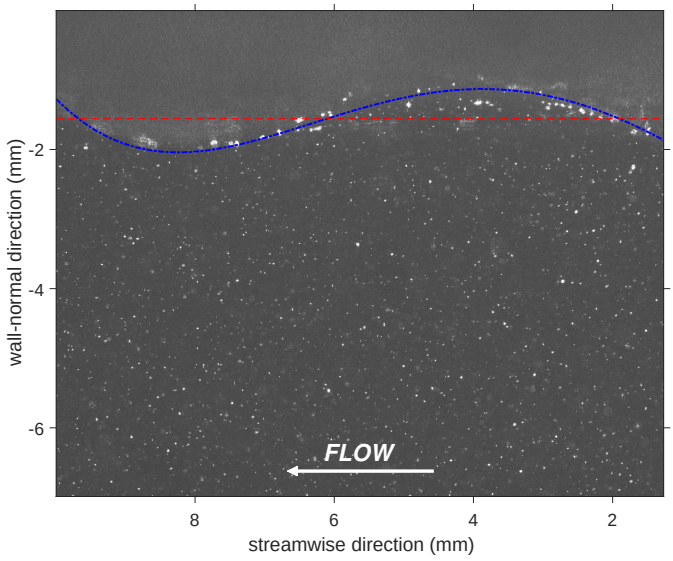

Figure 5.30: PIV image with a visible wavy fluid-surface interface, fluid flow from right to left (U_b =5.2 m/s). The blue line indicates the interface, red dashed line is the mean surface position.

5 points (manually) on the interface with equal spacing, followed by a polynomial fit and delivers the estimated coating/fluid boundary (blue dashed line). The red dashed line represents the non-compliant rigid wall, and corresponds to the average of the 500 estimated coating/fluid interfaces.

Statistical convergence of the velocity data is expected by taking 500 images at every bulk velocity U_b. For each image, the shape of the surface is determined by the procedure described above. Figure 5.31 indicates that the surface height distribution is identical to the distribution that was obtained by the BOS measurements. The root-mean-square values of the surface height were computed for the five bulk velocities and are similar to the rms-values obtained by BOS (Fig. 5.32). There is a small deviation in rms-values for the lowest bulk velocity $U_b = 1.7$ m/s, most likely due to the accuracy of the manual allocation of the 5 points on the fluid-surface interface, as $\zeta_{rms} = 8\mu$m corresponds to ~1 pixels. Hence, the described procedure to determine the surface interface is considered to be sufficiently reliable for further (velocity) data analysis.

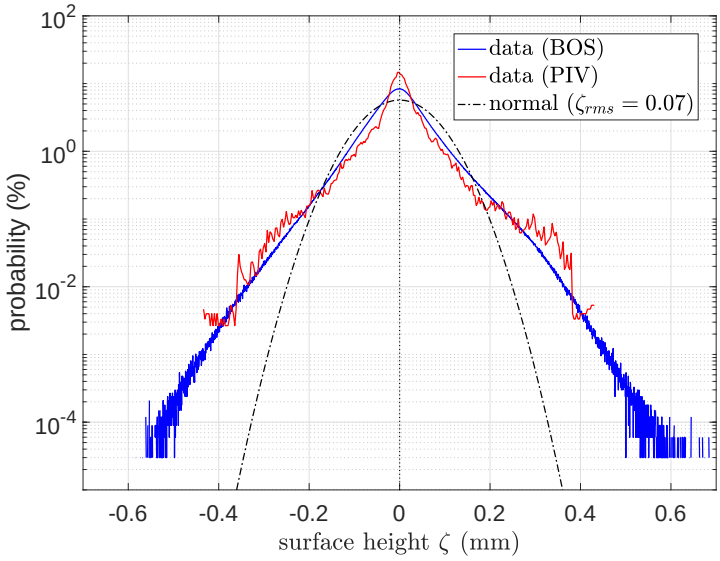

Figure 5.31: Surface height distribution based on the data obtained via BOS (2000 samples) and PIV (500 samples) at bulk velocity U_b = 5.2 m/s. The data is compared to a normal distribution with a standard diviation of ζ_{rms} = 0.07. Statistics: ζ_{rms} = 0.0703 (BOS) and 0.0682 (PIV), skewness of 0.278 (BOS) and 0.303 (PIV), and kurtosis of 6.09 (BOS) and 9.82 (PIV).

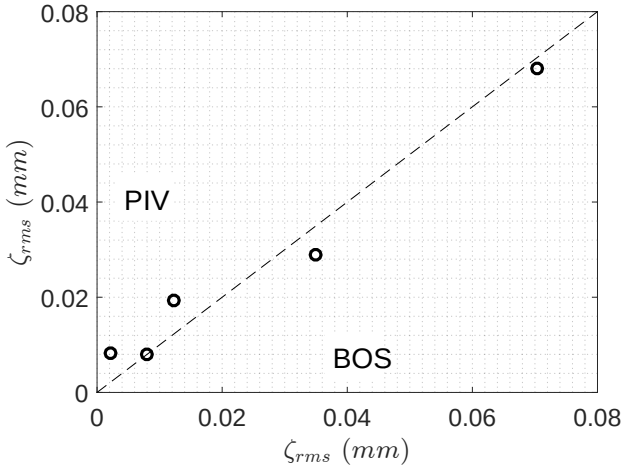

Figure 5.32: Surface height fluctuation ζ_{rms} obtained by the BOS measurements and the PIV measurements. The symbols from left to right represent the data obtained at a bulk velocity U_b = 1.7, 3.5, 4.4, 4.8 and 5.2 m/s.

MEAN FLOW ANALYSIS

Instantaneous velocity fields at a bulk velocity of $U_b = 5.2$ m/s are presented in Figure 5.33 and Figure 5.34 for the flow over a smooth flat plate and a coated plate, respectively. At first sight, the instantaneous velocity fields along the flat plate and the marginally deformed coating surface (Fig. 5.34a) do not show a significant difference, although the boundary layer thickness appears to be much smaller for the latter. When the coating surface deforms extremely (Fig. 5.34b), two main distinctions in the velocity field are observed: (1) close to the wall a region with very low (and in a small area even negative) velocities at the leeward side of the wave, and (2) further away from the wall higher velocities. A more detailed investigation of the velocity data was performed to quantify the influence of the coating on the near-wall velocity field.

The PIV analysis was used for the reconstruction of the velocity in the log layer, while the PTV analysis (i.e super-resolution method, Keane *et al.* [46]) was used to determine the velocity in the region close to the wall up to the first part of the log layer. The mean velocity profiles $\bar{u}$ were obtained by temporally and spatially averaging the velocity fields. Time-averaging was done over 500 instantaneous velocity fields and spatial averaging was applied in the streamwise direction, as the flow is considered to be homogeneous in the streamwise direction given the small field of view (FOV). The mean streamwise velocity profiles $\bar{u}$ are presented in Figure 5.35 and 5.36. The values of $\bar{u}$ and y are scaled in wall units u_τ. The local friction velocity u_τ was determined by fitting the velocity in the log region with a fixed slope $\partial\bar{u}^+/\partial y^+ = 1/\kappa y^+$ [54], where $\bar{u}^+ = \bar{u}/u_\tau$, $y^+ = yu_\tau/\nu$ and $\kappa = 0.41$ [7]. Although it results in an artificial collapse of the velocity data onto the universal log-law line, the application is considered to be valid for high Reynolds numbers [55]. Consequently, the local wall shear stress becomes $\tau_w = \rho_f u_\tau^2$ and corresponds very well to the estimated value of $6/7\bar{\tau_w}$, where $\bar{\tau_w}$ is the averaged wall shear stress obtained by the force measurements (Table 5.5). For bulk velocities

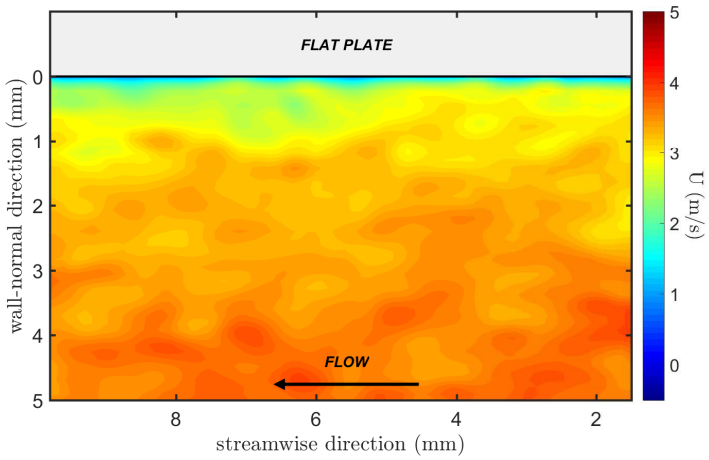

Figure 5.33: Instantaneous velocity field along a smooth flat plate, at a bulk velocity of $U_b = 5.2$ m/s.

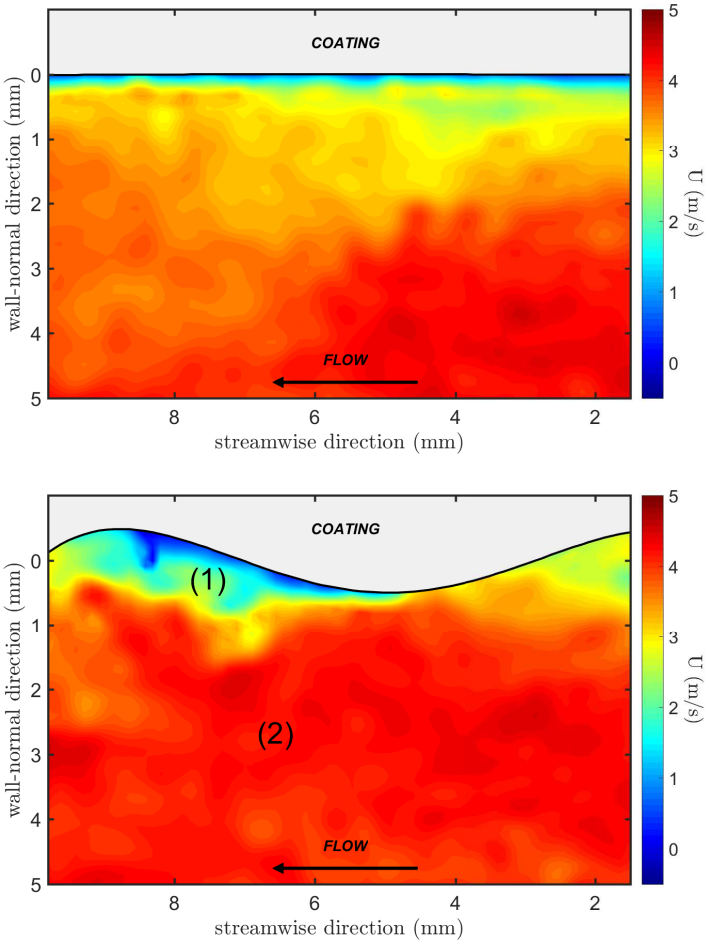

Figure 5.34: Instantaneous velocity fields along a coated plated at bulk velocity U_b = 5.2 m/s, with (a) marginal surface deformation, and (b) excessive surface deformation. Area (1): region with very low (and negative) velocities, and area (2): high velocities further away from the wall.

U_b < 4.5 m/s, the local shear stresses τ_κ of the coating plate were slightly larger than those of the smooth plate, in contrast to the values obtained by the force measurements. This demonstrates that the *global* force measurements do not perceive a drag change for the coating plate below the transition bulk velocity U_b = 4.5 m/s, while the results of the *local* PIV measurements suggest small changes of the frictional drag.

The reconstructed velocity profiles $\bar{u}$ were compared to the theoretical velocity profile related to a smooth flat surface. First, the experimental results of the smooth plate are presented. As expected, the velocity close to the wall match very well with the theoretical profile for smooth surfaces. The velocity profile for high bulk velocities deviates

Table 5.5: Estimated local shear stress via the force measurements ($\tau_{\bar{t}}$) and the log-fit method (τ_κ) for the smooth flat plate and the coated plate, as a function of the bulk velocity U_b.

U_b (m/s)		$\tau_{\bar{t}}$ (Pa)	τ_κ (Pa)	$\tau_\kappa/\tau_{\bar{t}}$ (-)
1.7	smooth	4.58	4.02	0.878
	coating	4.49	4.45	0.991
3.5	smooth	16.18	14.82	0.916
	coating	16.37	15.70	0.959
4.4	smooth	24.33	22.30	0.917
	coating	24.65	23.61	0.958
4.8	smooth	28.87	26.81	0.929
	coating	31.68	30.06	0.949
5.2	smooth	33.73	31.93	0.947
	coating	44.03	42.58	0.967

slightly from the expected profile below $y^+ < 5-10$, likely due to small vibrations of the watertunnel at these velocities. In the log-law region $y^+ > 30$, the velocity profiles show similarity and identical behavior (i.e. collapse). The logarithmic relation of smooth-walls is given by:

$$u^+ = \frac{1}{\kappa}\ln\left(y^+\right) + B \tag{5.8}$$

and is defined by the von Kármán constant $\kappa = 0.41$ and the smooth-wall log-law intercept $B = 5.2$ [56].

The profiles of the coating plate show some interesting results. In the near-wall region $y^+ < 30$, the velocity profile deviates from the theoretical profile for smooth surfaces $u^+ = \frac{1}{0.41}\ln(y^+) + 5.2$. This arises for both the pre-transition and the post-transition bulk velocities. Even though the pre-transition regime ($U_b < 4.5$ m/s) is considered to be one-way coupled, the velocity profiles show a noticeable effect of the coating deformation. Further away from the wall, in the log region, the velocity profiles are unaltered compared to those of the smooth plate. Beyond the transition velocity $U_b > 4.5$ m/s, the velocity profile shifts downwards in the log region, which is associated with drag increase due to significant surface deformations (i.e. 'dynamic' roughness). The roughness function Δu^+ can be included as an additional term in the log law relation of the wall [57–62]:

$$\bar{u}^+ = \frac{1}{\kappa}\ln\left(y^+\right) + B - \Delta u^+ \tag{5.9}$$

The downward shift Δu^+ is estimated by the mean difference of $\bar{u}^+ - \left(\frac{1}{\kappa}\ln\left(y^+\right) + B\right)$, with the von Kármán constant $\kappa = 0.41$ and the smooth-wall log-law intercept $B = 5.2$.

The obtained downward shift Δu^+ in the velocity profiles for U_b = 4.8 and 5.2 m/s are 1.0 and 3.4, respectively.

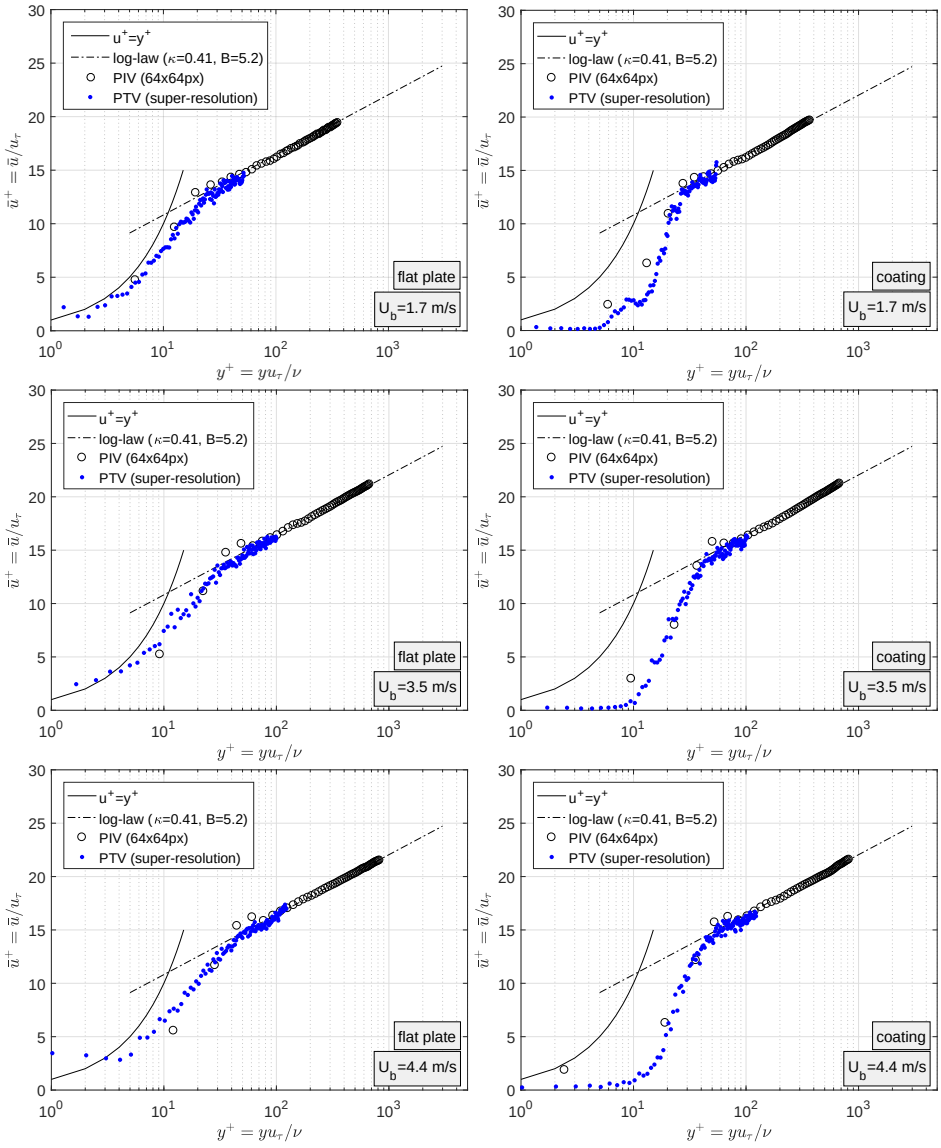

Figure 5.35: Pre-transition velocity profiles for the smooth flat plate and coated plate at bulk velocity U_b =1.7, 3.5 and 4.4 m/s, respectively.

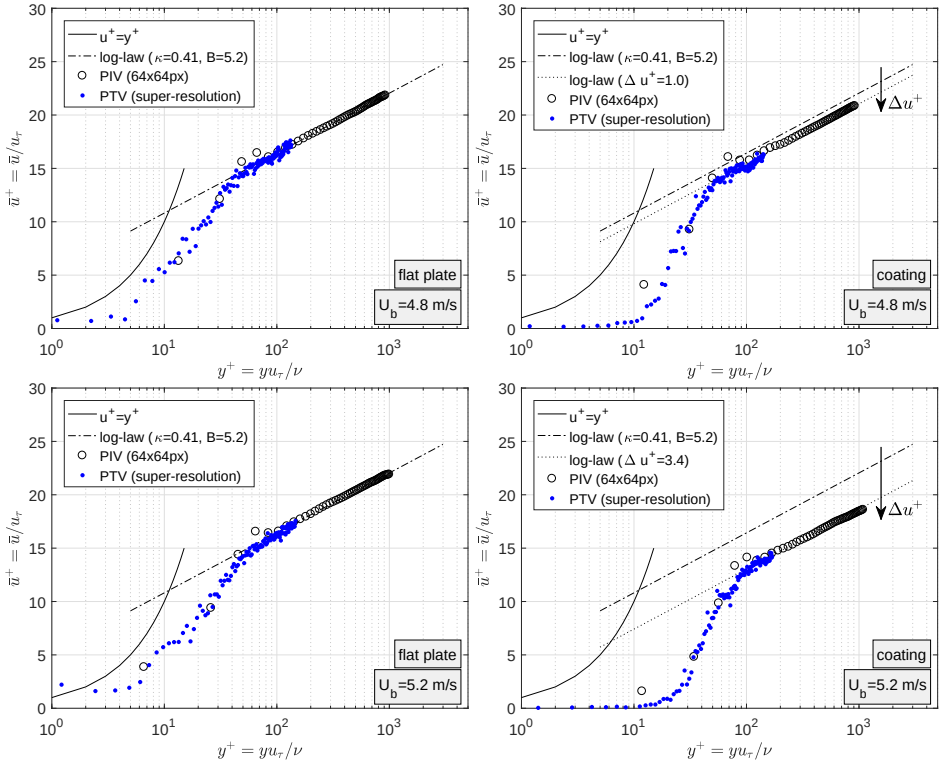

Figure 5.36: Post-transition velocity profiles for the smooth flat plate and coated plate at bulk velocity U_b =4.8 and 5.2 m/s, respectively.

For rough surfaces, experimental investigations showed that the roughness function Δu^+ correlates well with the fluctuations of the wall-normal velocity component v_{rms} at the mean surface interface $y = 0$ [63]. A linear correlation was suggested based on DNS results for turbulent channel flow with well defined roughness elements [64, 65]:

$$\Delta u^+ \approx \frac{B}{\kappa} v^+_{rms} \tag{5.10}$$

The downward shift Δu^+ can also be estimated based on the dynamic wall motions, when assuming that the rms-values of the wall-normal fluid velocity v^+_{rms} at the mean surface interface $y = 0$ correspond with the rms-values of the coating velocity in wall-normal direction $v^+_{c,rms}$. This would not be valid in the one-way coupled regime, since the surface deformations and wall dynamics are small enough that possible flow perturbations are completely damped out by the fluid viscosity, resulting in a downward shift of $\Delta u^+ = 0$ as was demonstrated for bulk velocities U_b = 1.7, 3.5 and 4.4 m/s (Fig. 5.35). The coating velocity in wall-normal direction $v_{c,rms}$ was derived from the obtained height fields $\zeta(x, y, t)$ and finally results in $v_{c,rms} = (\partial\zeta/\partial t)_{rms}$, shown in Figure

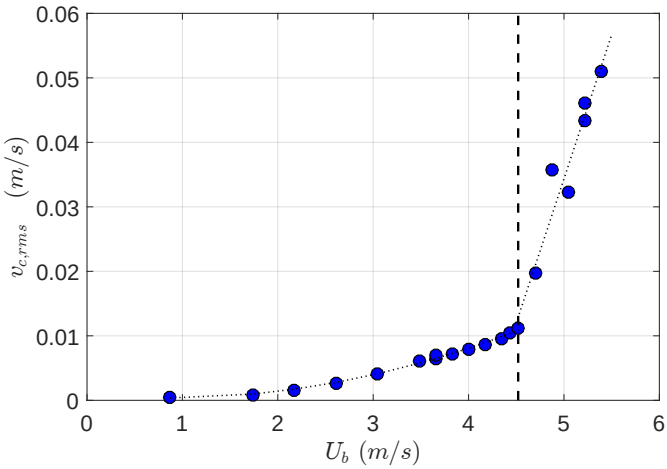

Figure 5.37: Rms-values of the coating surface velocity in wall-normal direction $v_{c,rms}$, based on the reconstructed height fields $\zeta(x,y,t)$, such that $v_{c,rms} = (\partial\zeta/\partial t)_{rms}$. The dashed line indicates the transition of one-way/two-way coupled system. The dotted lines are illustrative.

5.37. In order to obtain $v^+_{c,rms}$, the coating velocities in wall-normal direction $v_{c,rms}$ are normalised with the local friction velocities u_τ.
Figure 5.38 shows that the linear correlation delivers similar results as the obtained downward shift Δu^+ of the velocity profiles. For $U_b = 5.2$ m/s, the linear correlation slightly underestimates the downward shift ($\Delta u^+ = 2.9$ versus 3.4), while for $U_b = 4.8$ m/s the downward shift is overestimated ($\Delta u^+ = \pm 1.8$ versus 1.0). It is believed that the presence of two types of waves, the so-called one-way coupled waves (long waves with low amplitudes) and two-way coupled waves (short waves with high amplitude), affects the linear correlation of the roughness function Δu^+ in the two-way coupled regime (Eq. (5.10)). Far beyond the 1-way/2-way transition, the short waves with high amplitudes dominate the coating surface and supports the possible use of the linear correlation for the roughness function Δu^+ that corresponds to the downward shift due to the growth in surface roughness.

The linear correlation of the roughness function Δu^+ makes it possible to scale the equivalent sandgrain roughness k_s of Nikuradse [47] with the root-mean-square values of the surface height field ζ_{rms}. The values of Δu^+ are forced to collapse on the Nikuradsu-curve by making use of $k^+_s = \beta\zeta^+_{rms}$, as shown in Figure 5.39. At the 1-way/2-way transition velocity $U_b = 4.5$ m/s, the surface roughness starts to match the viscous sublayer $k_s \sim \delta_v$, which makes the equivalent sandgrain roughness $k_s \simeq 2\zeta_{rms}$. In the transitionally rough regime $5 \leqslant k^+_s \leqslant 70$, parameter β shows a declining trend with increasing bulk velocity U_b. The decline of parameter β is caused by the increase of surface roughness and wave density with increasing bulk velocity U_b, in contrast to Nikuradse [47] who only used a fixed surface roughness with a narrow sandgrain roughness distribution. The effective roughness is $k_s = (1.1-2.3)\zeta_{rms}$, which is significantly lower than the more commonly accepted value $k_s = (3-5)k_{rms}$ [57, 59].

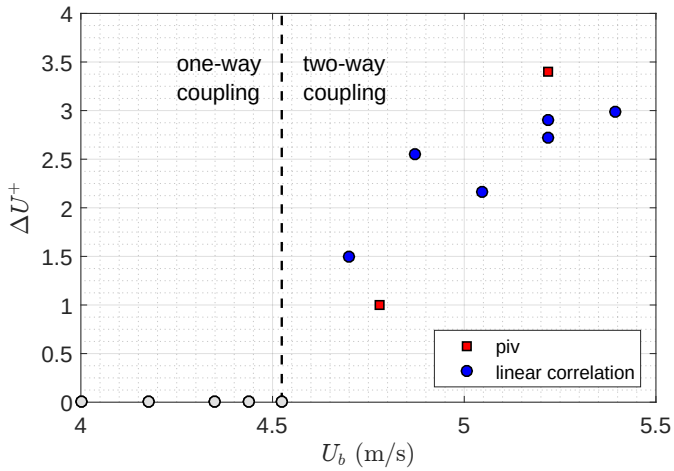

Figure 5.38: Roughness function Δu^+, based on the linear correlation of Eq. (5.10) with $v^+_{rms} = v^+_{c,rms}$ and the linear correlation based on the downward shift obtained by PIV. Gray symbols are based on the assumption $\Delta u^+ = 0$ for the one-way coupled system.

In conclusion, the wall-normal velocity fluctuations have an evident contribution to the drag. Although, surface deformations lead to an increase of v_{rms} at the mean surface interface $y = 0$, it does not imply a drag increase associated with a downward shift Δu^+ of the velocity profile in the log-region for bulk velocities in the one-way coupled regime. As stated previously, favorable interaction of the compliant surface with the turbulent flow may suppress the velocity fluctuation v' that diminish the turbulent Reynolds stress due to $-\rho\langle(u' + u_c)(v' + v_c)\rangle$. None of these hypotheses could be verified in the current study.

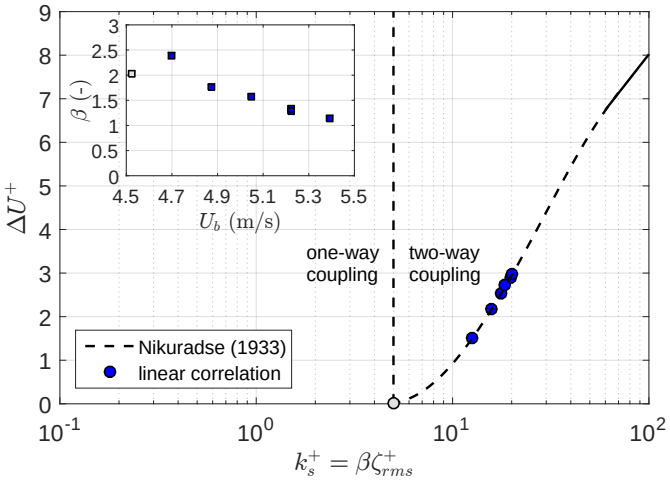

Figure 5.39: Roughness function Δu^+ as a function of the equivalent sandgrain roughness $k_s^+ = \beta\zeta_{rms}^+$. The inset indicates the decline of parameter β with increasing bulk velocity U_b.

5

ASSESSMENT OF TURBULENT LENGTH SCALES AND DISSIPATION RATES.
The spatial resolution of PIV is often the limiting factor to fully resolve the turbulent fluid motions at high Reynolds numbers. In order to verify whether all (small) turbulent motions are captured by the applied PIV method, the spatial resolution is compared to the smallest relevant length scale of the flow, defined as the Kolmogorov microscale λ_K:

$$\lambda_K = \left(\frac{\nu^3}{\epsilon}\right)^{1/4} \tag{5.11}$$

where ν is the kinematic viscosity, and ϵ the kinetic energy dissipation rate per unit mass. Initially, the dissipation rate ϵ can be estimated based on the energy-cascade model, where the turbulent energy is dissipated by the smallest eddies. In the near-wall region, the production and dissipation of turbulent kinetic energy are generally in balance. This leads to an accurate estimation of the dissipation rate ϵ_{est} when the friction velocity u_τ is known [66]:

$$\epsilon_{est} = \frac{u_\tau^3}{\kappa y} \tag{5.12}$$

The mean dissipation rate $\bar{\epsilon}_{est}$ is used for further analysis and is determined by averaging the computed estimated dissipation rate ϵ_{est} in the near-wall flow region $y < 5$ mm. This corresponds with the wall-normal distance of the reconstructed PIV velocity fields. The spatial resolution is defined by the vector spacing Δx used during the

PIV processing (i.e. interrogation window size D_I and accompanying overlap). As reported by Saarenrinne and Piirto [67], the ratio between the vector spacing Δx and the Kolmogorov length scale λ_K (Eq. (5.11)) should be $\Delta x/\lambda_K \leqslant 3$ (50% overlap) to fully resolve the smallest fluid motions, which is in close conformity with $\Delta x/\lambda_K \approx 1.5-2.0$ (75% overlap) reported by Tokgoz *et al.* [68]. The obtained $\Delta x/\lambda_K$ values in Table 5.6 indicate that the smallest scale fluctuations are not fully resolved in the present study by the applied PIV method, especially for bulk velocities $U_b > 1.7$ m/s.

Table 5.6: Turbulent length scales characteristics

U_b (m/s)	$\overline{\epsilon}_{est}$ (m^2/s^3)	$\overline{\lambda}_{K,est}$ (μm)	$\Delta x/\overline{\lambda}_{K,est}$ (-)
1.7	0.57	43.5	2.5
3.5	4.25	26.6	4.1
4.4	7.62	22.9	4.8
4.8	7.40	21.7	5.0
5.2	10.58	20.2	5.4

Nevertheless, a good estimation of the dissipation rate ϵ can still be computed by using the PIV data, even though the small scale fluctuations are filtered out due to the limit of the spatial resolution. The dissipation rate ϵ is computed from the velocity derivatives obtained by the planar PIV measurements. Since planar PIV delivers only two velocity components (u and v), the dissipation rate ϵ is estimated by using all the measured velocity components and the statistically local isotropic assumption for the unmeasured component (w), which results in [69]:

$$\epsilon = \nu\left\{2\overline{\left(\frac{\partial u'}{\partial x}\right)^2} + 2\overline{\left(\frac{\partial v'}{\partial y}\right)^2} + 3\overline{\left(\frac{\partial u'}{\partial y}\right)^2} + 3\overline{\left(\frac{\partial v'}{\partial x}\right)^2} + 2\overline{\left(\frac{\partial u'}{\partial y}\frac{\partial v'}{\partial x}\right)}\right\} \tag{5.13}$$

The mean dissipation rate $\overline{\epsilon}$ is determined over the 500 instantaneous velocity fields. In order to make a quantitative comparison, the mean dissipation rates $\overline{\epsilon}$ is made non-dimensio-nal with the theoretical dissipation rate $\overline{\epsilon}_{est}$ from Table 5.6, resulting in the normalised parameter $\overline{\epsilon^*}$. Table 5.7 indicates that the current planar PIV measurements underestimate the actual mean dissipation rates, which is expected due to the limited spatial resolution.

The computed dissipation rate $\overline{\epsilon}$ can be improved by using a LES sub-grid-scale model to estimate the dissipation rate contribution of the unresolved scales, as proposed by Sheng *et al.* [70]. The Smagorinsky model [71] was indicated to be a reliable sub-grid-scaling method to estimate the mean dissipation rate $\overline{\epsilon}_{sgs}$ for high Reynolds number turbulent flows. Similar to Khan [72] and Gabriele *et al.* [73], the dissipation rate ϵ_{sgs} is computed from the determined velocity gradients, the grid spacing Δ and the so-called Smagorinsky constant C_s:

$$\epsilon_{sgs} = (C_s\Delta)^2 \left\{ 2\overline{\left(\frac{\partial u'}{\partial x}\right)^2} + 2\overline{\left(\frac{\partial v'}{\partial y}\right)^2} + 3\overline{\left(\frac{\partial u'}{\partial y}\right)^2} + 3\overline{\left(\frac{\partial v'}{\partial x}\right)^2} + 2\overline{\left(\frac{\partial u'}{\partial y}\frac{\partial v'}{\partial x}\right)} \right\}^{3/2} \tag{5.14}$$

Table 5.7 shows that the sub-grid-scaling method improves the dissipation rate estimation, $\overline{\epsilon^*}_{sgs}$ in contrast to $\overline{\epsilon^*}$. The estimated dissipation rate ϵ_{sgs} is strongly dominated by the chosen value of parameter C_s. The ratio between the spatial resolution Δx and the Kolmogorov scale λ_K has been suggested to be a proper guideline to determine the correct Smagorinsky constant C_s [74].

Table 5.7: Turbulent length scales characteristics

U_b (m/s)	$\bar{\epsilon}$ (m^2/s^3)	$\overline{\epsilon^*}$ (-)	$\bar{\epsilon}_{sgs}$ (m^2/s^3)	$\overline{\epsilon^*}_{sgs}$ (-)
1.7	0.35	0.61	0.33	0.58
3.5	1.34	0.32	2.75	0.65
4.4	2.11	0.28	5.60	0.74
4.8	2.49	0.34	6.84	0.92
5.2	2.79	0.26	9.06	0.86

TURBULENCE STATISTICS

The analysis of the turbulent characteristics is done by Reynolds decomposition of the measured velocity components u and v into the mean velocity components $\bar{u}$ and $\bar{v}$, and the turbulent fluctuation around the mean velocity u' and v', which results in:

$$u'(x,y,t) = u(x,y,t) - \bar{u}(x,y) \tag{5.15}$$

and

$$v'(x,y,t) = v(x,y,t) - \bar{v}(x,y) \tag{5.16}$$

The mean velocity parameters $\bar{u}(x,y)$ and $\bar{v}(x,y)$ are obtained by temporally averaging the 500 instantaneous velocity fields. The velocity fluctuations $u'(x,y,t)$ and $v'(x,y,t)$ are input values to compute the turbulent stress components $\left\langle u'^2 \right\rangle$, $\left\langle v'^2 \right\rangle$ and $\langle u'v' \rangle$, where $\langle \bullet \rangle$ represents the temporal and spatial average in the streamwise direction. The turbulent stresses indicate how the turbulent flow is affected by the motions of the compliant wall in comparison with the smooth rigid wall. The total shear stress of the fluid is given by:

$$\tau = \mu\frac{\partial \bar{u}}{\partial y} - \rho \langle u'v' \rangle \tag{5.17}$$

The first term represents the viscous shear stress and dominates close to a rigid smooth wall as the velocity gradients are large in the very near-wall region. The second term

represents the turbulent Reynolds stress that normally dominates in the log-layer. In this region, the measured Reynolds stress $-\rho\langle u'v'\rangle$ does not require fully resolved fluid motions to construct accurate values [43]. Figure 5.40 displays the measured Reynolds stress $-\rho\langle u'v'\rangle$ related to the absolute wall-normal distance (linear scale) for bulk velocities $U_b = 1.7 - 5.2$ m/s, open symbols represent the rigid smooth plate and closed symbols are the compliant coating plate. The Reynolds stresses related to the compliant coating (closed symbols) are all (slightly) higher compared to the smooth plate (open symbols). For the compliant coating, all curves have a similar trend in the very near-wall region ($y < 0.5$ mm), which is most noticeable for $U_b = 5.2$ m/s. The fluid motions close to the interface modify the velocity profile $\bar{u}$ (see Figures 5.35 and 5.36) and with that the velocity gradient $\partial\bar{u}/\partial y$, which results in a decrease of the viscous shear stress. Simultaneously, the fluid motions enhance the velocity fluctuations that give rise to the Reynolds stress in the near-wall region, which is indirectly related to the wall motions of the compliant surface. The peak of the maximum Reynolds stress is normally located near the wall [56], such that $\tau_w \approx -\rho\langle u'v'\rangle|_{max}$. The maximum Reynolds stress $-\rho\langle u'v'\rangle|_{max}$ agrees very well with the estimated wall shear stress τ_κ (Table 5.8).

The dimensionless turbulent stress profiles $\langle u'^2\rangle$, $\langle v'^2\rangle$ and $\langle u'v'\rangle$ are presented in Figure 5.41 for bulk velocities $U_b = 3.5$ m/s (left) and $U_b = 5.2$ m/s (right). Turbulent stress components are scaled with the friction velocity of the rigid smooth plate $u_{\tau,0}$. The random error for the estimated displacement is typically ~0.1-0.2px for PIV and ~0.3px for PTV, resulting in a sufficient accurate streamwise velocity u as the displace-

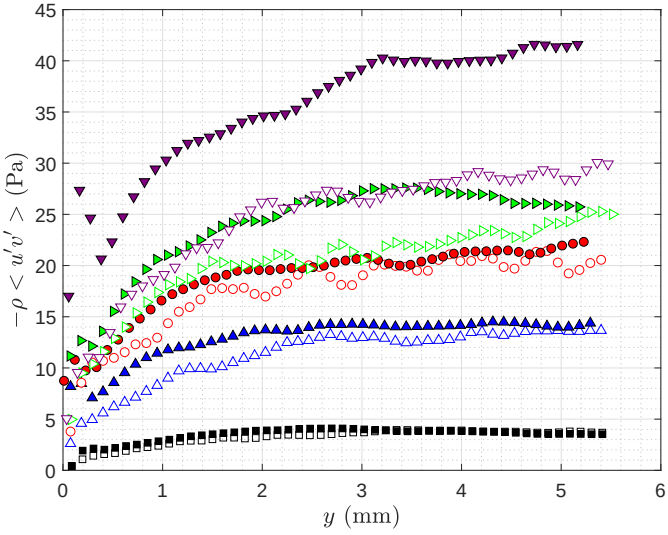

Figure 5.40: Reynolds stress $-\rho\langle u'v'\rangle$ for bulk velocities $U_b = 1.7$ m/s (□ symbols), $U_b = 3.5$ m/s (△ symbols), $U_b = 4.4$ m/s (○ symbols), $U_b = 4.8$ m/s (▷ symbols) and $U_b = 5.2$ m/s (▽ symbols). The open symbols represent the rigid smooth plate and closed symbols are the compliant coating plate.

Table 5.8: Local wall shear stress τ_w are estimated by the log-fit method (τ_κ) and by Reynolds decomposition (τ_{Rey}) for the smooth flat plate and the coated plate. The shear stress τ_{Rey} is approximately equal to the maximum of $-\rho\langle u'v'\rangle$, such that $\tau_w \approx -\rho\langle u'v'\rangle|_{max}$.

U_b (m/s)		τ_κ (Pa)	τ_{Rey} (Pa)
1.7	smooth	4.02	3.95
	coating	4.45	4.10
3.5	smooth	14.82	13.67
	coating	15.70	14.50
4.4	smooth	22.30	21.37
	coating	23.61	22.26
4.8	smooth	26.81	25.28
	coating	30.06	27.56
5.2	smooth	33.73	30.07
	coating	44.03	41.61

ment in the streamwise direction is in the order of 2-8 pixels. The displacement in the wall-normal direction is less than 0.5 pixel, which makes the random error proportional to the displacement and leads to inaccurate estimation of the wall-normal velocity v. Therefore, the PTV results are only applied for the estimation of the turbulent stress component $\left\langle u'^2 \right\rangle$ (Fig. 5.42), and not for $\left\langle v'^2 \right\rangle$ and $\langle u'v' \rangle$.

In general, the main observations can be summarized as follows:
Close to the wall, the two plates show a distinct peak in the $\left\langle u'^2 \right\rangle$-profile, where the peak value of the coated plate is larger than the peak value of the rigid smooth plate. For the smooth plate, the peak is around a wall-normal position $y^+ = 15-20$, as expected (Fig. 5.42a). For the coated plate, this peak moves away from the wall with an increasing bulk velocity (Fig. 5.42b), which is associated with an increase in the 'dynamic surface roughness' of the wall.
Further away from the wall, in the log-region, the turbulent statistics of the two plates are similar for the pre-transition bulk velocities $U_b < 4.5$ m/s. The wall fluctuations do not disturb the flow motions in this region. However, for the post-transition bulk velocities $U_b > 4.5$ m/s, the $\left\langle v'^2 \right\rangle$-profile is affected across the whole log-region. The wall-normal fluid motions and velocity fluctuations are most likely due to the corrugated surface of the coating as well as the presence of significant dynamic wall motions in the wall-normal direction $v_c = \partial\zeta/\partial t$ (related to Figure 5.37). The Reynolds stress $\langle u'v' \rangle$ is enhanced by the surface waves and increases with the same order of magnitude as the measured skin-friction.

WAVE PHASE SHIFT

The visual appearance of the waves and the large increase of friction and Reynolds stresses indicate a substantial fluid-surface interaction at a bulk velocity beyond $U_b \sim 4.5$ m/s. In order to separate the turbulent and the wave-induced fluid motions, the velocity decomposition receives an additional term: the wave-induced velocity $\widetilde{u}$ [75, 76].

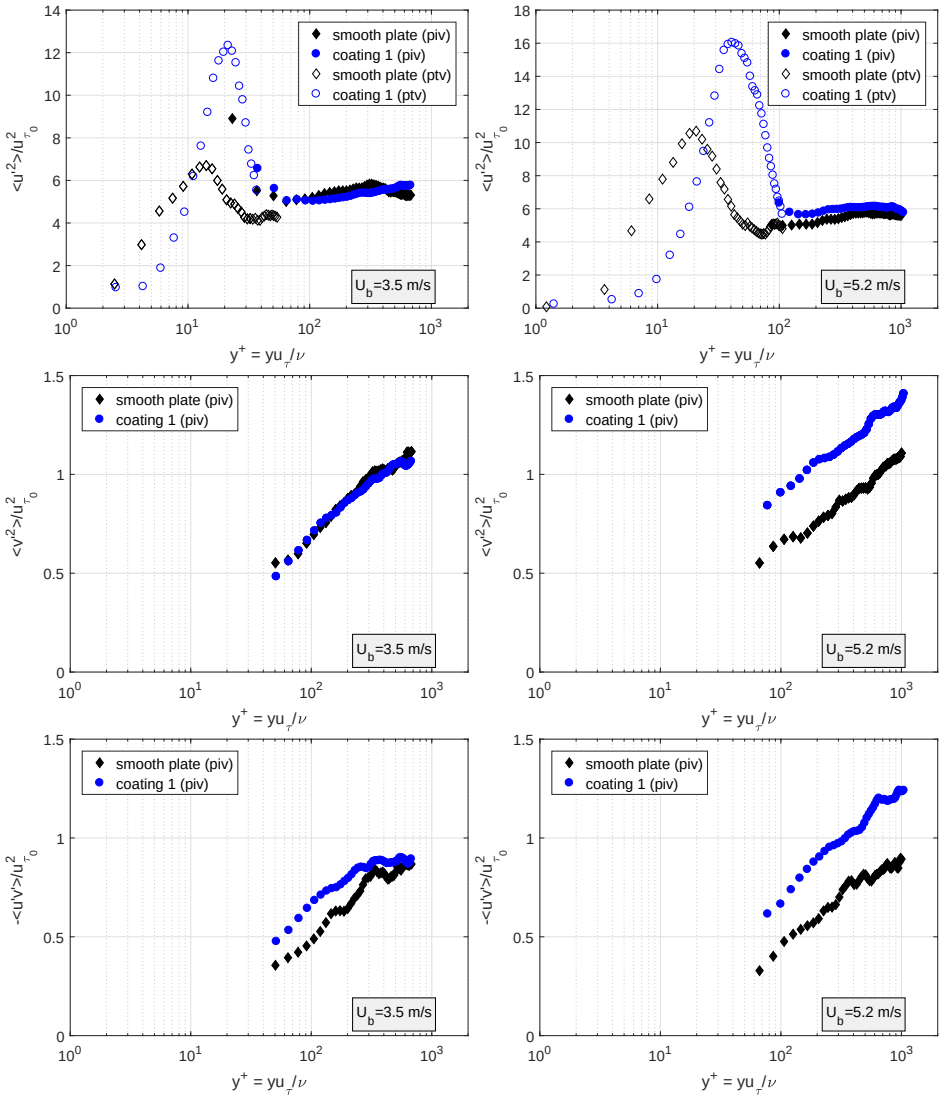

Figure 5.41: Dimensionless turbulent stress profiles $\langle u'^2 \rangle$ (top), $\langle v'^2 \rangle$ (middle) and $\langle u'v' \rangle$ (bottom) for bulk velocities $U_b = 3.5$ m/s (left) and $U_b = 5.2$ m/s (right). The PTV results are also applied for the estimation of the turbulent stress component $\langle u'^2 \rangle$ (open symbols).

The measured velocity components u and v are now decomposed into three parts:

$$u = \bar{u} + \tilde{u} + u' \tag{5.18}$$

and

$$v = \bar{v} + \tilde{v} + v' \tag{5.19}$$

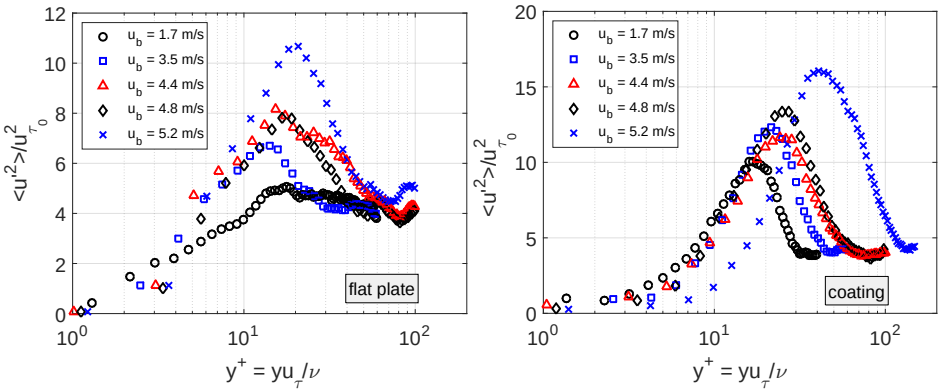

Figure 5.42: Dimensionless turbulent stress profiles $\langle u'^2 \rangle$ reconstructed from the PTV results for bulk velocities U_b = 1.7 - 3.5 - 4.4 - 4.8 and 5.2 m/s. Left: flat smooth plate. Right: coated plate.

5

The PIV measurements are performed in a fixed reference frame with respect to the tunnel, which means that the coating surface waves propagate through the field of view (FOV). Phase-averaging can determine the influence of the wave-phase and the wave-amplitude on the fluid motions and quantities. The coating surface waves suffer from the phase differences in the fixed FOV, which are nullified by the phase-shift of the instantaneous velocity field with the corresponding wave, such that the waves are all in-phase. The phase-shift is based on the period identification of the surface wave crest. In the present field of view, a wave crest is defined as the part of the coating surface that protrudes into the fluid flow. For the post-transition bulk velocities $U_b > 4.5$ m/s, the characteristic wave lengths of the dominant waves are around $\lambda_x \sim 9$ mm (Fig. 5.29). The characteristic wavelength is similar to the width of the FOV (~ 8.7 mm). Therefore, phase-shifting and image-stitching have been applied to obtain a qualitative phase-averaged velocity field, although this procedure is somewhat arbitrary.
Phase-shifting and image-stitching lead to discontinuities and anomalous jumps in the instantaneous velocity fields, which fade in the mean value when sufficient number of the instantaneous velocity fields is averaged. In order to compare the influence of the wall deformation amplitude on the fluid motions, two wave amplitude categories are appointed that contains a high amount of instantaneous velocity fields with significant surface wave amplitude, namely group 1: $A_c = 0.1 - 0.2$ mm with 135 images (i.e. $A_c^+ = 18 - 36$) and group 2: $A_c = 0.2 - 0.4$ mm with 105 images (i.e. $A_c^+ = 36 - 72$). Within these two wave amplitude categories, the phase-averaged velocities $\langle u \rangle_\theta$ and $\langle v \rangle_\theta$ are realized after phase-shifting and image-stitching of the relevant instantaneous velocity fields. Subsequently, the wave-induced velocity fields are obtained by $\tilde{u} = \langle u \rangle_\theta - \bar{u}$ and $\tilde{v} = \langle v \rangle_\theta - \bar{v}$ and are presented in Figure 5.43 and 5.44, respectively. The presented surface interface corresponds to the mean of the relevant surface waves after phase-shifting and image-stitching within one wave amplitude category. The wave-induced velocity fields $\tilde{u}$ and $\tilde{v}$ are made dimensionless with the dominant wave frequency f times the averaged wave crest amplitude $\bar{A}_c$. The dominant wave frequency f was determined from the displacement spectrum of the BOS results and equals $f = 96$ Hz for

both amplitude categories. The averaged wave crest amplitude $\bar{A}_c$ of the two amplitude categories are $\bar{A}_c = 0.15$ mm for group 1 (i.e. $\bar{A}_c^+ = 26$) and $\bar{A}_c = 0.27$ mm for group 2 (i.e. $\bar{A}_c^+ = 48$). The wave-induced velocity fields define a classical phenomenon of a turbulent boundary layer flow over a rigid wavy surface [77, 78]; the boundary layer upstream of the wave crest is influenced by the local acceleration of the flow, leading to a favourable pressure gradient. Downstream of the wave crest, the fluid near the wall starts to decelerate (i.e. adverse pressure gradient), leading to flow instabilities that amplifies mixing, resulting in larger local Reynolds stress. The surface wave induces strong fluid motions in wall-normal direction (Fig. 5.44).
It is noticed that the shape of the wave is asymmetric, which was also identified from the results of the BOS measurements. The crest is shorter and higher, which results in a steeper local slope of the crest that enhances the fluid motions. Therefore, the positive streamwise velocity under the crest is stronger than the negative streamwise velocity under the valley. The main difference between the two amplitude categories is the location of the positive and the negative velocity regions and their maxima. For amplitude group 1 ($\bar{A}_c^+ = 26$), the region is located exactly under the crest and valley, which corresponds to a linear response of the fluid motions to the surface wave. The wave-induced streamwise velocity field $\widetilde{u}$ of amplitude group 2 ($\bar{A}_c^+ = 48$) shows a small upstream shift of this region, which indicates a separation of the boundary layer behind the crest. This results in a non-linear behavior of the fluid motions in contrast to the surface wave, which seems plausible since $\bar{A}_c^+ \geqslant 27$ [77, 79, 80]. The indication of the boundary layer separation and the non-linear behavior is supported by the observation of a small downstream shift of the '$\widetilde{v} = 0$'-location (valley) at the coating-fluid interface (Fig. 5.44).

It can be concluded that the wave-induced velocities $\widetilde{u}$ and $\widetilde{v}$ are defined by and scales with the surface wave amplitude A of deformation. The wave has an apparent behavior to influence the velocity field like a rigid wavy wall, since the wave propagation velocity is considerably lower than the bulk velocity U_b, which was determined by the BOS surface deformation measurements.

5.4. SUMMARY AND CONCLUSION

The interaction of three compliant coatings with a turbulent boundary layer were investigated, such that the surface wave was characterized as a function of the coating properties and the bulk velocity $\bar{U}_b$.
Drag force measurements indicated that all three coatings behave like a smooth surface for low bulk velocities $\bar{U}_b$. However, the softest coating 1 ($|G^*| \sim 1.5$ kPa) starts to deviate from $\bar{U}_b \simeq 4.5$ m/s and above, as the shear stress $\bar{\tau}$ increases significantly. The flow experienced an additional drag due to flow-induced surface waves with high amplitude at the interface of coating 1, which has been confirmed by the BOS measurements. The dynamic roughness of the wavy surface was estimated based on the 'equivalent sandgrain roughness' of Nikuradse [47] $k_s = f(Re_L, C_d)$. The surface roughness k_s was around $k_s = 40$ μm at $\bar{U}_{b,trans} = 4.5$ m/s and $k_s = 130$ μm at $\bar{U}_b = 5.5$ m/s. The stiffer coating 2 ($|G^*| \sim 6.0$ kPa) and coating 3 ($|G^*| \sim 14$ kPa) maintained their

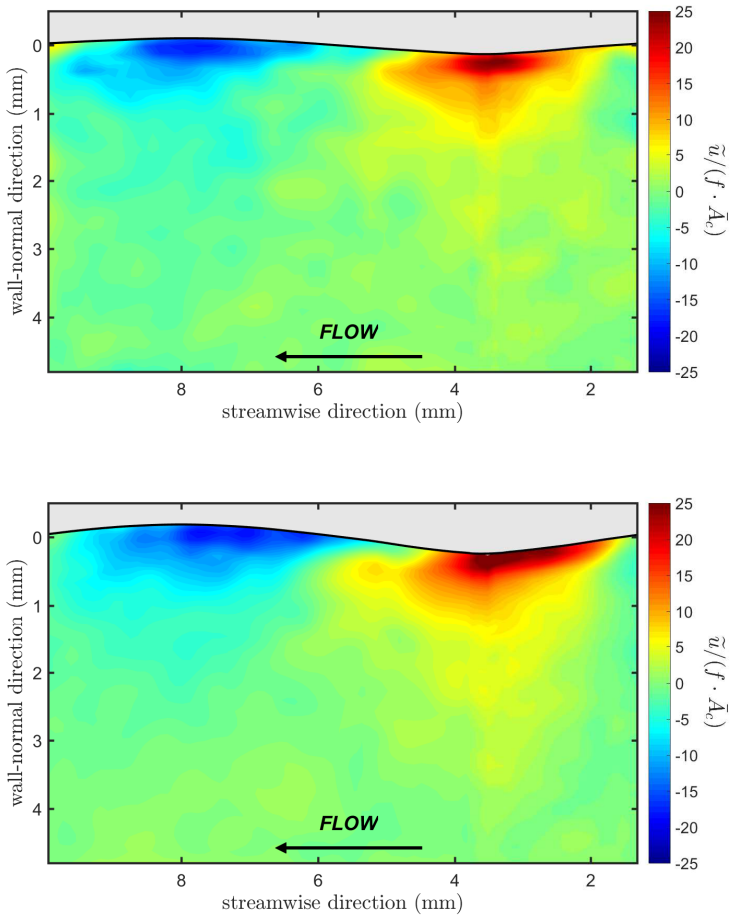

Figure 5.43: Streamwise wave-induced velocity field $\tilde{u}$ at bulk velocity U_b = 5.2 m/s of a) group 1, wave amplitude $A_c = 0.1 - 0.2$ mm and b) group 2, wave amplitude $A_c = 0.2 - 0.4$ mm.

smooth surface behavior up till the maximum available tunnel velocity $\bar{U}_b = 5.5$ m/s. The surface deformation measurements verified symmetric traveling waves for all three coatings and they followed the direction of the fluid flow. The wave propagation velocity was $c_w = 0.70 - 0.80\ \bar{U}_b$, which suggests strong correlation with high-intensity turbulent pressure fluctuations in the turbulent boundary layer. This hypothesis is supported by the scaling of the rms-values of the surface deformations ζ_{rms} with the ratio of pressure fluctuations to coating shear modulus $p_{rms}/|G^*|$ (Fig. 5.17b). A transition in the surface deformation has been observed for coating 1 at $\bar{U}_{b,trans} = 4.5$ m/s when additional wave-trains protrude the viscous sublayer and start to dominate the surface incrementally with an increasing bulk velocity. The shape of these waves were asym-

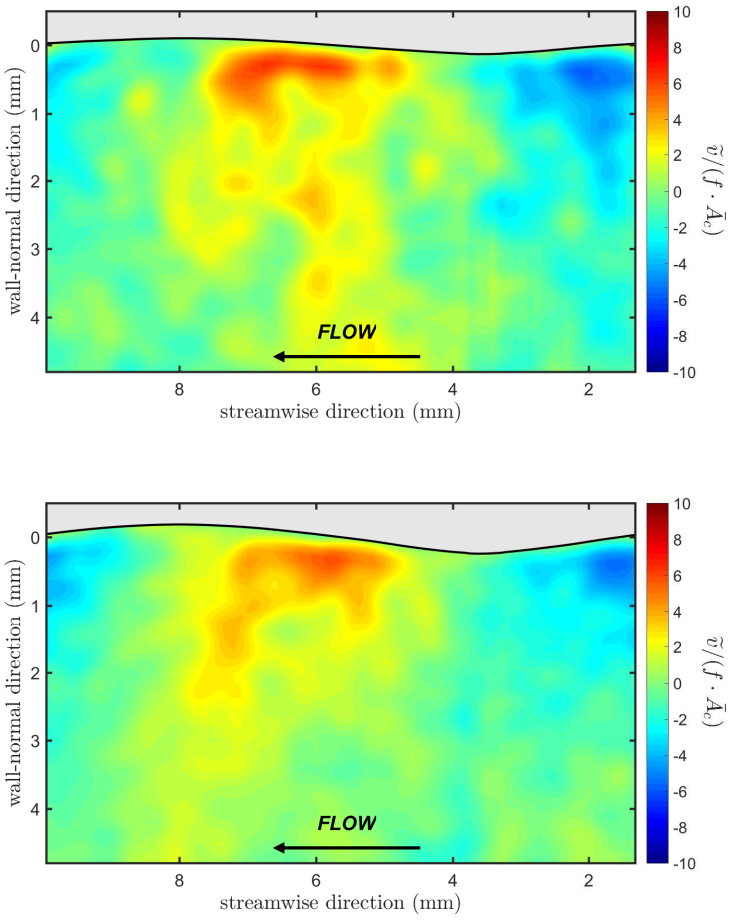

Figure 5.44: Wall-normal wave-induced velocity field $\tilde{v}$ at bulk velocity U_b = 5.2 m/s of a) group 1, wave amplitude $A_c = 0.1 - 0.2$ mm and b) group 2, wave amplitude $A_c = 0.2 - 0.4$ mm.

metric, with higher and shorter crests than the valleys. The wave-trains have a propagation velocity of around c_w = 0.17-0.18 $\bar{U}_b$ and is considered to be determined by the complex wave dynamics of the visco-elastic material. Height-time diagrams and time-series visualizations indicated modulation of the wave-train by the fast-moving low-amplitude waves related to the pressure fluctuations.

PIV measurements were done on the turbulent flow along the surface of coating 1. The mean velocity profiles indicate a change in the very near-wall region for all bulk velocities. Beyond the transition velocity $\bar{U}_{b,trans}$ = 4.5 m/s, the velocity profile shows a downward shift Δu^+ in the log region, which is associated with drag increase due to surface roughness. The downward shift Δu^+ is associated with an apparent roughness

k_s, which corresponds very well with the estimated values from the drag force measurements. Significant wall motions (i.e. $v_c = \partial\zeta/\partial t$) enhance the fluid motions and provides a linear correlation for the observed downward shift Δu^+. The wave-induced velocity fields showed local acceleration and deceleration of the fluid in the streamwise direction at the surface crest and the valley respectively, and defines the classical phenomenon of a turbulent boundary layer flow over a rigid wavy surface. Furthermore, strong surface deformation ($A^+ > 27$) resulted in a boundary layer separation behind the crest that leads to non-linear behavior of the fluid motions.

In conclusion, the large scale turbulent structures initiate moderate deformation of the coating surface, while the fluid flow remains nearly undisturbed. This is the so-called one-way coupled regime. However, in the case of coating 1, the undulations start to protrude the viscous sublayer when the bulk velocity increase beyond $\bar{U}_{b,trans} > 4.5$ m/s. The flow is capable of transferring sufficient energy towards the coating and initiating a wave-train with a significant wave-amplitude that is defined by the material properties of the visco-elastic coating. A two-way coupled regime arises as the wave-train induces extra fluid motions and increases the Reynolds stresses. In the current study, the observations show no capability to reduce turbulent drag with this type of visco-elastic compliant coating.

REFERENCES

[1] M. O. Kramer, *Boundary-layer stabilization by distributed damping,* Journal of the Aeronautical Sciences **24**, 459 (1957).

[2] M. O. Kramer, *Boundary layer stabilization by distributed damping,* Naval Engineers Journal **74**, 341 (1962).

[3] D. M. Bushnell, J. N. Hefner, and R. L. Ash, *Effect of compliant wall motion on turbulent boundary layers,* The Physics of Fluids **20**, S31 (1977).

[4] J. J. Riley, M. Gad-el Hak, and R. W. Metcalfe, *Complaint coatings,* Annual Review of Fluid Mechanics **20**, 393 (1988).

[5] M. Gad-el Hak, *Compliant coatings for drag reduction,* Progress in Aerospace Sciences **38**, 77 (2002).

[6] S. K. Robinson, *Coherent motions in the turbulent boundary layer,* Annual Review of Fluid Mechanics **23**, 601 (1991).

[7] H. Tennekes and J. L. Lumley, *A first course in turbulence* (MIT press, 1972).

[8] V. M. Kulik, S. V. Rodyakin, S.-B. Suh, I. Lee, and H. Chun, *The response of compliant coating to nonstationary disturbances,* Physics of Fluids **17**, 088104 (2005).

[9] J. H. Duncan, *The response of an incompressible, viscoelastic coating to pressure fluctuations in a turbulent boundary layer,* Journal of Fluid Mechanics **171**, 339 (1986).

[10] H. Benschop, A. Greidanus, R. Delfos, J. Westerweel, and W.-P. Breugem, *Deformation of a linear viscoelastic compliant coating in a turbulent flow,* Journal of Fluid Mechanics **859**, 613 (2019).

[11] M. Gad-El-Hak, R. F. Blackwelder, and J. J. Riley, *On the interaction of compliant coatings with boundary-layer flows,* Journal of Fluid Mechanics **140**, 257 (1984).

[12] M. Gad-el Hak, *Boundary layer interactions with compliant coatings: an overview,* Appl. Mech. Rev **39**, 511 (1986).

[13] P. Carpenter and A. Garrad, *The hydrodynamic stability of flow over kramer-type compliant surfaces. part 2. flow-induced surface instabilities,* Journal of Fluid Mechanics **170**, 199 (1986).

[14] R. Hansen and D. Hunston, *An experimental study of turbulent flows over compliant surfaces,* Journal of Sound and Vibration **34**, 297IN1 (1974).

[15] R. Hansen, D. Hunston, C. Ni, and M. Reischman, *An experimental study of flow-generated waves on a flexible surface,* Journal of Sound and Vibration **68**, 317 (1980).

[16] J. McMichael, P. Klebanoff, and N. Mease, *Experimental investigation of drag on a compliant surface,* Progress in Astronautics and Aeronautics **72**, 410 (1980).

[17] R. Hansen and D. Hunston, *Fluid-property effects on flow-generated waves on a compliant surface,* Journal of Fluid Mechanics **133**, 161 (1983).

[18] D. Hess, R. Peattie, and W. Schwarz, *A noninvasive method for the measurement of flow-induced surface displacement of a compliant surface,* Experiments in fluids **14**, 78 (1993).

[19] T. Lee, M. Fisher, and W. Schwarz, *Investigation of the stable interaction of a passive compliant surface with a turbulent boundary layer,* Journal of Fluid Mechanics **257**, 373 (1993).

[20] T. Lee, M. Fisher, and W. Schwarz, *The measurement of flow-induced surface displacement on a compliant surface by optical holographic interferometry,* Experiments in fluids **14**, 159 (1993).

[21] T. Lee, M. Fisher, and W. Schwarz, *Investigation of the effects of a compliant surface on boundary-layer stability,* Journal of Fluid Mechanics **288**, 37 (1995).

[22] C. Zhang, R. Miorini, and J. Katz, *Integrating mach–zehnder interferometry with tpiv to measure the time-resolved deformation of a compliant wall along with the 3d velocity field in a turbulent channel flow,* Experiments in Fluids **56**, 203 (2015).

[23] C. Zhang, J. Wang, W. Blake, and J. Katz, *Deformation of a compliant wall in a turbulent channel flow,* Journal of Fluid Mechanics **823**, 345 (2017).

[24] O. Zverkhovskyi, *Ship drag reduction by air cavities*, Ph.D. thesis, Delft University of Technology (2014).

[25] F. Moisy, M. Rabaud, and K. Salsac, *A synthetic schlieren method for the measurement of the topography of a liquid interface,* Experiments in Fluids **46**, 1021 (2009).

[26] F. Moisy, G.-J. Michon, M. Rabaud, and E. Sultan, *Cross-waves induced by the vertical oscillation of a fully immersed vertical plate,* Physics of Fluids **24**, 022110 (2012).

[27] A. Paquier, F. Moisy, and M. Rabaud, *Surface deformations and wave generation by wind blowing over a viscous liquid,* Physics of Fluids **27**, 122103 (2015).

[28] H. Richard and M. Raffel, *Principle and applications of the background oriented schlieren (bos) method,* Measurement Science and Technology **12**, 1576 (2001).

[29] M. Raffel, *Background-oriented schlieren (bos) techniques,* Experiments in Fluids **56**, 60 (2015).

[30] E.-J. Foeth, *The structure of three-dimensional sheet cavitation*, Ph.D. thesis, Delft University of Technology (2008).

[31] P. Pennings, *Dynamics of Vortex Cavitation*, Ph.D. thesis, Delft University of Technology (2016).

[32] K.-S. Choi, X. Yang, B. Clayton, E. Glover, M. Atlar, B. Semenov, and V. Kulik, *Turbulent drag reduction using compliant surfaces,* in *Proceedings of the Royal Society of London A: Mathematical, Physical and Engineering Sciences*, Vol. 453 (The Royal Society, 1997) pp. 2229–2240.

[33] A. Colley, P. Thomas, P. Carpenter, and A. Cooper, *An experimental study of boundary-layer transition over a rotating, compliant disk,* Physics of Fluids **11**, 3340 (1999).

[34] P. Bandyopadhyay, C. Henoch, J. Hrubes, B. Semenov, A. Amirov, V. Kulik, A. Malyuga, K.-S. Choi, and M. Escudier, *Experiments on the effects of aging on compliant coating drag reduction,* Physics of Fluids **17**, 085104 (2005).

[35] A. V. Boiko, V. M. Kulik, H.-H. Chun, and I. Lee, *Verification of drag-reduction capabilities of stiff compliant coatings in air flow at moderate speeds,* International Journal of Naval Architecture and Ocean Engineering **3**, 242 (2011).

[36] J. H. Laurer, R. Bukovnik, and R. J. Spontak, *Morphological characteristics of sebs thermoplastic elastomer gels,* Macromolecules **29**, 5760 (1996).

[37] T. Dürrschmidt and H. Hoffmann, *Organogels from aba triblock copolymers,* Colloid and Polymer Science **279**, 1005 (2001).

[38] G. Lattermann and M. Krekhova, *Thermoreversible ferrogels,* Macromolecular rapid communications **27**, 1373 (2006).

[39] J. K. Kim, M. A. Paglicawan, and M. Balasubramanian, *Viscoelastic and gelation studies of sebs thermoplastic elastomer in different hydrocarbon oils,* Macromolecular research **14**, 365 (2006).

[40] J. H. Laurer, J. F. Mulling, S. A. Khan, R. J. Spontak, and R. Bukovnik, *Thermoplastic elastomer gels. i. effects of composition and processing on morphology and gel behavior,* Journal of Polymer Science Part B: Polymer Physics **36**, 2379 (1998).

[41] F. C. Elwell, *Flushing of embayments*, Ph.D. thesis, University of Cambridge (2005).

[42] R. J. Adrian, *Particle-imaging techniques for experimental fluid mechanics,* Annual review of fluid mechanics **23**, 261 (1991).

[43] R. J. Adrian and J. Westerweel, *Particle image velocimetry*, 30 (Cambridge University Press, 2011).

[44] J. Westerweel and F. Scarano, *Universal outlier detection for piv data,* Experiments in fluids **39**, 1096 (2005).

[45] F. Charruault, A. Greidanus, W.-P. Breugem, and J. Westerweel, *A dot tracking algorithm to measure free surface deformations,* in *Proceedings 18th International Symposium on Flow Visualization* (ETH Zurich, 2018).

[46] R. Keane, R. Adrian, and Y. Zhang, *Super-resolution particle imaging velocimetry,* Measurement Science and Technology **6**, 754 (1995).

[47] J. Nikuradse, *Laws of flow in rough pipes,* in *VDI Forschungsheft* (Citeseer, 1933).

[48] P. Bradshaw, *A note on critical roughness height and transitional roughness,* Physics of Fluids **12**, 1611 (2000).

[49] F. M. White, *Fluid mechanics* (WCB, 1999).

[50] J. Duncan, A. Waxman, and M. Tulin, *The dynamics of waves at the interface between a viscoelastic coating and a fluid flow,* Journal of Fluid Mechanics **158**, 177 (1985).

[51] M. Goody, *An empirical spectral model of surface-pressure fluctuations that includes reynolds number effects,* in *8th AIAA/CEAS Aeroacoustics Conference & Exhibit* (2002) p. 2565.

[52] M. Goody, *Empirical spectral model of surface pressure fluctuations,* AIAA journal **42**, 1788 (2004).

[53] W. Willmarth, *Structure of turbulence in boundary layers,* Advances in applied mechanics **15**, 159 (1975).

[54] F. H. Clauser, *The turbulent boundary layer,* in *Advances in applied mechanics*, Vol. 4 (Elsevier, 1956) pp. 1–51.

[55] T. Wei, R. Schmidt, and P. McMurtry, *Comment on the clauser chart method for determining the friction velocity,* Experiments in fluids **38**, 695 (2005).

[56] S. B. Pope, *Turbulent flows,* (2001).

[57] M. Shockling, J. Allen, and A. Smits, *Roughness effects in turbulent pipe flow,* Journal of Fluid Mechanics **564**, 267 (2006).

[58] M. Schultz and K. Flack, *The rough-wall turbulent boundary layer from the hydraulically smooth to the fully rough regime,* Journal of Fluid Mechanics **580**, 381 (2007).

[59] L. I. Langelandsvik, G. J. Kunkel, and A. l. J. Smits, *Flow in a commercial steel pipe,* Journal of Fluid Mechanics **595**, 323 (2008).

[60] E. Napoli, V. Armenio, and M. De Marchis, *The effect of the slope of irregularly distributed roughness elements on turbulent wall-bounded flows,* Journal of Fluid Mechanics **613**, 385 (2008).

[61] M. P. Schultz and K. A. Flack, *Turbulent boundary layers on a systematically varied rough wall,* Physics of Fluids **21**, 015104 (2009).

[62] J. Yuan and U. Piomelli, *Estimation and prediction of the roughness function on realistic surfaces,* Journal of Turbulence **15**, 350 (2014).

[63] H. Cheng and I. P. Castro, *Near wall flow over urban-like roughness,* Boundary-Layer Meteorology **104**, 229 (2002).

[64] P. Orlandi, S. Leonardi, and R. Antonia, *Turbulent channel flow with either transverse or longitudinal roughness elements on one wall,* Journal of Fluid Mechanics **561**, 279 (2006).

[65] P. Orlandi and S. Leonardi, *Direct numerical simulation of three-dimensional turbulent rough channels: parameterization and flow physics,* Journal of Fluid Mechanics **606**, 399 (2008).

[66] F. T. M. Nieuwstadt, J. Westerweel, and B. J. Boersma, *Turbulence: introduction to theory and applications of turbulent flows* (Springer, 2016).

[67] P. Saarenrinne and M. Piirto, *Turbulent kinetic energy dissipation rate estimation from piv velocity vector fields,* Experiments in Fluids **29**, S300 (2000).

[68] S. Tokgoz, G. E. Elsinga, R. Delfos, and J. Westerweel, *Spatial resolution and dissipation rate estimation in taylor–couette flow for tomographic piv,* Experiments in fluids **53**, 561 (2012).

[69] K. Sharp and R. Adrian, *Piv study of small-scale flow structure around a rushton turbine,* AIChE Journal **47**, 766 (2001).

[70] J. Sheng, H. Meng, and R. Fox, *A large eddy piv method for turbulence dissipation rate estimation,* Chemical engineering science **55**, 4423 (2000).

[71] J. Smagorinsky, *General circulation experiments with the primitive equations: I. the basic experiment,* Monthly weather review **91**, 99 (1963).

[72] F. R. Khan, *Investigation of turbulent flows and instabilities in a stirred vessel using particle image velocimetry*, Ph.D. thesis, © FR Khan (2005).

[73] A. Gabriele, A. Nienow, and M. Simmons, *Use of angle resolved piv to estimate local specific energy dissipation rates for up-and down-pumping pitched blade agitators in a stirred tank,* Chemical Engineering Science **64**, 126 (2009).

[74] J. Meyers and P. Sagaut, *On the model coefficients for the standard and the variational multi-scale smagorinsky model,* Journal of Fluid Mechanics **569**, 287 (2006).

[75] A. K. M. F. Hussain and W. C. Reynolds, *The mechanics of an organized wave in turbulent shear flow,* Journal of Fluid Mechanics **41**, 241 (1970).

[76] M. Birvalski, M. Tummers, R. Delfos, and R. Henkes, *Piv measurements of waves and turbulence in stratified horizontal two-phase pipe flow,* International Journal of Multiphase Flow **62**, 161 (2014).

[77] J. Hudson, L. Dykhno, and T. Hanratty, *Turbulence production in flow over a wavy wall,* Experiments in Fluids **20**, 257 (1996).

[78] S. Belcher and J. Hunt, *Turbulent flow over hills and waves,* Annual Review of Fluid Mechanics **30**, 507 (1998).

[79] D. P. Zilker, G. W. Cook, and T. J. Hanratty, *Influence of the amplitude of a solid wavy wall on a turbulent flow. part 1. non-separated flows,* Journal of Fluid Mechanics **82**, 29 (1977).

[80] D. P. Zilker and T. J. Hanratty, *Influence of the amplitude of a solid wavy wall on a turbulent flow. part 2. separated flows,* Journal of Fluid Mechanics **90**, 257 (1979).

6

CLOSURE

Detailed conclusions and recommendations have been described in the separate chapters. This chapter provides a summary and general conclusion of the research performed, followed by the relevant perspectives and the remaining open questions.

6.1. SUMMARY & CONCLUSIONS

The main research concerns the study and the understanding of the interaction between non-smooth surfaces and a wall-bounded turbulent flow. The research was conducted in two parts, related to the experimental facility used in combination with the applied functional surface. The first part considers the turbulent flow in a Taylor-Couette setup and the application of a riblet surface. The second part describes the use of a water tunnel facility and the interaction between the compliant walls and a turbulent boundary layer flow. Force measurements indicated the amount of fluid shear stress acting on the surface of interest. Optical measurement techniques were adopted for both parts of the research to visualize and quantify the turbulent flow (PIV) and the compliant wall deformations (BOS).

6.1.1. TAYLOR-COUETTE SETUP & RIBLETS

The Taylor-Couette setup has proven to be an accurate and compact test-facility to measure and characterise the frictional resistance of surfaces under turbulent flow conditions. Nevertheless, specific artifacts of the TC-facility were taken into account when the setup is applied as a drag-measuring device.

The PIV measurements indicated the presence of different turbulent flow regimes ($Re_s >$ 400) under exact counter rotating conditions (R_Ω=0). The wall friction coefficient C_f was strongly influenced by the fluid motions related to these turbulent flow regimes and differs significantly from typical turbulent channel and pipe flows. The presence of large vortex-like structures completely disappeared for fully turbulent flows. Therefore, the derived data was limited to $Re_s > 10^4$ in order to make a suitable estimation of the drag performance of modified surfaces under general shear flows.

In this study, a riblet surface was applied on the inner cylinder, which reduced the total frictional drag by 5.3% at Reynolds number $Re_s = 4.7 \times 10^4$ under exact counter rotation. Under these conditions, the azimuthal velocity profile between the two rotating cylinders showed two differences compared to the velocity profile between two smooth-wall cylinders. First, the velocity gradient at the inner riblet-wall cylinder is significantly smaller indicative of the lower level of turbulence. Secondly, the bulk flow co-rotated slightly with the outer cylinder due to a lower total drag force at the inner cylinder riblet-wall. The small velocity shift in the azimuthal direction affects the net system rotation and induces a rotation effect. The rotation effect induces a rotational drag change that causes a part of the total measured drag change. The proposed "rotation effect" model, which is based on the angular momentum balance, makes use of the total measured drag change and estimates the velocity shift δ and corresponds very well with the reconstructed velocity shift obtained from the PIV measurements. In this way, the small shift in the bulk velocity quantifies the apparent rotation number $\hat{R}_\Omega$ that indicates the specific stand-alone rotational drag change.

Periodically driven Taylor-Couette flow was accomplished by modulating the veloc-

ity of the inner and outer cylinder as a sinusoidal function, such that the shear velocity between the two cylinders equals $U_{sh} = \langle U_{sh} \rangle - \Delta U_{sh} \sin(2\pi t/T)$ while maintaining $R_\Omega = 0$. Under these unsteady turbulent conditions, the main scaling parameters are the shear Reynolds number Re_s, the oscillation Reynolds number Re_{osc} and the Womersley number Wo, such that the required power to overcome the frictional drag becomes $\langle P_d \rangle = f(Re_s, Re_{osc}, Wo)$.

The results of the periodically driven experiments indicated that the very small velocity amplitudes $\mathscr{A} = Re_{osc}/Re_s \leq 0.05$ have a marginal impact on the drag change DC in contrast to the steady boundary conditions. The perturbations of these velocity amplitudes were considered to be smaller than the turbulent velocity fluctuations (i.e. $\Delta U_{sh} < u'$). Larger velocity amplitudes $\mathscr{A} = Re_{osc}/Re_s \geq 0.10$ induced a growth in the turbulent drag due to the additional turbulent fluctuations.

The total drag change DC as a function of periodically driven boundary conditions in contrast to the steady boundary conditions for the exact-counter rotating cylinders was given by $DC = \left(f(\mathscr{A}) + \mathscr{K}^* Wo^4 \mathscr{A}^2\right) - 1$, wherein the first term represents the analytical quasi-steady state solution with the accompanying velocity modulation, while the second term involves the magnitude of the boundary acceleration with the associated velocity fluctuation, where $\mathscr{K}^*$ is the conditional scaling-factor between the additional drag and the dimensionless acceleration.

The drag performance of riblets under periodically driven boundary conditions was evaluated and indicates that riblets are capable of reducing the frictional drag under small accelerations of the periodic driven boundaries. Nevertheless, the amount of drag reduction declines drastically when the boundary acceleration becomes more significant. Vigorous acceleration could even result in additional frictional drag when compared to a smooth surface.

6.1.2. WATER TUNNEL FACILITY & COMPLIANT COATINGS

The water tunnel and the related turbulent flow were characterized by both local and global measurements in order to quantify the accuracy and the proper usage of the test facility for frictional drag studies. The global flow velocity and the shear stress measurements showed only small fluctuations in the controlled bulk velocity U_b as well as the recorded friction-induced drag force F_d. These small fluctuations are related to characteristic features of the water tunnel, but had no anomalous effects on the results obtained.

The PIV measurements provided the local velocity profiles at three locations in the streamwise direction with the boundary layer growing in the same direction. A small acceleration of the flow was observed, but was considered to have no effect on the turbulent structures in the boundary layer as the acceleration parameter was small, $K < O(10^{-6})$. Furthermore, the turbulent flow was considered to be nearly isotropic with low turbulence intensity at the centerline of the water tunnel (i.e. $u_{rms} \cong v_{rms} \cong w_{rms}$).

The global force measurements quantified the overall plate shear stress and corresponded with the Grigson's empirical relation where $C_d = f(Re_L)$. Based on the local velocity profiles, the Clauser chart method showed to be a suitable procedure to quantify the local wall shear stress τ_w and accordingly the overall plate drag coefficient C_d.

The dynamic interaction between a compliant wall and the near-wall turbulent flow was indentified by applying compliant coatings, produced in-house, in the aforementioned water tunnel. The coating synthesis method made it possible to adjust the material properties, resulting in three coatings with different stiffnesses; coating 1: $|G^*| \sim 1.5$ kPa, coating 2: $|G^*| \sim 6.0$ kPa and coating 3: $|G^*| \sim 14$ kPa.

Two characteristic regimes of flow-surface interaction were determined; the one-way coupled regime and the two-way coupled regime. The one-way coupled regime occurs when the turbulent flow initiates moderate deformation of the coating surface, while the fluid flow itself remains undisturbed. For coating 1, this one-way coupled interaction was identified up till a bulk flow velocity $\bar{U}_b = 4.5$ m/s, while for coating 2 and 3 up till the maximum applied bulk velocity $\bar{U}_{b,max} = 5.5$ m/s. Under these conditions, the force and the PIV measurements had indicated similar shear stress values and flow behavior as for the rigid smooth surface, while the BOS reconstruction quantified measurable modulations of the coating surface. These surface modulations ζ are generally smaller than the viscous sublayer δ_v and scale with the turbulent pressure fluctuations over the coating shear modulus, i.e. $\zeta_{rms} \sim p_{rms}/|G^*|$. The characteristic wave propagation velocity was in the order of $c_w = 0.70 - 0.80\ \bar{U}_b$ and indicated strong correlation with the high-intensity turbulent pressure fluctuations in the turbulent boundary layer.

The two-way coupled regime was identified by substantial deformation of the coating surface accompanied by an enhanced turbulent flow activity. This regime was observed for coating 1 only, when the bulk velocity was $\bar{U}_b > 4.5$ m/s. The force measurements showed an increase in the shear stress in the two-way coupled regime. The PIV measurements confirmed the additional fluid motions (u', v') and the increase of the local Reynolds stresses. Furthermore, the velocity profile showed a downward shift Δu^+ in the log region, related to the drag increase due to the significant surface deformations.

The time-series visualizations of the surface deformation measurements showed wave-trains with significantly high amplitudes. The height-time diagrams suggested that these wave-trains were initiated by the original surface undulations caused by the large scale structures and associated pressure fluctuations in the turbulent boundary layer (i.e. one-way coupling). These initial surface undulations started to protrude the viscous sublayer, such that the turbulent flow was capable of transfering more energy towards the coating and initiated the wave-train with large wave-amplitudes. On their turn, these wave-trains induced the additional fluid motions in the turbulent flow. The propagation velocity of the wave-trains was $c_w = 0.17\text{-}0.18\ \bar{U}_b$ and incrementally dominated the coating surface with an increasing bulk velocity. The regime transition from 1-way to 2-way has been estimated to occur when the surface deformation fluctuation is around $\zeta_{rms} > \delta_v/2$. The turbulent flow along the slow-moving surface wave-trains resembled the classical phenomenon of a turbulent boundary layer flow over a rigid wavy surface, with local acceleration and deceleration of the fluid at the wave crest and at the valley, respectively. When the wave-trains started to dominate the coating surface, the wall-normal velocity component $\partial\zeta/\partial t$ provided the use of a linear correlation for the roughness function, which corresponded very well with the observed downward shift Δu^+. In contrast to Lee *et al.* [1], no frictional drag reduction under

turbulent flow conditions was found in this study with this type of compliant coatings.

6.2. OUTLOOK AND PERSPECTIVES

First of all, the goal of the present work was to elucidate the interaction of drag-modifying surfaces, in this case the riblets and the compliant coatings, with the accompanying turbulent flow. The findings of this study provided new knowledge and insights that can guide future research. Secondly, the experience obtained from this research may have additional value for the industry, regarding specific applications of the applied measurement techniques.

Recent fundamental research has established the use of the Taylor-Couette facility to study the effect of the drag reducing methods, such as air pockets, bubbles, polymers, liquid-infused surfaces and superhydrophobic coatings [2–5]. Additionally, the aviation [6] and the marine industries [7] have shown interest in using the TC system to study specific surface structures and coatings under turbulent flow conditions, which motivated the author to start a spin-off company called "flowmatters" [1].

Regarding the periodically driven turbulent flow, the scaling relation determined between the additional drag and the dimensionless acceleration was based on one shear velocity (i.e. Re_s) and a range of velocity amplitudes (i.e. Re_{osc}) and period times (i.e. Wo). These results should be considered as the preliminary direction to explore the consistancy of the relation between the frictional drag and the periodic turbulent flow conditions. The general next step is to extend the current study to a wider range of parametric flow conditions. Especially a wider range of the shear Reynolds number Re_s should elucidate the conditional scaling factor $\mathcal{K}^*$ dependency on Re_s. Furthermore, the operational conditions, such as the Rotation number (e.g. $-0.083 \leq R_\Omega \leq 0.091$), and the set-up geometry (e.g. radius ratio, gap size, aspect ratio) may influence the proposed scaling relation. It remains an open question if other drag-reducing methods effective under steady turbulent conditions will still succeed to reduce friction under periodic turbulent conditions, such as the applications of superhydrophobic surfaces, air bubbles/layers and polymers.

Many factors are still unclear regarding the interaction between the compliant material and the turbulent boundary layer flow, and these require additional investigations. In the present work, all the three coatings fit the scaling behavior in the one-way coupled regime, wherein the turbulent flow and the related surface-pressure fluctuations deform the compliant coating in proportion to the inverse of the coating stiffness, i.e. $\zeta_{rms}/h_c = 0.031 \cdot p_{rms}/|G^*|$. First, it is advised to determine the actual surface-pressure fluctuation p_{rms} in the near-wall region instead of using the estimated surface-pressure fluctuation based on the empirical pressure spectrum model of Goody [8, 9]. Secondly, the coating thickness h_c was chosen as a proper scaling parameter to normalise the surface deformation fluctuations ζ_{rms}, which could easily be clarified with additional deformation measurements using different coating thicknesses.

Open questions remain for the two-way coupled regime, as this was only observed for coating 1. The estimated 1-way/2-way transition can be rewritten as $0.031 \cdot h_c p_{rms}/|G^*| > \delta_v/2$, which gives direction to explore the two-way coupled regime in more details.

[1] www.flowmatters.nl

Both coating properties $|G^*|$ and h_c could be varied, as the water tunnel facility was already at the maximum bulk velocity (U_b ~5.6 m/s). This will elucidate how the complex wave dynamics of the compliant coating in the two-way coupled regime is related to the visco-elastic material properties.
An out-of-the-box challenging idea would be the application of magneto-responsive particles dispersed in the compliant material, such that the material stiffness $|G^*|$ can be modified in the presence of an external magnetic field [10]. In this way, the visco-elastic material behaviour can be determined by the imposed magnetic flux density.
Whitin this research, it is still not clear whether the compliant coatings have the capability to reduce frictional drag. It is suggested that the compliant wall may suppress the formation of new burst events in the near-wall turbulent flow after being triggered by an earlier bursting event [11]. Therefore, the research should focus on the favorable material properties (e.g. G' and $G"$), where the desired phase shift δ (with $\tan(\delta) = G"/G'$) is based on the energy-frequency spectrum of the turbulent flow.

Biofouling is considered to be the accumulation of micro-organisms on wetted surfaces that produce a matrix of extracellular polymeric substances (EPS), which mainly consist of polysaccharides, proteins, lipids and nucleic acids [12]. This matrix and the biofilm material properties are among others defined by the cross-linking density of the polymeric material. Furthermore, the biofilm response to fluid shear shows visco-elastic behaviour similar to the compliant material applied in this study [13]. These two similarities demonstrate the possibility of using these synthetic materials to investigate the frictional drag of biofouling on marine vessels in more detail.

The combination of the compliant coating and the optical measurement technique (BOS) in the present study can potentially be used as a non-intrusive measurement method to quantify the surface-pressure distribution on objects. In contrast to the pressure-sensitive paints (PSP) [14], which are effective measurement tools commonly used in aerodynamic research with high flow velocity, the pressure-sensitive coatings (PSC) are applicable in gas and liquid flow systems under a wide range of flow velocities. The new method quantifies the surface-pressure as a function of the coating modulations and the coating properties. The latter can be adapted to the turbulent flow conditions, such that the 1-way coupled regime is still valid. Specific flow phenomena (e.g. boundary layer separation, vortex shedding, etc), as well as the pressure distribution on an object (e.g. ship hull) can be determined from the local surface pressure measurement data and may contribute to specific design optimisation of objects under turbulent flow conditions. The novel pressure-sensitive coating (PSC) method described in this research work is patent pending.

REFERENCES

[1] T. Lee, M. Fisher, and W. Schwarz, *Investigation of the stable interaction of a passive compliant surface with a turbulent boundary layer,* Journal of Fluid Mechanics **257**, 373 (1993).

[2] R. A. Verschoof, D. Bakhuis, P. A. Bullee, S. G. Huisman, C. Sun, and D. Lohse, *Air cavities at the inner cylinder of turbulent taylor–couette flow,* International journal of multiphase flow **105**, 264 (2018).

[3] A. Varshney and V. Steinberg, *Drag enhancement and drag reduction in viscoelastic flow,* Physical Review Fluids **3**, 103302 (2018).

[4] T. Van Buren and A. J. Smits, *Substantial drag reduction in turbulent flow using liquid-infused surfaces,* Journal of Fluid Mechanics **827**, 448 (2017).

[5] S. Srinivasan, J. A. Kleingartner, J. B. Gilbert, R. E. Cohen, A. J. Milne, and G. H. McKinley, *Sustainable drag reduction in turbulent taylor-couette flows by depositing sprayable superhydrophobic surfaces,* Physical review letters **114**, 014501 (2015).

[6] P. A. Leitl, S. Kuntzagk, A. Flanschger, and K. Pfingsten, *Experimental and numerical investigation of the reduction in skin friction due to riblets applied on the surface of a taylor-couette cell,* in *AIAA Scitech 2019 Forum* (2019) p. 1625.

[7] H. Benschop, A. Guerin, A. Brinkmann, M. Dale, A. Finnie, W.-P. Breugem, A. Clare, D. Stübing, C. Price, and K. Reynolds, *Drag-reducing riblets with fouling-release properties: development and testing,* Biofouling **34**, 532 (2018).

[8] M. Goody, *An empirical spectral model of surface-pressure fluctuations that includes reynolds number effects,* in *8th AIAA/CEAS Aeroacoustics Conference & Exhibit* (2002) p. 2565.

[9] M. Goody, *Empirical spectral model of surface pressure fluctuations,* AIAA journal **42**, 1788 (2004).

[10] H. An, S. J. Picken, and E. Mendes, *Enhanced hardening of soft self-assembled copolymer gels under homogeneous magnetic fields,* Soft Matter **6**, 4497 (2010).

[11] D. M. Bushnell, J. N. Hefner, and R. L. Ash, *Effect of compliant wall motion on turbulent boundary layers,* The Physics of Fluids **20**, S31 (1977).

[12] H.-C. Flemming and J. Wingender, *The biofilm matrix,* Nature reviews microbiology **8**, 623 (2010).

[13] I. Klapper, C. J. Rupp, R. Cargo, B. Purvedorj, and P. Stoodley, *Viscoelastic fluid description of bacterial biofilm material properties,* Biotechnology and bioengineering **80**, 289 (2002).

[14] J. H. Bell, E. T. Schairer, L. A. Hand, and R. D. Mehta, *Surface pressure measurements using luminescent coatings,* Annual Review of Fluid Mechanics **33**, 155 (2001).

A

TAYLOR-COUETTE RELATED PARAMETERS, CONDITIONS & CORRECTIONS

This Appendix contains background information, results, observations and interpretation based on the present measurements [1] and earlier conducted investigations by Delfos *et al.* [2], Ravelet *et al.* [3] and Tokgöz [4] on the present TC facility.

A

A.1. FLOW STRUCTURES & VELOCITY PROFILES

Research on torque scaling identified the relation between the flow structures and measured shear stress [5–7]. For the current facility, Ravelet *et al.* [3] demonstrated strong dependency of the friction coefficient C_f on the Reynolds number Re_s (Eq. A.1) and the rotation number R_Ω (Eq. A.2), due to the change in turbulent flow structures and their interactions.

$$Re_s = \frac{2}{1+\eta}\left|\eta Re_o - Re_i\right| \tag{A.1}$$

$$R_\Omega = (1-\eta)\frac{Re_i + Re_o}{\eta Re_o - Re_i} \tag{A.2}$$

where η is the gap ratio between the inner and the outer cylinder, $\eta = r_i/r_o$.

The present investigation reproduced the results to gain more insight on the typical artifacts of Taylor-Couette shear flows with respect to the intended study of drag reducing methods. Torque measurements have demonstrated the relation between C_f and Re_s under several rotating conditions (Figure A.1). Tomo-PIV was used to reconstruct the 3D velocity fields and to identify the fluid motions in the radial gap under different rotation conditions (Figure A.2). A more detailed description on the tomo-PIV application to Taylor-Couette flow was given by Tokgöz [4].

Figure A.1 shows the relation between the friction coefficient C_f and shear Reynolds number Re_s for three relevant rotation conditions: inner rotation only ($R_\Omega = -0.083$), exact counter rotation ($R_\Omega = 0$) and outer rotation only ($R_\Omega = 0.091$). The turbulent shear stress values for inner rotation were significantly higher than for the counter and outer rotation, which could be attributed to the strong axial-positioned fluid motions in the axial and radial direction (Figure A.2a) that result into large-scale flow structures; the so-called counter-rotating pair of Taylor vortices (Figure A.2d). For inner cylinder rotation, the transition to a different regime was estimated to be around $Re_s = 140$. This corresponds very well with the critical Taylor number $Ta_c = 1700$ [9], which predicts the onset of instabilities due to the significant presence of centrifugal over viscous forces that leads to the growth of laminar Taylor vortices.
Under exact-counter rotation conditions, the friction curve collapses on the theoretical line of C_f-Re_s for laminar TC-flow. A transitional regime occurs from $Re_s = 400-4000$, where "Taylor-vortex"-like structures are dominating the fluid motions in the radial gap (see Chapter 2). The large vortical structures were completely dissolved when the flow became fully turbulent (Figure A.2d). Furthermore, the friction values C_f were nearly identical as for planar-Couette flow [8], except for the transition region due to the presence of the large vortical structures.

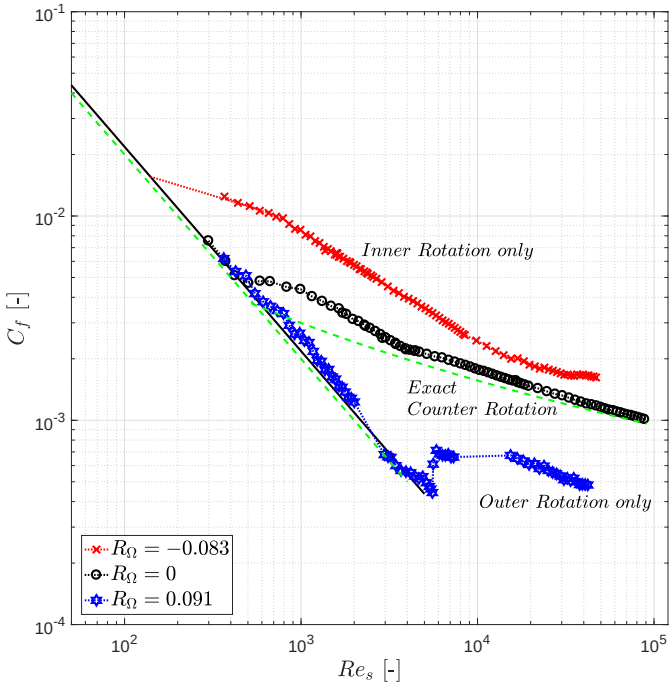

Figure A.1: Friction coefficient C_f as a function of Reynolds number Re_s for the present TC-facility, with gap ratio $\eta = r_i/r_o = 0.917$. Inner rotation only $R_\Omega = -0.083$ (red ×), exact-counter rotation $R_\Omega = 0$ (black ∘) and outer rotation only $R_\Omega = 0.091$ (blue ⋆). Solid black line represents the analytical laminar relation $2/\eta Re_s$, while the dashed green line indicates the data of plane-Couette flow [8].

When only the outer cylinder is rotating, the flow remains stable (i.e. laminar) untill $Re_s \simeq 5000$, from where it rapidly transits to a turbulent flow. The transition is considered to be caused by the end effects of the current facility, which induces a secondary flow in the axial direction (Figure A.2c).

The torque measurements indicate that the operational conditions strongly influence the formation of the turbulent flow structures present in the radial gap between the inner and the outer cylinders, which have partially been verified by the current tomo-PIV measurements. In Figure A.2d, the time-averaged velocity data indicate that the turbulent flow structures for inner cylinder rotation ($R_\Omega = -0.083$) deviate substantially from the other two rotation conditions (i.e. $R_\Omega = 0$ and $R_\Omega = 0.091$). Tokgöz [4] also observed that the large-scale Taylor-vortex structures starts to decay into smaller structures when the rotation number is increased from $R_\Omega = -0.083$ towards $R_\Omega = 0.091$. They stated, that the random organization of these smaller structures start to become dominant after $R_\Omega \geq -0.005$, and the azimuthal positions of these structures change spatially and are averaged-out in the mean velocity data. Consequently, no significant difference is noticeable between the counter and the outer rotation reconstructed time-averaged vorticity plots (Figure A.2d).
In order to better understand the flow dynamics, Tokgöz [4] studied the instantaneous

A

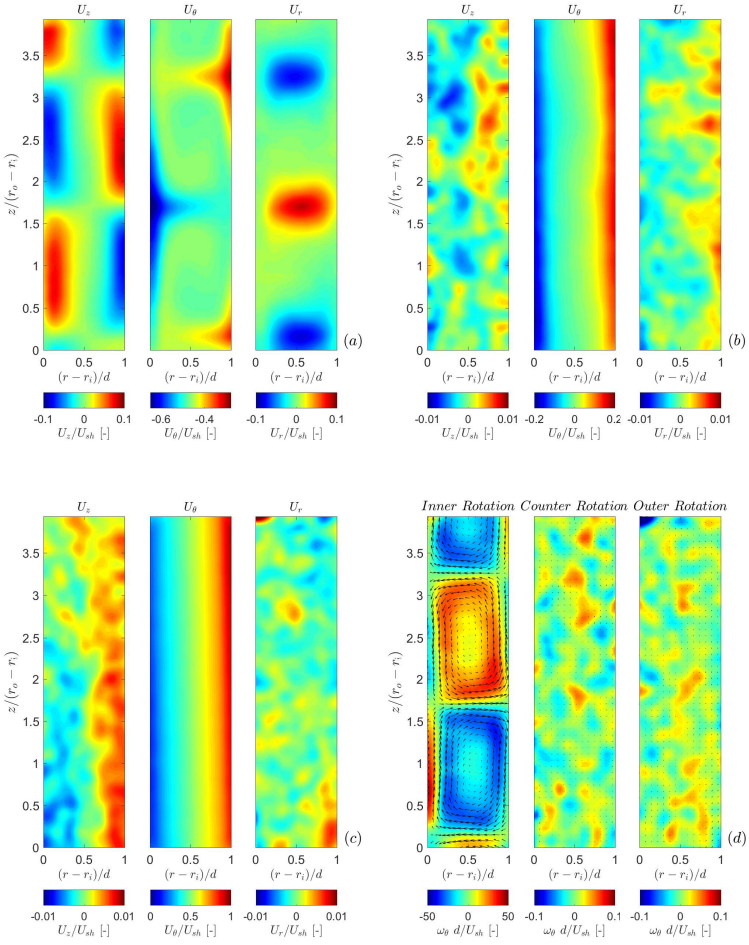

Figure A.2: Time-averaged normalised PIV results @ Reynolds number Re_s = 47000 for a) inner rotation $R_\Omega = -0.083$, b) exact-counter rotation $R_\Omega = 0$ and c) outer rotation $R_\Omega = 0.091$. The first panel indicates the axial velocity U_z, the second panel shows the azimuthal velocity U_θ, while the third panel presents the radial velocity U_r. d) Out-of-plane vorticity for the three rotation conditions; color indicates the normalized strength, arrows indicate the radial and axial velocities.

velocity data into further detail. An apparent change in the *size* and the *orientation* of the turbulent flow structures was observed with increasing rotation number ($R_\Omega = -0.083$ to $R_\Omega = 0.091$). At the inner rotation only with $R_\Omega = -0.083$, the flow structures were relatively large and elongated in the azimuthal direction with a minimal axial movement of these vortices in time. At the exact-counter rotation with $R_\Omega = 0$, the dimensions of the flow structures changed (i.e. they became smaller) and their orientation was more random. Finally, at the outer rotation only with $R_\Omega = 0.091$, the size of the coherent structures were similar as for $R_\Omega = 0$, with the structures primarily aligned

in the axial direction. It was suggested that these segmented Taylor column-like structures are connected to the earlier mentioned secondary fluid motions caused by the finite length of the cylinders with co-rotating end-plates.

To summarize, the size and the orientation of the turbulent flow structures were strongly related to the rotation condition, which in turn determine the shear stresses acting on the cylinder walls. Figure A.3 shows the relation between the friction coefficient C_f and the rotation number R_Ω at four different Reynolds numbers Re_s, equivalent to the graph reported by Ravelet *et al.* [3]. In general, the friction values C_f decreased with an increasing rotation number R_Ω, with an apparent linear decline around $R_\Omega = 0$. For low Reynolds number $Re_s = 1000$, the friction values C_f remained constant between $0.025 \geq R_\Omega \geq 0.091$, which are considered to be operating conditions to obtain laminar flow ($C_f \sim 2/\eta\ Re_s^{-1}$). For lower rotation numbers (i.e. $R_\Omega \leq 0.025$), flow disturbances instigate the laminar-turbulent transition and give rise to the friction values C_f. For higher Reynolds numbers (i.e. turbulent flow), the contribution to the measured shear stress is mostly dominated by the mean fluid motions for the inner rotating conditions $R_\Omega = -0.083$, while the velocity fluctuations in the azimuthal (u'_θ) and the radial (u'_r) directions contribute significantly for the counter and the outer rotating conditions, $R_\Omega = 0$ and $R_\Omega = 0.091$ respectively [4]. The velocity fluctuations u'_θ and u'_r were smaller for the outer rotation in contrast to the counter rotation, which clarifies the corresponding differences in friction values C_f.

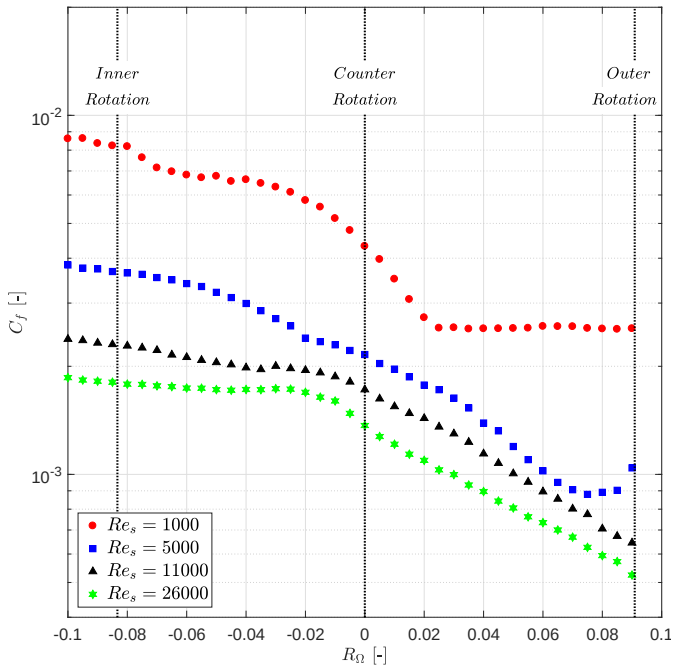

Figure A.3: Friction coefficient C_f as a function of rotation number R_Ω at constant shear Reynolds numbers $Re_s = 1000$ (red •), $Re_s = 5000$ (blue ■), $Re_s = 11000$ (black ▲) and $Re_s = 26000$ (green ★).

In conclusion, the rotation condition strongly influences the formation of flow structures and the corresponding shear stresses. With respect to the present investigation of drag reducing methods, the applied TC-flow would represent a common wall-bounded turbulent flow. The preferred operating condition would be exact-counter rotating cylinders ($Re_i = -Re_o$), to mimic a similar flow as a regular plane Couette flow with comparable shear stress values. In addition to that, the Taylor-Couette facility encounters artificial fluid motions when rotating only the inner or the outer cylinder. More specifically, the exact-counter rotation delivers random-oriented flow structures, where the inner rotation induces the familiar Taylor-vortices in the azimuthal direction due to dominant centrifugal forces, while the outer rotation results in Taylor-columns in the axial direction due to disruptive end-effects.

A.2. VALIDATION OF THE VON KÁRMÁN CONTRIBUTION

The fluid motions in the *von Kármán* gaps (top & bottom gaps in the axial direction) and the *Taylor-Couette* gap (gap in the radial direction), as shown in Figure 3.2, generate shear forces acting on the inner cylinder. The flow between the end-plates resembles a classical von Kármán swirling flow between two rotating co-axial disks [10, 11]. According to the study of Daily and Nece [12], the disk friction coefficient $C_{f,disk}$ is related to the disk Reynolds number $Re_d = |\Delta\omega| r_i^2/\nu$ and the axial spacing/disk radius ratio h/r_i, where $|\Delta\omega|$ is the relative angular velocity between inner and outer cylinders, r_i is the radius of the inner cylinder, ν is the fluid viscosity and h is the distance between the two end-plates. For the TC-facility, the torque contribution of the von Kármán gap (vK-gap) is considered to be independent of the operating conditions ($\sim R_\Omega$), as the relative angular velocity remains constant under all rotating conditions (see example in Table A.2). For the current setup, Tokgöz [4] assumed that the torque contribution of the von Kármán gaps equals half of the measured torque at $R_\Omega = 0.091$.

In order to validate this assumption, additional torque measurements were undertaken with substantially taller inner and outer cylinders, maintaining a similar gap distance h between the end-plates (i.e. vK-gap). The length of the cylinders applied in this validation study are listed in Table A.1. The validation measurements were performed under exact-counter rotating conditions (i.e. $R_\Omega = 0$) and covered all flow regimes (i.e. laminar, transitional and turbulent).

Table A.1: Specifications of the small and the tall Taylor-Couette systems.

	short cylinders	tall cylinders
L_o [mm]	222.1	881.5
L_i [mm]	216.7	876.2
h [mm]	2.70	2.65
Γ [-]	21.7	87.6

It is known that the flow in the horizontal vK-gaps induces a secondary flow in the TC-gap. Nevertheless, the effect of this secondary flow on the measured torque is expected to be minimal for the short and tall configurations, as both aspect ratios $\Gamma = L_i/(r_o - r_i)$ are considered to be significantly large [13, 14]. This permits to use the obtained torque data for the linear relation between the total measured torque M_{tot} and the inner cylinder length L_i in order to determine the contribution of the von Kármán flow, which is rewritten as:

$$C_{f,tot} L_i = \frac{M_{tot}}{\pi \rho r_i^2 U_{sh}^2} \tag{A.3}$$

A

Figure A.4 indicates the linear relation between the rewritten torque $C_{f,tot}L_i$ and the cylinder length L_i for a random laminar and turbulent flow. The black arrow highlights the intersection of the dashed line with the y-axis and represents the torque contribution of the von Kármán flow. For laminar flow $Re_s = 270$ (Figure A.4a), the vK-contribution is equivalent to the theoretical value (~50%), as described in Chapter 2. For turbulent flow $Re_s = 46 \times 10^3$ (Figure A.4b), the fluid motions in the TC-gap contribute significantly more to the total measured torque M_{tot} compared to the laminar flow conditions; the estimated vK-contribution reduces to around M_{vK}/M_{tot} ~0.25.

This evaluation procedure was followed for the remaining Reynolds numbers Re_s and delivered the relevant TC-contribution in contrast to the total measured torque as a function of Re_s, where $M_{TC}/M_{tot} = 1 - M_{vK}/M_{tot}$. Figure A.5 displays the estimated torque contribution of the TC-gap via the applied assumption and via the validation measurements. For the laminar flow conditions both methods determined a TC-contribution to the total torque of around ~50%, as expected. Remarkable agreement was observed for the transitional regime $Re_s = 400-4000$ and indicated a comparable trend in the transition from a laminar to a fully turbulent flow regime. For fully turbulent flow conditions, the flow contribution of the Taylor-Couette gap was underestimated by ±3% via the assumption method.

It can be concluded that a proper similarity was found between the two methods and confirmed that the suggested assumption, where the torque contribution of the von Kármán gaps equals half of the measured torque at $R_\Omega = 0.091$, was a suitable approach to separate the torque contribution of the TC-gap and vK-gaps.

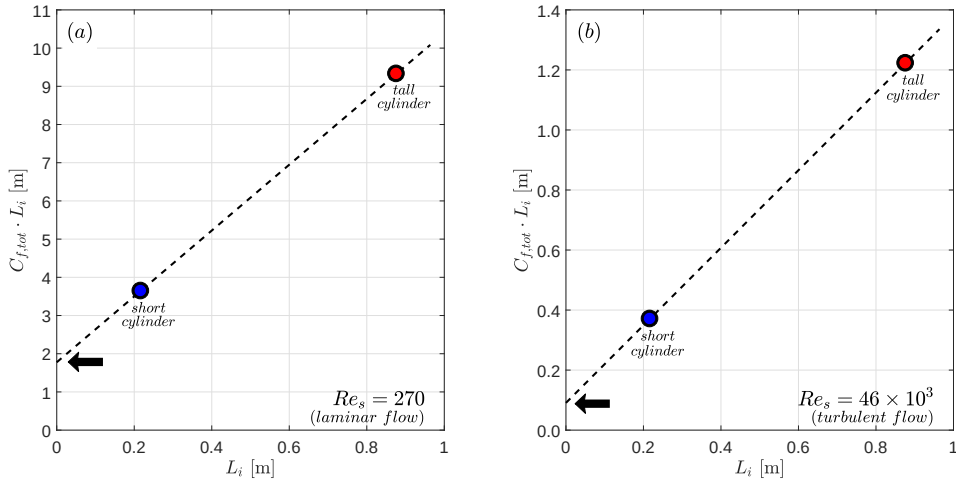

Figure A.4: The obtained $C_{f,tot}L_i$-values of the short and tall cylinder configuration for a) laminar flow conditions $Re_s = 270$ and b) turbulent flow conditions $Re_s = 46 \times 10^3$. The dashed line indicates the assumed linear relation between $C_{f,tot}L_i$ and L_i. The black arrow suggests the torque contribution due to the presence of the von Kármán gap.

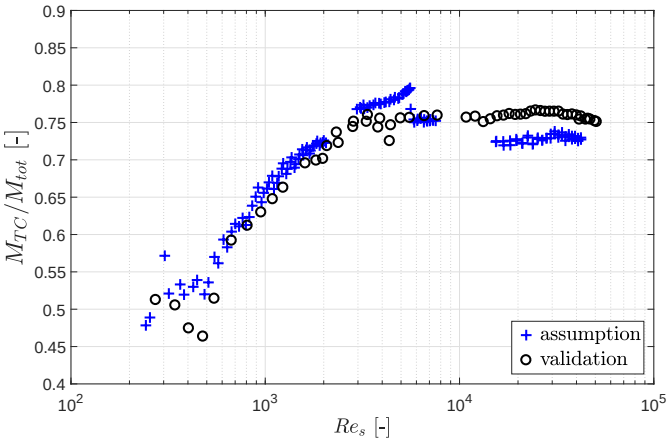

Figure A.5: Estimated torque contribution of the TC-gap M_{TC}/M_{tot} as a function of the shear Reynolds number Re_s under exact-counter rotating conditions (i.e. $R_\Omega = 0$).

Table A.2: Example of the shear flow operating conditions R_Ω at $Re_s = 29000$ with a constant relative angular velocity $|\Delta\omega|$ between the two end-plates of the inner and the outer cylinder.

R_Ω [-]	Re_i [-]	Re_o [-]	ω_i [rad/s]	ω_o [rad/s]	$\lvert\Delta\omega\rvert$ [rad/s]
-0.083	-27.8×10^3	0	-25.3	0	25.3
-0.050	-22.5×10^3	5.8×10^3	-20.5	5.8	25.3
0	-14.5×10^3	14.5×10^3	-13.2	12.1	25.3
0.050	-6.6×10^3	23.2×10^3	-6.0	19.3	25.3
0.091	0	30.3×10^3	0	25.3	25.3

A

A.3. ROTATION EFFECT

APPARENT ROTATION NUMBER

In the current study, the inner cylinder surface was modified in order to quantify the accompanying drag change. The torque measurements were performed under exact-counter rotating conditions ($R_\Omega = 0$). Under these operating conditions and when the friction at the inner cylinder wall changes due to the surface modification, the core flow co-rotates slightly with either the inner or the outer cylinder due to a change in the total drag force at the inner cylinder wall. Based on the angular momentum balance, the small shift in the average bulk velocity $\bar{U}_b$ is given by:

$$\delta = \frac{\bar{U}_b}{U_{out}} = \frac{1 - \sqrt{C_f / C_{f,0}}}{1 + \sqrt{C_f / C_{f,0}}} \tag{A.4}$$

where δ is the velocity shift in the azimuthal direction at the radial location where $U(r) = 0$, U_{out} is the outer cylinder velocity and C_f is the measured friction coefficient of the modified surface. For an unaltered and smooth inner cylinder, the friction coefficient equals $C_f = C_{f,0}$ and maintains the general average bulk velocity $\bar{U}_b = 0$ and thus $\delta = 0$. When the friction at the inner cylinder wall increases, i.e. $C_f > C_{f,0}$, the average bulk velocity becomes $\bar{U}_b < 0$ (i.e. $\delta < 0$), which implies that the bulk fluid co-rotates slightly with the inner cylinder. The same holds for the reversed scenario, when $C_f < C_{f,0}$.

The small shift in the average bulk velocity under exact-counter rotating conditions ($R_\Omega = 0$) can be quantified as an apparent rotation number $\hat{R}_\Omega$, which is estimated by:

$$\hat{R}_\Omega = (1 - \eta) \frac{(U_i + \bar{U}_b) + (U_o + \bar{U}_b)}{\eta(U_o + \bar{U}_b) - (U_i + \bar{U}_b)} \tag{A.5}$$

and can be rewritten as:

$$\hat{R}_\Omega = \frac{2\delta(1 - \eta)}{1 + \eta - \delta(1 - \eta)} \tag{A.6}$$

where $\eta = r_i / r_o$ is the gap ratio, with r_i and r_o as the radius of the inner and the outer cylinder respectively. It was demonstrated that the friction coefficient C_f is strongly dependent on the rotating conditions, i.e. the rotation number R_Ω. Consequently, the apparent rotation number $\hat{R}_\Omega$ represents a stand-alone drag change in contrast to the actual operating condition $R_\Omega = 0$ (see Figure A.3), in other words $C_f(\hat{R}_\Omega) \neq C_f(R_\Omega = 0)$. This rotational drag change is part of the total measured drag change due to the surface modification and therefore is called the rotation effect.

MODEL ASSESSMENT

The method to correct for the rotation effect in order to obtain the actual net drag change by the surface modification, originates from the angular momentum balance where the possible shift in average bulk velocity $\bar{U}_b$ has been incorporated:

$$\begin{aligned} \tau_w &= \frac{1}{2}\rho\, C_{fi}\, (U_{in} - \bar{U}_b)^2 \\ &= \frac{1}{2}\rho\, C_{fo}\, (U_{out} - \bar{U}_b)^2 \left(\frac{r_o}{r_i}\right)^2 \end{aligned} \tag{A.7}$$

The rotational drag change is then related to the apparent rotation number $\hat{R}_\Omega$, which on its turn is determined by the present bulk velocity shift δ. In order to validate Equation A.6, additional PIV measurements provided the velocity profiles between the cylinders at various rotation numbers R_Ω around $R_\Omega = 0$, while maintaining an identical Reynolds number Re_s.

Figure A.6 shows three azimuthal velocity profiles of rotation number $R_\Omega = 0.005, 0$ and -0.005 at Reynolds number $Re_s = 29 \times 10^3$. Despite the small change in the cylinder velocities, a significant mutation is observed in the shape of the velocity profiles. For exact-counter rotation $R_\Omega = 0$, the radial location with zero azimuthal velocity (i.e. $U_\theta / U_o = 0$) is around $(r - r_i)/d = 0.56$. The inset of Figure A.6 images the positive and the negative shift of the velocity profiles (i.e. δ^+ and δ^-) at this location when the rotation number R_Ω was changed. The shifts in the azimuthal velocity δ are listed in Table A.4, as well as the estimated apparent rotation numbers $\hat{R}_\Omega$ based on the measured velocity shift δ (Eq. A.6). The apparent rotation number $\hat{R}_\Omega$ deviates roughly 5% from the imposed rotation number R_Ω and justifies a proper estimation of the additional drag change due to the rotation effects.

Table A.3: The azimuthal velocity shift δ and the estimated apparent rotation numbers $\hat{R}_\Omega$ at $Re_s = 29000$.

R_Ω	δ	$\hat{R}_\Omega$
0.005	6.0%	0.0052
0	0%	0
-0.005	-5.4%	-0.0047

A

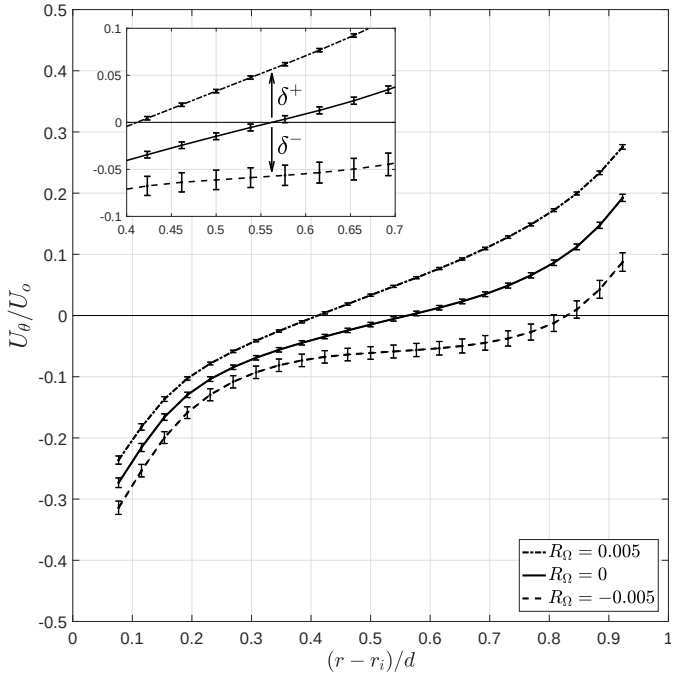

Figure A.6: Azimuthal velocity profiles at a rotation number $R_\Omega = 0.005, 0$ and -0.005 at a Reynolds number $Re_s = 29 \times 10^3$. The velocities are normalized to the outer cylinder velocity for exact-counter rotation $R_\Omega = 0$.

A.4. FRICTIONAL HEATING & FLUID TEMPERATURE

Frictional heating is an associated phenomena for viscous shear flows. Without forced cooling the fluid temperature rises during an on-going measurement. Consequently, the viscosity of the fluid drops and results in an increase in the shear Reynolds number Re_s. In order to estimate a reliable operational Reynolds number Re_s, it is necessary to determine the corresponding time-dependent fluid temperature T_f. For the current facility, it was not feasible to implement a common temperature sensor without inducing additional flow disturbances. Therefore, the fluid temperature T_f was estimated via a simplified heat balance equations, with the frictional heating power P_{heat} and the outer wall temperature T_{out} of the outer cylinder as the input parameters.

The amount of frictional heating power P_{heat} is compiled by the total measured torque M_{tot} multiplied by the relative angular velocity between the inner and the outer cylinder (resp. ω_i and ω_o):

$$P_{heat} = |\omega_o - \omega_i| \, M_{tot} \tag{A.8}$$

The outside wall temperature T_{wall} was monitored during a measurement by an infrared thermometer to evaluate the actual fluid temperature T_f via heat transfer calculations. A simplification of the overall heat balance is given in Equation A.9, where m_i and $c_{p,i}$ represent the mass and the heat capacity of the applied facility materials (PMMA, PVC and brass). The assumption is made that cooling only occurs at the outer wall of the outer cylinder, which rotates with a specific angular velocity ω_o that induces forced convection. Other essential parameters are the thermal conductivity of the plexiglas k_{px} [W/(m^{2}K)], the wall thickness of the outer cylinder δ_c [m], and the equivalent surface area of the outer cylinder that transfers the heat $A_c \approx 2\pi(r_o+\delta_c/2)L_o$ [m^2]. Compiling the relevant parameters leads to:

$$\sum \left(m_i c_{p,i}\right) \frac{\partial T_f}{\partial t} = P_{heat} - \frac{k_{px}}{\delta_c} A_c \left(T_f - T_{wall}\right) \tag{A.9}$$

Table A.4: The mass and specific heat capacity of the TC-facility components.

Component i	Material	m_i [kg]	$c_{p,i}$ [J/(kg^{o}C)]
Fluid	water	1.8	4180
Inner cylinder	pmma	1.0	1270
Inner cylinder, end-plates	pvc	2.3	900
Outer cylinder	pmma	1.1	1270
Outer cylinder, bottom-plate	pmma	0.7	1270
Outer cylinder, top-plate	brass	2.3	380

A

The outside wall temperature T_{wall} was recorded every second (i.e. $\delta t = 1$) during the measurement. As very small temperature changes are observed between two time-steps, the approximation is made $T_f(t+\Delta t) \approx T_f(t)$ and simplifies Equation A.9:

$$T_f(t+\Delta t) = T_f(t) + \frac{P_{heat} - \frac{k_{px}}{\delta_c} A_c \left(T_f - T_{wall}\right)}{\sum(m_i c_{p,i})} \Delta t \tag{A.10}$$

The fluid temperature T_f was measured with a thermocouple at the start and at the end of every measurement cycle, when the cylinders were at rest. The start fluid temperature $T_f(t = t_0)$ is the initial temperature in the heat balance equation (Eq.A.9), while the end fluid temperature $T_f(t = t_{end})$ verifies an accurate progression of the fluid temperature T_f during the measurement cycle. Generally, the measured fluid end-temperature deviated less than $\pm 0.2^o$C compared to the calculated fluid end-temperature $T_f(t = t_{end})$, see Figure A.7. An iteration method is suggested to optimize the estimated time-dependent fluid temperature $T_f(t)$ during the measurement cycle, where the actual fluid temperature $T_f(t = t_0)$ and $T_f(t = t_{end})$ are used to calibrate the estimation.

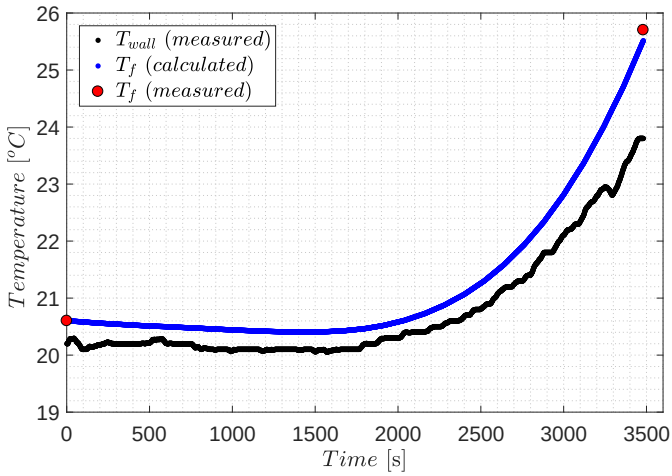

Figure A.7: Example of the estimated temperature development during a measurement cycle.

REFERENCES

[1] A. J. Greidanus, R. Delfos, S. Tokgoz, and J. Westerweel, *Turbulent Taylor-Couette flow over riblets: drag reduction and the effect of bulk fluid rotation,* Experiments in Fluids **56**, 1 (2015).

[2] R. Delfos, F. Ravelet, and J. Westerweel, *Scaling of torque in turbulent taylor-couette flow with background rotation,* in *Advances in Turbulence XII* (Springer, 2009) pp. 629–632.

[3] F. Ravelet, R. Delfos, and J. Westerweel, *Influence of global rotation and Reynolds number on the large-scale features of a turbulent Taylor-Couette flow,* Physics of Fluids (1994-present) **22**, 055103 (2010).

[4] S. Tokgöz, *Coherent Structures in Taylor-Couette Flow: Experimental Investigation*, Ph.D. thesis, TU Delft, Delft University of Technology (2014).

[5] D. P. Lathrop, J. Fineberg, and H. L. Swinney, *Transition to shear-driven turbulence in Couette-Taylor flow,* Physical Review A **46**, 6390 (1992).

[6] G. S. Lewis and H. L. Swinney, *Velocity structure functions, scaling, and transitions in high-Reynolds-number Couette-Taylor flow,* Physical Review E **59**, 5457 (1999).

[7] B. Eckhardt, S. Grossmann, and D. Lohse, *Torque scaling in turbulent Taylor-Couette flow between independently rotating cylinders,* Journal of Fluid Mechanics **581**, 221 (2007).

[8] E. Aydin and H. Leutheusser, *Plane-couette flow between smooth and rough walls,* Experiments in fluids **11**, 302 (1991).

[9] F. M. White, *Fluid mechanics* (WCB, 1999).

[10] G. K. Batchelor, *Note on a class of solutions of the navier-stokes equations representing steady rotationally-symmetric flow,* The quarterly journal of mechanics and applied mathematics **4**, 29 (1951).

[11] K. Stewartson, *On the flow between two rotating coaxial disks,* in *Mathematical Proceedings of the Cambridge Philosophical Society*, Vol. 49 (Cambridge University Press, 1953) pp. 333–341.

[12] J. W. Daily and R. E. Nece, *Chamber dimension effects on induced flow and frictional resistance of enclosed rotating disks,* Journal of Fluids Engineering **82**, 217 (1960).

[13] J. Cole, *Taylor-vortex instability and annulus-length effects,* Journal of Fluid Mechanics **75**, 1 (1976).

[14] M. Burin, E. Schartman, and H. Ji, *Local measurements of turbulent angular momentum transport in circular couette flow,* Experiments in fluids **48**, 763 (2010).

ACKNOWLEDGEMENTS

A PhD research is a journey of discoveries and amazements, with hightlights and dissapointments, which involved many people. I would like to thank them all.
First of all, I would like to express my appreciation and gratitude for the involvement of my supervisors Jerry Westerweel, René Delfos and Stephen Picken. Jerry, I admire your open view on generating ideas and solutions. It all sounded so simple, but often it was a struggle to set up the measurements differently as well as the endless data processing. Nevertheless, the work has been improved significantly. The freedom and encouragement that I received gave me the confidence to go my own way and to become an independent researcher. You were always open for my ideas and plans that I wanted to initiate, regarding the topics on the interface of fluid dynamics and sports, mainly about swimming and rowing.
René, the "daily supervisor". Our conversations and meetings were mostly about the practical implementation of the experiments and data analysis. The questions were short, your answers long but effective. In my memory, you were always prepared to review and to improve several conference papers just before the final deadline, even during the weekends or during your holidays. I consider the last conference in Glasgow as a team effort, where the real work was done during the day and the social work in the evening.
Stephen, you were the very first who was involved in an intended study of drag reducing coatings for rowing boats. It soon became clear that the subject was outside my own discipline and Jerry was involved during the writing of the research proposal. The crossovers between chemistry and fluid dynamics was an eye-opener for me, and I continuously observe opportunities for novel research projects. We will certainly meet again!
Dear Caroline. All the work you have done to make my period within the lab run smoothly has been crucial. The conditions were well organized, such that I could focus on my own research. Super bedankt!
I would also like to thank Jan, Jasper and Edwin. All of you have contributed to the practical implementation of the scientific work. Among them, setting up a complex Labview program for the periodic-driven Taylor-Couette flow (Jan); the design, construction and repair of test facilities (Jasper); and the help with setting up all optical measurement systems (Edwin) have been some essential issues that I would never have accomplished without you.
Several student projects (BEP, internships and graduation) have contributed whithin the framework of this PhD research. Among others, the publication of the work on "Turbulent spot in linearly stable Taylor-Couette flow" (Arjang Alidai), the investigation of the von Kármán flow contribution to the total torque as a function of the shear Reynolds number (Emma Aubert) and the additional measurements regarding the perio-

dically-driven Taylor-Couette flow (Manon Baudot). Major thanks.
This PhD project took a bit longer than usual, due to the unusual combination of doing scientific research and topsport. There were too many PhDs, postdocs and guest researchers to thank all by name. Thank you all for the great time in the lab!
For sure, I would like to highlight a few people, in particular my roommates and research collaborators. My first roommates, Astrid and Marcel. As a chemist, you ensured that I immediately felt welcome in a new scientific discipline. You patiently taught me the basics of the lab, fluid dynamics and PIV.
Yoshi, you came over from Japan for one year to become an expert on tomo-PIV. I enjoyed our conversations about our cultures. Our small "reunion" on Tokushima Island was very nice and special, especially the taxi ride with karaoke-disco showed that you are a natural.
Florian, thanks to your work I came into contact with the optical measurement method to reconstruct the wall deformations of the compliant coating under a turbulent shear flow. This method realized a large part of this thesis. You also appear to be an expert on the social level, which was verified in several conferences and workshops. Merci, monsieur!
My last roommates were Pedro and Ernst Jan (aka EJ). You always made the atmosphere in the room! Pedro, your analytical model of the Taylor-Couette velocity profile of non-Newtonian fluids is still one of the things that keep circulating my mind. That publication will be there for sure.
EJ, the interest in rowing brought us together and we have initiated and executed many projects. I have watched with great admiration how you realized the Rowbot, to visualize and quantify the fluid motions around a dynamic rowing blade. Your research gave new insights in order to row faster. The many conversations we had about unleashing “our” field of expertise on sports, still motivates me to think outside the box and search for the cross-overs between different fields and disciplines.
Arati, the goal of our exploratory measurements was to quantify the velocity profiles of ketchup in the Taylor-Couette facility by using the ultrasound measurement method. It never resulted in a publication, but I keep the option open to take additional measurements! I am grateful to you for reading my thesis and providing useful feedback.

I’m very thankful to my friends and family that have supported me over the past few years. In particular my parents. Pap en mam, jullie vertrouwen en steun heeft me altijd het gevoel geven dat ik mezelf kon ontwikkelen tot wie ik nu ben. Mam, het doet me veel verdriet dat pappa de feitelijke afronding van dit onderzoek niet meer heeft kunnen meemaken. Ik mis hem, maar in gedachten is hij altijd bij ons en ik weet dat hij vervuld zou zijn met trots.

Lieve Marianne, je bent mijn maatje. De laatste loodjes van dit proefschrift wogen het zwaarst. Het is eindelijk af! Samen met Yves en Lina gaan we nieuwe avonturen tegemoet! Ik hou van jullie.

Arnoud Greidanus
Amsterdam, August 2020

ABOUT THE AUTHOR

Arnoud Jan GREIDANUS

Arnoud Greidanus was born on June 1st 1981 in Leiderdorp (The Netherlands). After graduated from high school in Weert in 1999, he moved to Delft to study Chemical Engineering at the Delft University of Technology (TU Delft). He started rowing at the student club DSR Proteus-Eretes in 2000, which eventually evolved to a professional rowing career at the Dutch National Rowing Team from 2005 till 2013. Sport highlights were the Gold medal at the World Rowing Championships (2007), joining the Olympic Games (Beijing, 2008), the Silver medal at the World Rowing Championships (2012), and many more. In 2009, Arnoud took a sabatical year in order to re-charge his rowing battery, which also gave the opportunity to finish his Master degree in (Bio)Chemical Engineering. That year, he also initiated the project proposal for his PhD research, which he immediately started in 2010. He combined his PhD research (part-time) with his rowing career untill 2013. After the post-Olympic year (2013), he retired from rowing and dedicated his time to fullfill the PhD research. As a spin-out from this research, he founded the company "flowmatters" in 2016, which has been active on frictional measurements, material development and turbulent flow research in general. In June 2018 he re-joined the TU Delft as a postdoctoral research associate, in a joint-industrial research project to optimize the gas well deliquification process by delaying liquid loading. He continues the work activities at "flowmatters" and is currently living in Amsterdam with Marianne, and their son Yves Storm (2017) and their daughter Lina Mare (2019).

PROFESSIONAL ACTIVITIES

Jun 2020 - present:	Projectleader & Scientific Researcher at TU Delft.
Oct 2016 - present :	Consultant/Founder at research company "flowmatters".
Jun 2018 - Oct 2019 :	Postdoctoral Research Associate at TU Delft.
Feb 2010 - Nov 2016 :	PhD Researcher at TU Delft. part-time in 2010-2013, full-time in 2014-2016.
Apr 2005 - Nov 2013 :	Elite Rowing Athlete at Dutch National Rowing Team (KNRB).

SCIENTIFIC CONTRIBUTIONS

PAPERS

1. **A.J. Greidanus**, R. Delfos, S.J. Picken & J. Westerweel. *Experimental investigation of the interaction between compliant surfaces and a turbulent shear flow.* Manuscript in Preparation.
2. **A.J. Greidanus**, R. Delfos, & J. Westerweel. *Scaling and riblet drag performance under periodic turbulent conditions.* Manuscript in Preparation.
3. H.O.G. Benschop, **A.J. Greidanus**, R. Delfos, J. Westerweel & W.-P. Breugem. *Deformation of a linear viscoelastic compliant coating in a turbulent flow.* Journal of Fluid Mechanics **859**, 613-658 (2019).
4. A. Alidai, **A.J. Greidanus**, R. Delfos & J. Westerweel. *Turbulent Spot in Linearly Stable Taylor Couette Flow.* Flow, Turbulence and Combustion **96** (3), 609-619 (2016)
5. **A.J. Greidanus**, R Delfos, S Tokgoz & J Westerweel. *Turbulent Taylor–Couette flow over riblets: drag reduction and the effect of bulk fluid rotation.* Experiments in Fluids **56** (5), 107 (2015).

SELECTION OF CONTRIBUTED TALKS

1. A. Dash, A. Anantharaman, A.J. Greidanus & C. Poelma. *Simultaneous Ultrasound Imaging Velocimetry (UIV) and Flow Visualization in Taylor-Couette flows: Validation of UIV in single-phase flows.* 13th International Symposium on Particle Image Velocimetry (ISPIV2019), 22-24 July 2019, Munich, Germany.
2. P. Shoeibi Omrani, A.J. Greidanus, F. Vercauteren, J. van 't Westende, R. Henkes, U. Gawandalkar. *Effect of salinity and thermal ageing on the performance of foamers for gas well deliquification.* SPE Workshop: Production Optimisation in Gas and Oil Assets, 7-8 November 2018, The Hague, The Netherlands.
3. H.O.G. Benschop, A.J. Greidanus, R. Delfos & J. Westerweel & W.-P. Breugem. *Deformation of a viscoelastic wall layer in turbulent flows.* 12th European Fluid Mechanics Conference (EFMC12), 9-13 September 2018, Vienna, Austria.
4. F. Charruault, A.J. Greidanus, W.-P. Breugem & J. Westerweel. *A dot tracking algorithm to measure free surface deformations.* 18th International Symposium on Flow Visualization (ISFV 18), 26-29 June 2018, Zurich, Switzerland.
5. R. Delfos, A.J. Greidanus, F. Charruault & J. Westerweel. *Wave characteristics of a compliant coating under a turbulent flow.* 5th International Conference on Advanced Model

Measurement Technology for the Maritime Industry (AMT'17), 11-13 October 2017, Glasgow, UK.

6. A.J. Greidanus, R. Delfos & J. Westerweel. *Fluid-structure interaction of compliant coatings under turbulent flow conditions: force and PIV analysis.* 5th International Conference on Advanced Model Measurement Technology for the Maritime Industry (AMT'17), 11-13 October 2017, Glasgow, UK.

7. C.B. Kuyt, A.J. Greidanus & J. Westerweel, *Drag reduction by applying speedstrips on rowing oars*, 11th conference of the International Sports Engineering Association (ISEA 2016), 11-14 July 2016, Delft, The Netherlands.

8. A.J. Greidanus, R. Delfos & J. Westerweel, *Drag and power-loss in rowing due to velocity fluctuations.* 11th conference of the International Sports Engineering Association (ISEA 2016), 11-14 July 2016, Delft, The Netherlands.

9. A. Greidanus, R. Delfos, S. Tokgöz & J Westerweel. *Experimental study of surface modification in a fully turbulent Taylor-Couette flow.* 15th European Turbulence Conference 2015 (ETC15), 25-28 August 2015, Delft, The Netherlands.

10. A. Greidanus, R. Delfos, S. Tokgoz & J. Westerweel. *Riblet drag reduction and the effect of bulk fluid rotation in a fully turbulent Taylor-Couette flow.* European Drag Reduction and Flow Control Meeting (EDRFCM 2015), 23–26 March 2015, Cambridge, UK.

11. A.J. Greidanus, R. Delfos & J. Westerweel. *Drag reduction by surface treatment in turbulent Taylor-Couette flow.* 13th European Turbulence Conference 2011 (ETC13), 12-15 September 2011, Warsaw, Poland.